Summer 2017

A Partitioned Approach for Computing Fluid-Structure Interaction, With Application to Tumor Modeling and Simulation

Asim Timalsina
Old Dominion University

A PARTITIONED APPROACH FOR COMPUTING FLUID-STRUCTURE INTERACTION, WITH APPLICATION TO TUMOR MODELING AND SIMULATION

by

Asim Timalsina
B.S. May 2011, George Mason University
M.S. August 2013, Old Dominion University

A Dissertation Submitted to the Faculty of
Old Dominion University in Partial Fulfillment of the
Requirements for the Degree of

DOCTOR OF PHILOSOPHY

COMPUTATIONAL AND APPLIED MATHEMATICS

OLD DOMINION UNIVERSITY
August 2017

Approved by:

Fang Hu (Co-Director)

Jin Wang (Co-Director)

Gene Hou (Member)

Yan Peng (Member)

ABSTRACT

A PARTITIONED APPROACH FOR COMPUTING FLUID-STRUCTURE INTERACTION, WITH APPLICATION TO TUMOR MODELING AND SIMULATION

Asim Timalsina
Old Dominion University, 2017
Director: Dr. Fang Hu

Modeling and Simulation plays a critical role in understanding complex physical and biological phenomena as it provides an efficient and controlled test environment, without the risk of costly experiments and clinical trials. In this dissertation, we present an extensive study of two such systems with integrated application: Fluid structure interaction (FSI) and virotherapy on tumor. Moreover, we substantiate a few preliminary results of FSI application on tumor.

The FSI problem comprises of fluid forces exerted on the solid body and the motion of the structure affecting the fluid flow. FSI problems are of great interest to applied industries, however they are also computationally challenging due to the complex structures involved and freely moving boundaries. We propose a partitioned approach to compute FSI that integrates the direct forcing technique with the Immersed Boundary Method which is able to handle complex rigid, moving, solid and elastic structures. We then propose and analyze a virotherapy model for tumor treatment that includes both the innate and adaptive immune cells which are then studied in a variety of settings. We demonstrate that immune responses, burst sizes, and repeated administration of viral doses on regular intervals play a huge role in the success of the virotherapy. A detailed stability analysis of the ODE tumor virotherapy model is also performed. We analyzed some of the biologically meaningful equilibrium analytically and computationally, whenever analytic solution was impossible. We confirm that tumor can be controlled by showing the existence of endemic equilibria that are locally (or globally if certain criteria are met) stable for a set of parameters. Finally, the FSI method is applied to multiple non-stationary discs to gain some insights in the behavior of the cellular aggregation. This will serve as a stepping stone to our future work of understanding the intra-cellular interaction among tumor cells.

ACKNOWLEDGMENTS

First of all, I would like to thank my advisor Dr. Jin Wang for taking me in as his student and guiding me through all of my research work. He was available promptly and gave great suggestions whenever I reached a dead-end in my projects. This dissertation would not have been possible without his support. I am also very thankful to Dr. Fang Hu for becoming my co-advisor in such a short notice. It has been a very rewarding experience working with Dr. Gene Hou in the fluid-structure interaction projects. Many thanks to him and Dr. Yan Peng for serving on my dissertation committee. I would also like to thank our Graduate Program Director Dr. Raymond Cheng for his always helpful advises and support over the course of the years. All of their time, advise, and guidance have been very valuable.

I am thankful to the Department of Mathematics and Statistics for providing me with resources to succeed in my academic pursuit of excellence. I would like to thank our department and the Modeling and Simulation Program from MSVE department for their financial support.

I am very thankful to my father and mother for their continuous support to achieve this goal. My special thanks goes to my loving wife Anima for her constant support and encouragement during this time. Finally, I am very appreciative of all my family (especially my father and mother-in-law), relatives and friends for their endless support, and this section wouldn't be complete without thanking them.

TABLE OF CONTENTS

Page

LIST OF TABLES

LIST OF FIGURES

CHAPTER 1

INTRODUCTION

Fluid structure interaction (FSI) and tumor virortherapy are very popular and important topics in their own domain. There are numerous advantages of using advanced mathematical concepts and computers to model and simulate real life industry applications. Computer simulations are becoming an indispensable tool for the design and analysis of complex systems; performance can be tested in advance in an inexpensive manner and interactions among various independent parameters can be reproduced and studied in a very controlled environment [73]. A primary focus of this dissertation is to design and study mathematical and computational models for two processes: i) fluid structure interaction (FSI) that is able to handle any structure/s and ii) virotherapy of tumor. Figure 1 shows the overall structure of this dissertation. The highlight of this dissertation is definitely the proposal of the computational framework for FSI and the tumor virotherapy model with mediated immunity, however the stability analysis of virotherapy is studied in great detail as well.

This dissertation is organized into two core chapters detailing the FSI process and the tumor virotherapy model; in addition to the usual Introduction and Conclusion. The fourth chapter will serve as a building block for our future work in cancer cell-cell interaction and interaction with exterior fluids. Each chapter will contain a complete background section that will dive deep into the subject, along with a relevant discussion section. This dissertation will begin with this detailed description to all the topics that will be introduced in the subsequent chapters.

Computational Fluid Dynamics (CFD) is a branch of fluid mechanics that simulates and visualizes fluid flow along with flows passing through various objects. The process involves mathematical modeling of the flow usually through Navier Stokes equation, numerical modeling involves designing solvers, discretization of spatial and temporal terms, and search of efficient and fast solver that is able to handle complex flows. FSI naturally involves CFD, but often times it also includes a structure that is fully or partially immersed in the fluid. Although FSI is a multiphysics simulation, a lot of emphasis is given in the CFD design. In Chapter 2, we propose a new partitioned approach to compute FSI by extending the

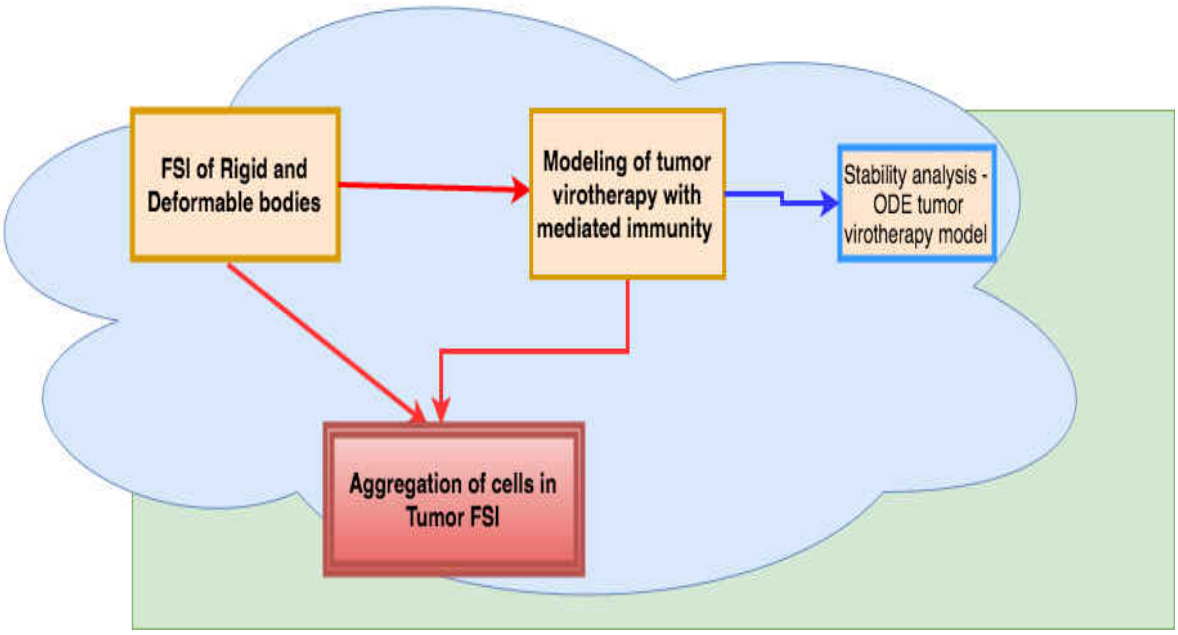

FIG. 1: Overview of the dissertation

original direct-forcing technique and integrating it with the immersed boundary method. The immersed body moves with the local fluid velocity and the deformations trigger forces which in turn affects the motion of the fluid [9]. The fluid and structural equations are calculated separately via their respective disciplinary algorithms, with the fluid motion solved by the immersed boundary method on a uniform Cartesian mesh and the structural motion solved by a finite element method, and their solution data only communicate at the fluid-structure interface. This computational framework is capable of handling FSI problems with sophisticated structures described by detailed constitutive laws. The proposed methods are thoroughly tested through numerical simulations involving viscous fluid flow interacting with rigid, elastic solid, and elastic thin-walled structures.

Cancer is a serious illness that causes millions of deaths every year all around the world. Common forms of treatment of cancer involve radiation therapy, chemotherapy, surgery, etc. A novel method was derived by direct injection of virus into tumor in the middle of the 20^{th} century [71]. The first virus implemented in this regards were found to perform very poorly mainly because of two hindrances: i) it destroyed healthy cells and ii) the immune

responses destroyed the viruses upon injection which prevented them from destroying tumor cells. In the later years, many improvements were made so that the virus chosen was cautiously able to destroy the tumor cells by distinguishing the virus in the first injection, along with other methods that enabled to keep the healthy cells unharmed. This method, called oncolytic virotherapy, is a technique that employs replication competent viral vectors as agents that preferentially attack and proliferate in cancerous cells,leaving most healthy cells uninjured [69]. It is a very promising treatment that has gained a lot of attention in the past decade. There are many oncolytic viruses which have demonstrated anti-tumor efficacy, including adenoviruses, Coxsackieviruses, herpes simplex viruses, measles viruses, Newcastle disease virus, reoviruses, Seneca Valley virus,vaccinia viruses, and vesicular stomatitis virus (VSV) [69]. In Chapter 3, we propose a new mathematical modeling framework based on partial differential equations to study tumor virotherapy with mediated immunity. The model incorporates both innate and adaptive immune responses, and represents the complex interaction among tumor cells, oncolytic viruses, and immune systems on a domain with a moving boundary. Using carefully designed computational methods, we conduct extensive numerical simulation to the model. The results allow us to examine tumor development under a wide range of settings, and provide insight into several important aspects of the virotherapy, including the dependence of the efficacy on a few key parameters and the delay in the adaptive immunity. Our findings also suggest possible ways to improve the virotherapy for tumor treatment. In addition to the PDE model, we also present and analyze non-linear tumor growth model based on ordinary differential equations that illustrates the interaction between oncolytic virus, tumor cells and immune cells. We investigate both the exterior (analytically) and the interior(using numerical simulations) equilibrium points of this reduced system. The numerical simulation of the system is conducted using the fourth order Runge Kutta method. We carry out the stability analysis on the boundary and positive equilibrium points of the model and show that there are possible locally and globally stable equilibrium points. We also found that the system exhibits a periodic limit cycles for some parameters. In addition, we have shown that the tumor can be eliminated completely with this virotherapy process under certain conditions which conforms to our previous study with PDEs. We provide numerical simulations and stability plots to demonstrate our result.

In Chapter 4, we try to set up future work by combining the previous two modeling efforts in FSI and tumor cells, and present some preliminary numerical results for the aggregation of cells. Clustering of cells and movement of the cluster as a single unit is an important aspect

in studying the tumor bio-mechanism. In this chapter, we model cell as a freely moving rigid disc and study the aggregation of cells. We do this by carefully simulating a single disc and multiple discs that tracks their motion in the fluid along with the adhesion process. In the final chapter, we draw conclusions and present some directions to expand our current work.

Note: Some part of the second and third chapters are published in *Communications in Computational Physics* and *Bulletin of Mathematical Biology* respectively. Majority of the work in all chapters are my own work with my advisor Dr. Jin Wang except for modeling structure dynamics which was collaborative work with Dr. Gene Hou and equations for PDE tumor model which was formulated in collaboration with Dr. Jianjun Paul Tian.

CHAPTER 2

FLUID STRUCTURE INTERACTION

2.1 BACKGROUND

The interactions between viscous fluid flows and immersed solid structures are nonlinear multi-physics phenomena with application to a wide range of scientific and engineering disciplines [4, 10]. The study of fluid-structure interaction (FSI) is an emerging field that has been fast growing in recent decades. Owing to the difficulties in analysis and limitations in experiments for these strongly nonlinear problems, FSI research and development largely rely on computational methods.

Current numerical methods for FSI may be broadly classified in two categories: the *monolithic* approach and the *partitioned* approach. The first approach [13, 23] uses a unified system to represent the entire FSI problem and employs a single algorithm to solve the fluid and structure dynamics simultaneously. The monolithic approach can potentially achieve very high accuracy in FSI simulation, but it typically demands large computational effort, and it may require substantial resources and expertise to develop and implement such an algorithm. In contrast, the partitioned approach [26, 30] treats the fluid and the structure as two systems which can be computed separately with their respective solvers. Thus, fluid and structural dynamics may be solved with different mesh discretizations and numerical algorithms, and the solution data communicate at the fluid-structure interface. A significant advantage of this approach is the capability to integrate available disciplinary algorithms with respect to the fluid and structural dynamics, thus reducing the effort and time in FSI code development. A challenge, however, is to effectively coordinate the disciplinary solvers to achieve an accurate and efficient FSI solution procedure.

Another way to categorize FSI methods is based on the types of meshes employed, and there are two major classes: the *conforming mesh* methods and the *non-conforming mesh* methods. The Lagrangian methods [4,6] and the Arbitrary Lagrangian-Eulerian methods [25] are typical examples of the conforming mesh approach, where a mesh-updating procedure is generally required at each time step corresponding to the movement/deformation of the

immersed structures. On the other hand, non-conforming mesh methods employ fixed (normally Cartesian) grids which eliminate the need of re-meshing and lead to reduced algorithmic complexity and improved computational efficiency, an advantage compared to the conforming mesh methods.

The best known non-conforming mesh method for FSI is probably the immersed boundary method invented by Peskin [20]. This numerical technique solves the fluid equations with an additional forcing term which represents the effects of the immersed structure acting on the fluid motion. Essentially, the fluid equations are solved in the entire domain with a fixed Eulerian mesh, and the immersed structure is represented as a moving boundary tracked on a separate manner. Due to its efficiency, flexibility and robustness, the immersed boundary method has become increasingly popular in FSI study and many progresses, in both the methodology and application, have been made in recent years (see, e.g., [11,15,17,24,31,32]). One major limitation associated with this approach, however, is that it primarily deals with structures that do not occupy volumes; e.g., a fiber in 2D space and a membrane in 3D space. Although immersed bodies with a finite volume can be approximated by a network of connected fibers, each of which can be treated as an immersed boundary, such an approximation may not accurately model the realistic structural response to the fluid motion. Some other variations of the method, such as the immersed finite element method [32], are able to handle bulk solid structures described by material constitutive laws, yet their applications to more sophisticated structural settings are still to be seen. Additionally, in the presence of rigid or nearly rigid structures, methods of the immersed boundary type generally result in highly stiff systems which are challenging to solve numerically.

The direct-forcing method developed by Mohd-Yusof [18] overcomes the numerical stiffness encountered by the immersed boundary method and several other penalty forcing techniques (see, e.g., [8]). The method implements the no-slip condition on the fluid momentum equations at the interface, so that the FSI force can be directly evaluated with the incorporation of the known structural interfacial velocity. Some recent work related to the direct-forcing method includes, among others, [9, 29, 34]. We note that most (if not all) direct-forcing techniques published so far are concerned with FSI problems involving rigid solid structures.

The main objective of this chapter is to combine the immersed boundary and the direct-forcing methods into a new, partitioned computational framework that enables accurate and efficient FSI computation and that allows realistic material representation of sophisticated

structures. Within this framework, Cartesian grids will be used for the majority of the computation, and the fluid and structure equations will be computed separately by their respective disciplinary solvers, typically with finite differences for the fluid domain and finite elements for the structure domain. In particular, a variety of structural geometries and configurations can be investigated and well-developed structural algorithms with detailed constitutive laws can be easily incorporated. The fluid and structural solutions are connected at the fluid-structure interface through a procedure based on an extension of the direct-forcing approach. These algorithms are thoroughly tested by a number of numerical simulations involving FSI problems with different material types such as rigid, elastic solid, and elastic thin-walled structures.

2.2 FLUID SYSTEM

We first describe the dynamics of the fluid part in our FSI problem. Below we present the governing equations of the fluid motion and the numerical treatment. We refer to [22] and references therein for a large body of work on computational fluid dynamics, particularly for solving Navier-Stokes equations. These equations are a set of time dependent highly non linear partial differential equations that describe the fluid flow. They can be seen as Newtons's second law of motion applied to a fluid parcel. The equations are usually solved together as a combination of the momentum and the continuity equation as seen in the next section. The Navier-Stokes equation represents the conservation of momentum, and the continuity equation represents the conservation of mass.

2.2.1 EQUATIONS OF MOTION

We consider a two-dimensional (2D) fluid domain, Ω^f, with an immersed solid domain, Ω^s (see Figure 2). Let Γ^s denote the fluid-structure interface. Let $[0, T]$ denote the time domain. The flow is assumed to be viscous and incompressible, and the motion is described by the standard Navier-Stokes equations

$$\rho^f(\frac{\partial \mathbf{u}}{\partial t} + \mathbf{u}\cdot\nabla\mathbf{u}) + \nabla p - \mu\nabla^2\mathbf{u} = \mathbf{f} \quad \text{in} \quad \Omega^{\mathrm{f}} \times [0, \mathrm{T}] \tag{1a}$$

$$\nabla\cdot\mathbf{u} = \mathbf{0} \quad \text{in} \quad \Omega^{\mathrm{f}} \times [0, \mathrm{T}] \tag{1b}$$

$$\mathbf{u}\,|_{t=0} = \mathbf{u_0} \quad \text{in} \quad \Omega^{\mathrm{f}} \tag{1c}$$

where $\mathbf{u}$ and p denote the fluid velocity and pressure, ρ^f and μ denote the fluid density and dynamic viscosity, respectively, and $\mathbf{f}$ is the external force. The terms in the equation (1a) refer to the inertial forces, pressure forces, viscous forces and external body forces. Equation (1b) is simplification of continuity equation in the context of constant density fluid flow. At the fluid-structure interface, we have the no-slip condition

$$\mathbf{u} = \mathbf{U}^s \quad \text{on} \ \ \Gamma^s \,. \tag{2}$$

Here $\mathbf{U}^s$ is the velocity of the structure immersed in the fluid, and Γ^s is the fluid-structure interface. In addition, we assume periodic boundary conditions on both the x and y directions of the fluid domain. Below we describe our numerical procedure for solving the fluid equations.

2.2.2 NUMERICAL CALCULATION

For ease of notations, we introduce the central difference operators on the Eulerian grids. Let $\mathbf{e}_1$, $\mathbf{e}_2$ be the standard basis of $\mathbf{R}^2$. For any vector $\boldsymbol{\varphi} = [\varphi_1 \ \varphi_2]$, and function $\varphi(\mathbf{x})$, $\mathbf{x} \in \Omega^f$, we define

$$(D_\beta \varphi)(\mathbf{x}) = \frac{\varphi(\mathbf{x} + h\mathbf{e}_\beta) - \varphi(\mathbf{x} - h\mathbf{e}_\beta)}{2h}, \qquad \beta = 1, 2 \tag{3a}$$

$$(L\boldsymbol{\varphi})(\mathbf{x}) = \sum_{\beta=1}^{2} \frac{\boldsymbol{\varphi}(\mathbf{x} + h\mathbf{e}_\beta) + \boldsymbol{\varphi}(\mathbf{x} - h\mathbf{e}_\beta) - 2\boldsymbol{\varphi}(\mathbf{x})}{h^2} \tag{3b}$$

where $h = \Delta x = \Delta y$. Let $\mathbf{D} = (D_1, D_2)$. The differential operators in the Navier-Stokes equations are then discretized as follows:

$$\nabla \cdot \boldsymbol{\varphi} \approx \mathbf{D} \cdot \boldsymbol{\varphi} = D_1\varphi_1 + D_2\varphi_2 \tag{4a}$$

$$\nabla \varphi \approx \mathbf{D}\varphi = (D_1\varphi, D_2\varphi) \tag{4b}$$

$$\nabla^2 \boldsymbol{\varphi} \approx L\varphi = L\varphi_1 + L\varphi_2 \tag{4c}$$

Since $\nabla \cdot \mathbf{u} = \mathbf{0}$, we have,

$$\mathbf{u} \cdot \nabla \varphi = \nabla \cdot (\mathbf{u}\varphi). \tag{5}$$

To take advantage of (5), a skew symmetric difference operator is employed to approximate

the convective term $\mathbf{u}\cdot\nabla\mathbf{u}$, which is denoted by S and defined as follows:

$$(S(\mathbf{u})\mathbf{u}) = \frac{1}{2}\mathbf{u}\cdot\nabla\mathbf{u} + \frac{1}{2}\nabla\cdot(\mathbf{u}\mathbf{u}) \sim \frac{1}{2}\mathbf{u}\cdot\mathbf{D}\mathbf{u} + \frac{1}{2}\mathbf{D}\cdot(\mathbf{u}\mathbf{u}). \tag{6}$$

As a result, equations (1a)(1b) can be spatially discretized as follows:

$$\rho^f\Big(\frac{\partial\mathbf{u}}{\partial t} + S(\mathbf{u})\mathbf{u}\Big) + \mathbf{D}p - \mu L\mathbf{u} = \mathbf{f}\,, \tag{7a}$$

$$\mathbf{D}\cdot\mathbf{u} = \mathbf{0}\,. \tag{7b}$$

For temporal discretization, implicit methods can be applied to equations (7a) and (7b) to ensure time-stepping stability. However, to treat the nonlinear terms, an iterative procedure is usually necessary. To reduce computational effort, fractional-step methods are widely used to calculate the incompressible Navier-Stokes equations. Here we adopt the fractional-step method presented in [20].

Assume that the solution is known at time t_n and $\mathbf{u}^n$ represents the solution of $\mathbf{u}$ at the n^{th} time step. At the preliminary (or, predictor) step, we solve for the intermediate variables $\mathbf{u}^{n+\frac{1}{2}}$ and $p^{n+\frac{1}{2}}$ by

$$\rho^f\Big(\frac{\mathbf{u}^{n+\frac{1}{2}} - \mathbf{u}^n}{\Delta t/2} + S(\mathbf{u}^n)\mathbf{u}^n\Big) + \mathbf{D}p^{n+\frac{1}{2}} - \mu L\mathbf{u}^{n+\frac{1}{2}} = \mathbf{f}^{n+\frac{1}{2}}, \tag{8a}$$

$$\mathbf{D}\cdot\mathbf{u}^{n+\frac{1}{2}} = \mathbf{0}. \tag{8b}$$

Then we update the solution at the corrector step; i.e., solve for $\mathbf{u}^{n+1}$ and $\mathbf{p}^{n+1}$, using

$$\rho^f\Big(\frac{\mathbf{u}^{n+1} - \mathbf{u}^n}{\Delta t} + S(\mathbf{u}^{n+\frac{1}{2}})\mathbf{u}^{n+\frac{1}{2}}\Big) + \mathbf{D}p^{n+1} - \mu L\big(\frac{\mathbf{u}^n + \mathbf{u}^{n+1}}{2}\big) = \mathbf{f}^{n+\frac{1}{2}}, \tag{9a}$$

$$\mathbf{D}\cdot\mathbf{u}^{n+1} = \mathbf{0}. \tag{9b}$$

To solve the system of equations (8 and 9), a Fast Fourier Transform is implemented [21]. In both the steps above, we need to solve linear systems of the form

$$(1 - \frac{\Delta t}{2}\frac{\mu}{\rho^f}L)\mathbf{u} + \frac{\Delta t}{2\rho^f}\mathbf{D}p = \mathbf{w}, \tag{10a}$$

$$\mathbf{D}\cdot\mathbf{u} = 0. \tag{10b}$$

where $\mathbf{w}$ refers to all the known terms, and $\mathbf{u}$ and p refer to the unknown velocity and pressure terms. The Discrete Fourier Transform of the above equations are given by (with $\widehat{\ }$ representing the Fourier space):

$$(1 - \frac{\Delta t}{2}\frac{\mu}{\rho^f}\widehat{L})\widehat{\mathbf{u}} + \frac{\Delta t}{2\rho^f}\widehat{\mathbf{D}}\widehat{p} = \widehat{\mathbf{w}}, \tag{11a}$$

$$\widehat{\mathbf{D}} \cdot \widehat{\mathbf{u}} = 0. \tag{11b}$$

Applying $\widehat{\mathbf{D}}\cdot$ to both sides of equation (11a) and making use of (11b), we get,

$$\widehat{p} = \frac{\widehat{\mathbf{D}} \cdot \widehat{\mathbf{w}}}{\frac{\triangle t}{2\rho^f}\widehat{\mathbf{D}} \cdot \widehat{\mathbf{D}}} \tag{12a}$$

Then with the pressure term known, we can calculate $\widehat{\mathbf{u}}$ as follows,

$$\widehat{\mathbf{u}} = \frac{\widehat{\mathbf{w}} - \frac{\triangle t}{2\rho^f}\widehat{\mathbf{D}}\widehat{p}}{(1 - \frac{\triangle t}{2}\frac{\mu}{\rho^f}\widehat{L})} \tag{12b}$$

Once solved, $\widehat{\mathbf{u}}$ and $\widehat{p}$ are transferred back to the physical space to obtain the solution $\mathbf{u}$ and p at the given time level.

2.3 STRUCTURE SYSTEM

We now present the structural part of the FSI problem. Although the computational framework proposed in this chapter can be applied to solid structures with various constitutive laws (e.g., linear elastic, hyperelastic, and viscoelastic), we will, for illustration, focus our attention on structures described by a linear elastic model. In what follows, we will describe the equations of motion and numerical treatment of the structural dynamics. As a primary emphasis of our work is to use disciplinary algorithms and codes to solve fluid and structural equations separately, we will employ the standard notations in solid mechanics when presenting the structure system below. We refer to [14] for a detailed explanation of equations and notations in solid mechanics.

2.3.1 EQUATIONS OF MOTION

We consider a linear isotropic elastic beam. Since the strains on the elastic beam are

small, we use the linear strain model to describe the deformations. In such an elastic domain Ω^s, the strain-displacement equation, the stress-strain relation and the dynamic equations of equilibrium state are given as follows:

$$\boldsymbol{\varepsilon} = \partial \boldsymbol{W}, \tag{13a}$$

$$\boldsymbol{\sigma} = \mathbf{D_e}\boldsymbol{\varepsilon}, \tag{13b}$$

$$\boldsymbol{\partial}^T\boldsymbol{\sigma} + \bar{\mathbf{b}} = \rho^s\ddot{\mathbf{W}} \tag{13c}$$

where $\boldsymbol{\varepsilon}$ is the strain, $\boldsymbol{\sigma}$ is the stress, $\mathbf{D_e}$ is the material stiffness matrix, ρ^s is the density of the structure, $\bar{\mathbf{b}}$ is the body force, $\mathbf{W}$ is the displacement, and $\dot{\mathbf{W}}$ and $\ddot{\mathbf{W}}$, respectively, denote the first and second time derivatives of $\mathbf{W}$. Specifically,

$$\boldsymbol{\sigma} = \begin{pmatrix} \sigma_x \\ \sigma_y \\ \tau_{xy} \end{pmatrix} = \begin{pmatrix} \sigma_{11} \\ \sigma_{22} \\ \sigma_{12} \end{pmatrix}, \quad \boldsymbol{\epsilon} = \begin{pmatrix} \epsilon_x \\ \epsilon_y \\ \gamma_{xy} \end{pmatrix} = \begin{pmatrix} \epsilon_{11} \\ \epsilon_{22} \\ 2\epsilon_{12} \end{pmatrix}, \quad \mathbf{W} = \begin{pmatrix} W_1 \\ W_2 \end{pmatrix}, \quad \bar{\mathbf{b}} = \begin{pmatrix} \bar{b}_1 \\ \bar{b}_2 \end{pmatrix},$$

$$\boldsymbol{\partial} = \begin{pmatrix} \frac{\partial}{\partial x} & 0 \\ 0 & \frac{\partial}{\partial y} \\ \frac{\partial}{\partial x} & \frac{\partial}{\partial y} \end{pmatrix}, \quad \text{and } \mathbf{D_e} = \frac{\mathrm{E}}{1-\nu^2} \begin{pmatrix} 1 & \nu & 0 \\ \nu & 1 & 0 \\ 0 & 0 & \frac{1-\nu}{2} \end{pmatrix},$$

where σ_x and σ_y are the orthogonal normal stresses relative to the co-ordinate system, τ_{xy} is the orthogonal shear stresses, ϵ_x and ϵ_y are the normal strain in the x and y direction, γ_{xy} is the shear strain, and E and ν are Young's modulus and Poisson's ratio respectively.

We write the boundary of the structure as $\Gamma^s = \Gamma^d \cup \Gamma^t$, where Γ^d refers to the fixed part of the boundary and Γ^t refers to the movable part. The boundary conditions are

$$\mathbf{W} = \mathbf{W}_0 \quad \text{on} \quad \Gamma^{\mathrm{d}}, \tag{14a}$$

$$\mathbf{n}\boldsymbol{\sigma} = \mathbf{T}_0 \quad \text{on} \quad \Gamma^{\mathrm{t}}, \tag{14b}$$

where

$$\mathbf{n} = \begin{pmatrix} n_1 & 0 & n_2 \\ 0 & n_2 & n_1 \end{pmatrix}$$

and (n_1, n_2) is the outward unit normal to the boundary. The initial displacement and velocity are given by

$$\mathbf{W}(\mathbf{x}, \mathbf{0}) = \mathbf{g}_1 \,, \tag{15a}$$

$$\dot{\mathbf{W}}(\mathbf{x}, 0) = \mathbf{g}_2 \,. \tag{15b}$$

These equations given in (13) are solved using the finite element method. The weak form is given by

$$\int_{\Omega^s} \boldsymbol{\sigma}^T \delta\boldsymbol{\varepsilon} \mathrm{d}v = \int_{\Gamma^t} \mathbf{T}_0^T \delta\mathbf{W} \mathrm{d}s + \int_{\Omega^s} \bar{\mathbf{b}}^T \delta\mathbf{W} \mathrm{d}v - \int_{\Omega^s} \rho^s \ddot{\mathbf{W}}^T \delta\mathbf{W} \mathrm{d}v, \tag{16}$$

where $\delta\mathbf{W}$ and $\delta\boldsymbol{\varepsilon}$ are arbitrary virtual displacement and strain fields respectively. The finite element approximation estimates the displacement vector by a linear combination of shape functions as

$$\mathbf{W}(\mathbf{x}, t) = \mathbf{N}(\mathbf{x}) \underline{\mathbf{W}}(t) \quad \text{and} \tag{17}$$

$$\ddot{\mathbf{W}}(\mathbf{x}, t) = \mathbf{N}(\mathbf{x}) \ddot{\underline{\mathbf{W}}}(t). \tag{18}$$

Here $\underline{\mathbf{W}}$ is the nodal displacement vector; i.e. displacement values at any finite element node and $\mathbf{N}$ is the interpolation function. Consequently, one has

$$\boldsymbol{\varepsilon} = \boldsymbol{\partial}\mathbf{W} = (\boldsymbol{\partial}\mathbf{N})\underline{\mathbf{W}} = \mathbf{B}(\mathbf{x})\underline{\mathbf{W}}, \tag{19}$$

where $\mathbf{B} = \boldsymbol{\partial}\mathbf{N}$ is the strain displacement matrix. And

$$\boldsymbol{\sigma} = \mathbf{D}_\mathbf{e}\boldsymbol{\varepsilon} = \mathbf{D}_\mathbf{e}\mathbf{B}(\mathbf{x})\underline{\mathbf{W}}. \tag{20}$$

Therefore, the virtual displacement and the virtual strain field are given by

$$\delta \mathbf{W} = \mathbf{N} \delta \underline{\mathbf{W}}, \tag{21}$$

$$\delta \boldsymbol{\varepsilon} = \mathbf{B} \delta \underline{\mathbf{W}}. \tag{22}$$

Substituting equations (19) and (21) in (16), we obtain the discretized weak form,

$$\begin{aligned} 0 &= \int_{\Omega^s} \rho^s \ddot{\mathbf{W}}^T \delta \mathbf{W} \mathrm{d}v + \int_{\Omega^s} \boldsymbol{\sigma}^T \delta \boldsymbol{\varepsilon} \mathrm{d}v - \int_{\Gamma^t} \mathbf{T}_0^T \delta \mathbf{W} \mathrm{d}s - \int_{\Omega^s} \bar{\mathbf{b}}^T \delta \mathbf{W} \mathrm{d}v \\ &= \ddot{\underline{\mathbf{W}}}^T \int_{\Omega^s} \mathbf{N}^T \mathbf{N} \delta \underline{\mathbf{W}} \mathrm{d}v + \underline{\mathbf{W}}^T \int_{\Omega^s} \mathbf{B}^T \mathbf{D_e} \mathbf{B} \delta \underline{\mathbf{W}} \mathrm{d}v - \int_{\Gamma^t} \mathbf{T}_0^T \mathbf{N} \delta \underline{\mathbf{W}} \mathrm{d}s - \int_{\Omega^s} \bar{\mathbf{b}}^T \mathbf{N} \delta \underline{\mathbf{W}} \mathrm{d}v \\ &= (\ddot{\underline{\mathbf{W}}}^T M^T + \underline{\mathbf{W}}^T K^T - \mathbf{f}_t^T - \mathbf{f}_b^T) \delta \underline{\mathbf{W}} \\ &= \delta \underline{\mathbf{W}}^T (M \ddot{\underline{\mathbf{W}}} + K \underline{\mathbf{W}} - \mathbf{f}_t - \mathbf{f}_b). \end{aligned} \tag{23}$$

The derivation above is done by defining its integrals in terms of the mass matrix, the stiffness matrix, the surface force term and the body force term, M, K, $\mathbf{f}_t$ and $\mathbf{f}_b$, respectively, as

$$\begin{aligned} \int_{\Omega^s} \mathbf{N}^T \mathbf{N} \mathrm{d}v &= M^T, \\ \int_{\Omega^s} \mathbf{B}^T \mathbf{D_e} \mathbf{B} \mathrm{d}v &= K^T, \\ \int_{\Gamma^t} \mathbf{T}_0^T \mathbf{N} \mathrm{d}s &= \mathbf{f}_t^T, \\ \int_{V} \bar{\mathbf{b}}^T \mathbf{N} \mathrm{d}v &= \mathbf{f}_b^T. \end{aligned}$$

Equation (23) results in a matrix equation for the motion:

$$M \ddot{\underline{\mathbf{W}}} + K \underline{\mathbf{W}} - \mathbf{f}_t - \mathbf{f}_b = 0 \tag{24}$$

with consistent boundary and initial conditions.

2.3.2 NUMERICAL CALCULATION

We rewrite the dynamic equation (24) in the form as

$$M\ddot{\underline{\mathbf{W}}} + K\underline{\mathbf{W}} - \mathbf{f}_b = \mathbf{F}(t), \tag{25}$$

where $\mathbf{F}(t)$ is emphasized as the force load acting on the boundary of the structure. Equation (25) is solved based upon the modal synthesis approach in which the displacement vector is approximated by modal superposition. That is, the dynamic response $\underline{\mathbf{W}}$ is expanded as a linear combination of eigenvectors with weighted coefficients $\mathbf{a}(t)$; i.e.

$$\underline{\mathbf{W}} = \boldsymbol{\psi}\mathbf{a}(t). \tag{26}$$

The columns of the matrix $\boldsymbol{\psi}$ are the eigenvectors of the eigenvalue problem pertaining to the equation of motion,

$$K\boldsymbol{\psi} = \Lambda M\boldsymbol{\psi}, \tag{27}$$

where the eigenvectors $\boldsymbol{\psi}$ satisfy the orthonormal conditions $\boldsymbol{\psi}^T K\boldsymbol{\psi} = \Lambda$ and $\boldsymbol{\psi}^T M\boldsymbol{\psi} = \mathbf{I}$, and Λ is the diagonal matrix consisting of the eigenvalues of the problem.

Substituting (26) in (25), we obtain

$$M\boldsymbol{\psi}\ddot{\mathbf{a}}(t) + K\boldsymbol{\psi}\mathbf{a}(t) - \mathbf{f}_b = \mathbf{F}(t). \tag{28}$$

Multiplying the above equation by $\boldsymbol{\psi}^T$, we obtain

$$\boldsymbol{\psi}^T M\boldsymbol{\psi}\ddot{\mathbf{a}}(t) + \boldsymbol{\psi}^T K\boldsymbol{\psi}\mathbf{a}(t) - \boldsymbol{\psi}^T\mathbf{f}_b = \boldsymbol{\psi}^T\mathbf{F}(t). \tag{29}$$

The dynamic equation can then be decoupled into a set of ordinary differential equations as

$$\ddot{\mathbf{a}}(t) + \Lambda\mathbf{a}(t) - \boldsymbol{\psi}^T\mathbf{f}_b = \boldsymbol{\psi}^T\mathbf{F}(t). \tag{30}$$

In this study, a one-step implicit Newmark method [1] is used to solve equation (30). It can be summarized as follows:

Assume that $\mathbf{a}_{n-1}$, $\dot{\mathbf{a}}_{n-1}$, $\ddot{\mathbf{a}}_{n-1}$ at time t_{n-1} are known. The Newmark method extrapolates $\mathbf{a}_n$ and $\dot{\mathbf{a}}_n$, at time $t_n = t_{n-1} + \Delta t$ in terms of $\ddot{\mathbf{a}}_n$ as

$$\dot{\mathbf{a}}_n = \dot{\mathbf{a}}_{n-1} + \Delta t[(1-\alpha)\ddot{\mathbf{a}}_{n-1} + \alpha\ddot{\mathbf{a}}_n], \tag{31a}$$

$$\mathbf{a}_n = \mathbf{a}_{n-1} + \Delta t\dot{\mathbf{a}}_{n-1} + \Delta t^2\left[\left(\frac{1}{2}-\beta\right)\ddot{\mathbf{a}}_{n-1} + \beta\ddot{\mathbf{a}}_n\right]. \tag{31b}$$

The above approximation corresponds to the linear acceleration method if $\alpha = \frac{1}{2}$ and $\beta = \frac{1}{6}$, and the constant average acceleration method if $\alpha = \frac{1}{2}$ and $\beta = \frac{1}{4}$. We use the latter one which is unconditionally stable.

At time t_n , equation (30) becomes,

$$\ddot{\mathbf{a}}_n + \Lambda\mathbf{a}_n - \boldsymbol{\psi}^T\mathbf{f}_{b,n} = \boldsymbol{\psi}^T\mathbf{F}_n. \tag{32}$$

Substituting equations (31) into equation (32), we obtain

$$\ddot{\mathbf{a}}_n = (I + \Lambda\beta\Delta t^2)^{-1}\left[\boldsymbol{\psi}^T(\mathbf{F}_n + \mathbf{f}_{b,n}) - \Lambda\left(\mathbf{a}_{n-1} + \Delta t\dot{\mathbf{a}}_{n-1} + \Delta t^2\left(\frac{1}{2}-\beta\right)\ddot{\mathbf{a}}_{n-1}\right)\right]. \tag{33}$$

Once $\ddot{\mathbf{a}}_n$ is found, equations(31) can be used to find $\mathbf{a}_n$ and $\dot{\mathbf{a}}_n$. The displacement and velocity at the finite element nodes are then computed by

$$\underline{\mathbf{W}}_n = \boldsymbol{\psi}\mathbf{a}_n, \tag{34a}$$

$$\dot{\underline{\mathbf{W}}}_n = \boldsymbol{\psi}\dot{\mathbf{a}}_n. \tag{34b}$$

The magnitude of the von Mises stresses is often calculated to measure the strength of the structure, and is an important factor for structure design consideration. The stresses at each node can be calculated based on equations (34) and (19). The displacement $\underline{\mathbf{W}}_n$ at the boundary reveals the deformed position of the structure. The velocity $\dot{\underline{\mathbf{W}}}_n$ at the boundary; i.e., $\mathbf{U}^s$, is then passed to the fluid code. Also, since the structural part is solved in Lagrangian co-ordinate we do not require any additional mapping for the structural velocity. In the remainder of this section, we describe the procedure to calculate the required stresses in the above presented framework.

Once the time history of the elastic displacement is obtained, we can then proceed to

compute the dynamic stresses. This can be done using the known mode shapes of the given structure $\boldsymbol{\psi}$ and the modal coordinates $\mathbf{a}$ from the solution of equation (31b). The modal superposition can be applied here to find the total stresses, $\boldsymbol{\sigma}^{\boldsymbol{T}} = \begin{pmatrix} \sigma_x & \sigma_y & \tau_{xy} \end{pmatrix}$. The combination of equations (26) and (17a) describes the displacement field in the structure in terms of modal coordinates as

$$\mathbf{W}(\mathbf{x}, t) = \mathbf{N}(\mathbf{x})\boldsymbol{\psi}\mathbf{a}(t).$$

The state of stresses at any point, $\mathbf{x}$, in the structure is then obtained as, according to equations (13a) and (13b),

$$\begin{aligned} \boldsymbol{\sigma}(\mathbf{x}, t) &= \mathbf{D_e}\boldsymbol{\varepsilon}(\mathbf{x}) && (35) \\ &= \mathbf{D_e}\boldsymbol{\partial}\mathbf{W}(\mathbf{x}) && (36) \\ &= \mathbf{D_e}(\boldsymbol{\partial}\mathbf{N}(\mathbf{x}))\boldsymbol{\psi}\mathbf{a}(t). && (37) \end{aligned}$$

Since the material properties $\mathbf{D_e}$, the differential operator $\boldsymbol{\partial}$, the finite element interpolation function and the mode shapes are known before starting the FSI solution process, the relationship between the stresses $\boldsymbol{\sigma}$ and the modal coordinates can be defined as,

$$\begin{aligned} \boldsymbol{\sigma}(\mathbf{x}, t) &= [\mathbf{D_e}(\boldsymbol{\partial}\mathbf{N}(\mathbf{x}))\boldsymbol{\psi}]\mathbf{a}(t) && (38) \\ &= \mathbf{B}(\mathbf{x})\mathbf{a}(t) && (39) \end{aligned}$$

Once the normal stresses σ_x , σ_y and the shear stress τ_{xy} are known, one can then use the following equation to find the von Mises stress

$$\boldsymbol{\sigma}_{\nu,c} = \sqrt{\sigma_x^2 + \sigma_y^2 - \sigma_x\sigma_y + 3\tau_{xy}^2}$$

Collection of the von Mises stresses at the centers of all elements can be used to find the von Mises stress distribution over the entire finite element model. As mentioned earlier, values of the von Mises stresses are often required as an output of an analysis to measure the capability of the structure failure to sustain the given load in any engineering design.

2.4 FLUID-STRUCTURE INTERACTION

As discussed above, our computational framework allows that the fluid and structural motions are solved separately by their disciplinary methods, and their solutions now need to be connected at the interface where the fluid-structure interaction takes place. The FSI forces represent the physical interaction between the fluid and solid. Similar to the velocity and the pressure fields, this variable is unknown and needs to be calculated. In the original framework developed by Peskin, force on the elastic boundary is computed by

$$\mathbf{F} = -\frac{\partial E}{\partial \mathbf{X}}, \tag{40}$$

where E is the elastic energy of the material. In general, it may be sufficient to use the Hooke's law in many situations like the linear elastic model

$$\mathbf{F} = -\kappa(\mathbf{X} - \mathbf{X}_e). \tag{41}$$

The boundary points $\mathbf{X}$ is connected to a fixed equilibrium points $\mathbf{X}_e$ with a stiff spring. The spring acts as a force to hold the boundary points together when they fall out of desired place. For rigid bodies, the problem may result in stiff system of equations due to large value of the stiffness constant κ. Goldstein et al. [8] used a feedback forcing approach applied at Lagrangian grid to enforce no slip condition at the immersed boundary as follows:

$$\mathbf{F}(\mathbf{s}, \mathbf{t}) = \alpha \int_0^t \mathbf{U}(s, \tau)\, \mathrm{d}\tau + \beta \mathbf{U}(\mathrm{s}, \tau) \tag{42}$$

The issue with this method, similar to previous forcing terms, is that large values of α and β which can lead to stiff equations; in addition to the problem of uncertainties among the parameters. Moreover, this type of feedback forcing method may generate spurious oscillations and restrict computational time steps for stability. An alternative way of expressing the forcing term f which does not suffer from the previous limitations is the direct forcing method. Below we describe the details of our numerical technique to link the fluid and structural dynamics using the direct-forcing approach.

2.4.1 CALCULATION OF FSI FORCES

The original direct-forcing technique by Mohd-Yusof was implemented in Cartesian grids where the force was calculated directly from the Navier-Stokes equations [18] in order to avoid artificial parameters and stiffness issues. The proposed method imposed direct forcing by replacing $\mathbf{U}_{n+1}$ by $\mathbf{U}_s$ in the Navier Stokes equations. Alternatively, the force can be evaluated at the Lagrangian grid points, as suggested by Uhlmann [29]. We adopt the latter approach in the current study with some modifications as shown below. This works well with moving moving boundary problems as it avoids large oscillations towards the force. Let $\mathbf{U}^n$ and P^n denote, respectively, the fluid velocity and pressure evaluated on the Lagrangian grids. Our forcing term $\mathbf{F}^{n+1}$ takes the form

$$\mathbf{F}^{n+1} = \begin{cases} \rho^f [\dfrac{\mathbf{U^s} - \mathbf{U}^n}{\Delta t} + ((\mathbf{U} \cdot \nabla)\mathbf{U})^n] + \nabla P^n - \mu \nabla^2 \mathbf{U}^n & \text{on} \quad \Gamma^s \\ \mathbf{0} & \text{elsewhere.} \end{cases} \tag{43}$$

This forcing is direct because the desired structural velocity is imposed directly on the boundary of the body. So at each time step, the boundary condition criteria is enforced exactly. The forcing term $\mathbf{F}$ using this direct forcing method also functions as a velocity corrector for the grid points inside the IB. The force $\mathbf{F}$ is passed to the structure code acting as the force load on the right-hand side of equation (25). Once equation (25) is solved, the structural displacement and velocity fields, particularly the interfacial velocity $\mathbf{U}^s$, are updated. Meanwhile, the force $\mathbf{F}$ is interpolated to the Eulerian grid so as to solve the Navier-Stokes equations and update the fluid motion. The interpolation is done through a discrete delta function, described below. Once the interpolation is completed, the forcing term $\mathbf{f}$ on the right-hand side of the fluid momentum equations is obtained.

2.4.2 INTERPOLATION FUNCTIONS

The location of the moving solid boundary usually does not coincide with the solution at the Eulerian grid. Hence a proper interpolation or distribution of force is required. The simplest possibility is to select the grid point nearest to the boundary. Several linear interpolation methods have also been investigated in the past. For this study, however, the interaction between the Eulerian grid and the Lagrangian grid will be achieved by a smooth approximation of the Dirac Delta function. A 2D discrete delta function, denoted δ_h, is

typically given by the product of two 1D discrete delta functions,

$$\delta_h = \frac{1}{h^2}\phi(\frac{x}{h})\phi(\frac{y}{h})$$

where $h = \Delta x = \Delta y$. The following properties are satisfied by such a regularized delta function, $\phi(r)$, where r denotes $\frac{x}{h}$, or $\frac{y}{h}$.

- ϕ is continuous for all r ,
- $\phi(r) = 0$ for $|r| \geq 2$,
- $\sum_{i\ even} \phi(r-i) = \sum_{i\ odd} \phi(r-i) = \frac{1}{2}$,
- $\sum_i (r-i)\phi(r-i) = 0$,
- $\sum_i (\phi(r-i))^2 = c$,

where c is a constant and r is any real variable. Here we use the function ϕ introduced by Peskin [20], which was used to interpolate fluid velocity to the boundary velocity.

$$\phi(x) = \frac{1}{8}\begin{cases} 3 - 2|x| + \sqrt{1 + 4|x| - 4x^2} & : |x| \leq 1 \\ 5 - 2|x| - \sqrt{-7 + 12|x| - 4x^2} & : 1 \leq |x| \leq 2 \\ 0 & : |x| \geq 2. \end{cases}$$

The distribution of forces from Lagrange to Euler grids and the interpolation of velocities from Euler to Lagrange grids are then represented as follows [29]:

$$\mathbf{f}(\mathbf{x}_{ij}) = \sum_l \mathbf{F}(\mathbf{X}_l) \cdot \delta_h(\mathbf{x}_{ij} - \mathbf{X}_l)\Delta V_l, \tag{44}$$

$$\mathbf{U}(\mathbf{X}_l) = \sum_{i,j} \mathbf{u}(\mathbf{x}_{ij}) \cdot \delta_h(\mathbf{x}_{ij} - \mathbf{X}_l)h^2, \tag{45}$$

where ΔV_l is the discrete volume at each Lagrangian point.

Interpolation/distribution of other quantities can be done in a similar way.

2.4.3 FLUID-STRUCTURE COUPLING

In a typical computational procedure for fluid-structure interaction based on the immersed boundary approach, the fluid and structure parts are solved sequentially (see, e.g., [20, 24]). Such an algorithm generally contains the following basic steps:

- Calculate the FSI forces at the fluid-structure interface.
- Distribute the forces from the interface to the background Eulerian grids.
- Solve the Navier-Stokes equations on the Eulerian grids with the forcing term.
- Interpolate the fluid velocity from the background Eulerian grids to the interfacial Lagrangian grids.
- Advance the structural positions (particularly at the interface) with the updated velocity.

Our numerical approach will integrate the immersed boundary method and the direct-forcing technique into a new, partitioned framework, based on which well-developed disciplinary methods can be employed to solve the fluid and structural motions and their solution data only communicate at the fluid-solid interface. This approach will extend the immersed boundary method to the computation of more realistic solid structures that occupy finite volumes, and will extend the direct-forcing technique toward dealing with more general, elastic materials described by detailed constitutive laws. Key steps of our FSI algorithm are summarized below, where the emphasis is put on the fluid-structure coupling. We assume that at $t = t_{n+1}$, the fluid velocity u^n and pressure p^n (defined on the Eulerian grids) and the structural boundary position $\Gamma^{s,n}$ are known. We again let $\mathbf{U}^n$ and P^n denote the fluid velocity and pressure evaluated on the Lagrangian grids at the time t_n .

1. Use the known information on u^n, p^n and $\Gamma^{s,n}$ to compute $\mathbf{U}^n$, $((\mathbf{U} \cdot \nabla)\mathbf{U})^n$, $\nabla^2\mathbf{U}^n$, and ∇P^n on the structural boundary through interpolation from the Eulerian grids to the Lagrangian grids.
2. Calculate the forces $\mathbf{F}^{n+1}$ on the Lagrangian grids using the direct-forcing approach (see equation 43).

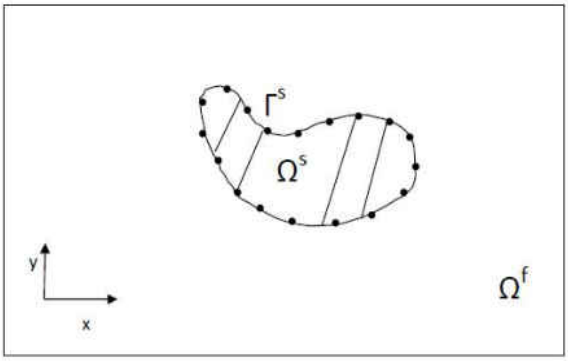

FIG. 2: Fluid-structure domain.

3. Distribute the forces from the interface to the fluid domain to obtain $\mathbf{f}^{n+1}$.

4. Compute the Navier-Stokes equation. Also calculate $\mathbf{u}^{n+1}$, $((\mathbf{u}\cdot\nabla)\mathbf{u})^{n+1}$, $\nabla^2\mathbf{u}^{n+1}$, and ∇p^{n+1} for the next time step.

5. Pass the force $-\mathbf{F}^{n+1}$ as the load to the structural solver.

6. Solve the structural system at $t = t_{n+1}$; particularly, obtain the boundary displacement $\mathbf{W}^{s,n+1}$ and velocity $\mathbf{U}^{s,n+1}$.

7. Update the fluid-structure interface with the updated structural displacement obtained from the structure code; e.g., $\Gamma^{s,n+1} = \Gamma^{s,n} + \mathbf{W}^{s,n+1}$.

8. Pass the updated fluid velocity $\mathbf{u}^{n+1}$ and pressure p^{n+1}, interface location $\Gamma^{s,n+1}$ and structural velocity $\mathbf{U}^{s,n+1}$ to the next step of computation.

2.5 EXAMPLES

A structure (rigid or flexible) is fully immersed in the fluid. See Figure 2. Any naturally existing fluid structure interaction problem comprises of fluid forces exerted on the solid body and the motion of the structure affecting the fluid flow. We present four examples to demonstrate our numerical algorithms. The first one is the canonical problem of viscous flow past a rigid circular cylinder. We will compare our numerical findings with published

results. We also tested the usual moving rigid cylinder with fixed velocity and got very good results. However, instead of presenting that problem, we choose to present a new variation of a moving circular cylinder problem. See example 2 for details. The third example is a more complex problem with viscous flow past an elastic and deformable solid beam. We will pay special attention to the movement and deformation of the solid structure under the impact of fluid flow. The fourth example, computationally most challenging, is concerned with viscous flow past an elastic and deformable hollow beam, where complex interaction occurs between the fluid flow and the thin-walled structure.

2.5.1 FLOW PAST A RIGID CYLINDER

We first verify our method for the well-known problem of 2D viscous flow past a rigid cylinder. In this case, though, the structure solver is not needed; Γ^s remains unchanged and $\mathbf{U}^s = 0$. The step sizes used for this simulation are $\Delta t = 10^{-4}$, $\frac{\Delta q}{h} = 0.5$ where Δq and h are Lagrangian and Eulerian grid size respectively in a computational domain of [0,14] $\times$ [0,14]. Under the standard setting, we compare the drag coefficient and the length of the eddies to those in the literature. The drag coefficient is a dimensionless quantity used to calculate the drag or resistance of an object in a fluid flow. The results are presented in Table 1. The drag coefficient in 2D is calculated using the formula,

$$C_D = \frac{2F_x}{\rho^f u^2 D} \tag{46}$$

where F_x is the x component of the fluid force acting on the cylinder, and D is the diameter of the cylinder. The Reynolds number, which is the ratio of inertial forces to viscous forces, Re is given by

$$\mathrm{Re} = \frac{\rho^f u D}{\mu}.$$

We observe good agreement between our numerical measurement and published results. Meanwhile, Figure 3 shows the streamline plots of the flow with different Reynolds numbers. We clearly observe three distinct types of flow behaviors: when Re is very low, the flow is symmetric and steady, and no wakes form in the tail region; when Re is in an intermediate range (typically between 5 and 40), a pair of vortices in wakes are observed and the length of the eddies increases with Re; when Re grows even larger (e.g., 100), the motion becomes asymmetric and unsteady, and the wakes evolve into vortex streets.

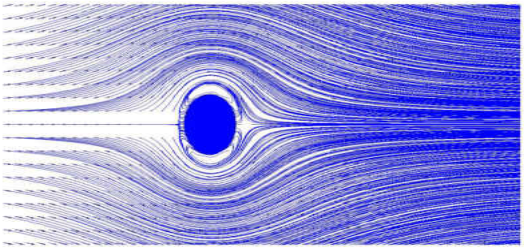

(a) Re=0.1

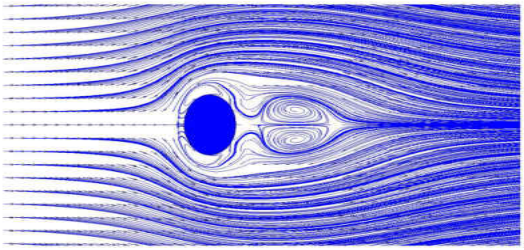

(b) Re=30

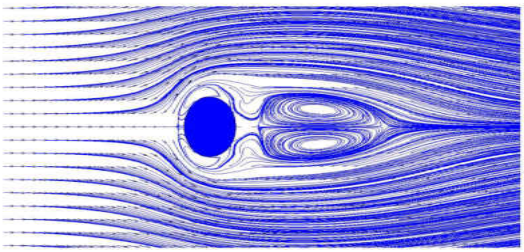

(c) Re=40

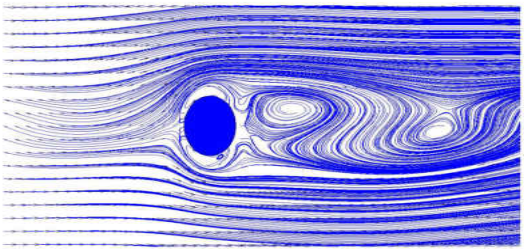

(d) Re=100

FIG. 3: Streamline visualization with different Reynolds numbers for the flow past a rigid cylinder.

TABLE 1: Comparison of the wake lengths and drag coefficients.

Re=20	L	C_D
Fornberg [7]	0.91	2
Dennis and Chang [3]	0.94	2.05
Donna Calhoun [2]	0.94	2.05
Taira and Colonius [28]	0.97	2.07
Present	0.9	2

Re=40	L	C_D
Fornberg [7]	2.24	1.50
Dennis and Chang [3]	2.35	1.52
Donna Calhoun [2]	2.18	1.62
Taira and Colonius [28]	2.33	1.55
Present	2.36	1.54

2.5.2 A RIGID BALL THROWN IN AN OPPOSITE DIRECTION TO THE FLUID FLOW.

A ball of radius 0.5 is propelled into the fluid with some initial velocity $\mathbf{V}_0(= \mathbf{U}^{s0})$ in the opposite direction of the flow. We analyze the movement of the ball in the fluid flow and the time taken by the ball to reverse it's direction and hence move along with the flow.

A direct forcing Immersed boundary method as described in earlier section is used. For the first time step(t_1), the position of the ball is updated using the prescribed initial velocity. This assumption is valid since for small Δt, it is reasonable to assume the structure velocity to be the same at t_0 and $t_0+\Delta t$. After the second time step, the no-slip condition is used. The velocity of the fluid $\mathbf{u}(t_n)$ at a given time step is interpolated to get $\mathbf{U}(t_n)$ in the Lagrangian grid. All the nodes in the ball is then uniformly assigned the same velocity of the fluid at one node of the ball in order to restrict the deformation of the ball. The parameters used for this simulation are $\Delta t = 10^{-4}$, $\frac{\Delta q}{h} = 0.5$, $\rho^f = 1$, $\mu = 1$, and a computational domain of [0,14] $\times$ [0,14]. The fluid flow is assigned an uniform initial velocity of $\mathbf{u}_0 = 10$. For different initial ball velocities, Figure 5 shows the gradual change in the velocity of the ball as it eventually moves along with the flow. The second plot in Figure 5 gives us a closer look at the time

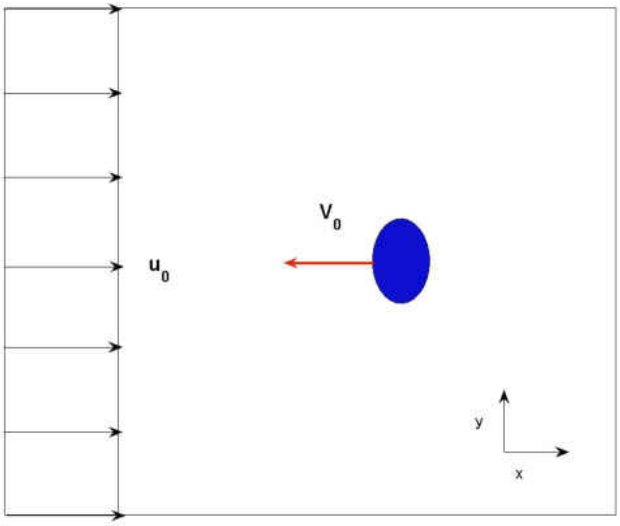

FIG. 4: Ball with an initial velocity in the opposite direction of the flow

when the ball changes its direction from negative to positive, i.e. to the direction of the flow. For example, if the initial velocity of the ball is -10, it takes $0.015s$ for the ball to change its direction and move with the flow. With a much higher initial velocity of -90, it takes the ball a much longer time of $0.1s$ to change direction.

The higher the velocity of the ball in the opposite direction of the flow, the more time it takes to change it's direction to that of the fluid flow. Figure 6 shows this phenomena for three different initial velocities of the fluid flow. Also, the higher the initial velocity of the fluid flow,the faster the change in the direction of the ball movement, which is as expected.

2.5.3 FLOW PAST AN ELASTIC SOLID BEAM

In this problem, a 30×3 (in^2) elastic beam is immersed in a viscous fluid. The bottom of the beam is fixed, whereas other parts of the beam are movable and deformable. The parameters characterizing material properties of the beam are listed in Table 2. We consider ten mode shapes of the elastic beam to form the eigenvector matrix $\boldsymbol{\psi}$ in equation (26); these ten modes are visualized in Figure 8. The corresponding eigenvalues and frequencies of each

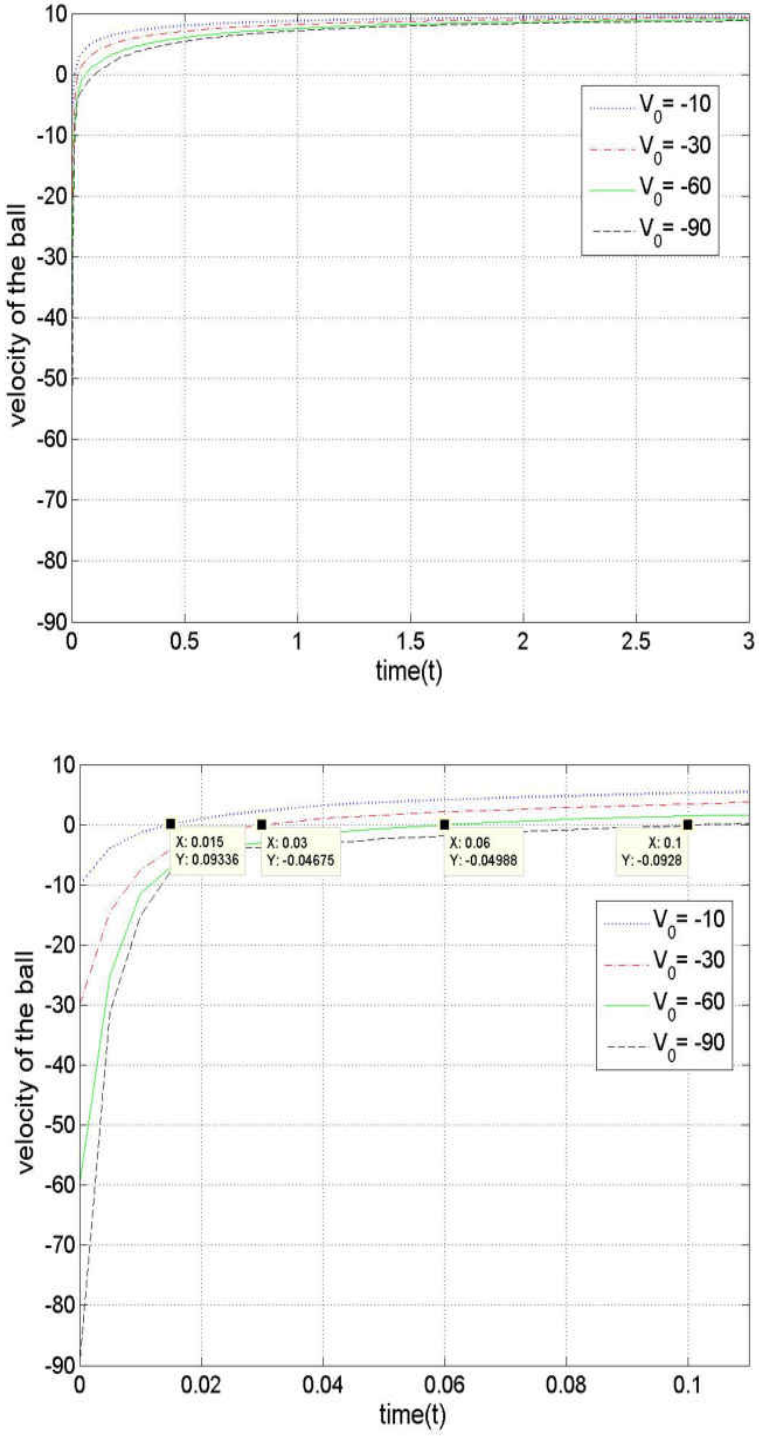

FIG. 5: Velocity of the ball over time with different initial velocities $\mathbf{V}_0$

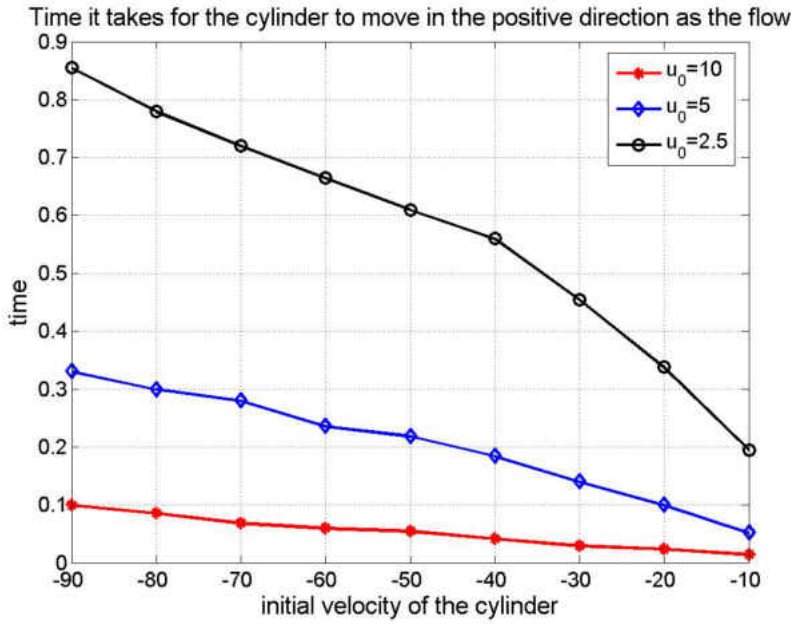

FIG. 6: Time it takes for the cylinder to move in the positive direction as the flow under different intial fluid flows $\mathbf{u}_0$

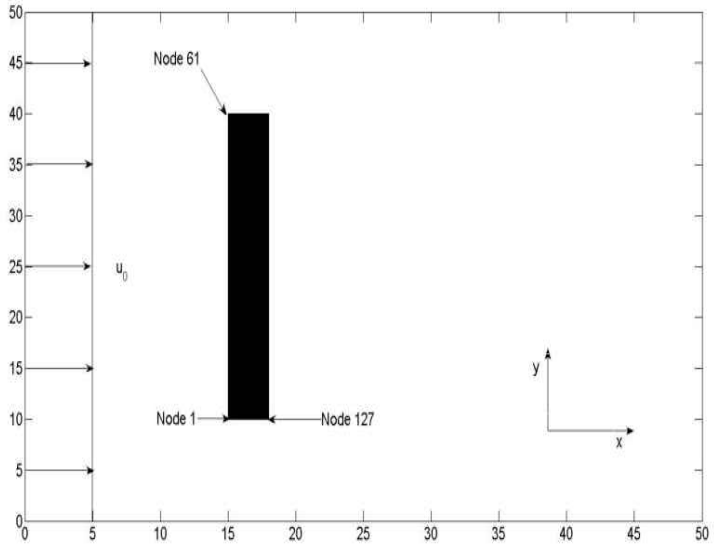

FIG. 7: Fluid-structure interaction diagram of an elastic beam.

TABLE 2: Material parameters for the elastic beam.

Young's modulus	Poisson's ratio	density	thickness
3.0E+09 psi	0.3	284 lb/in^3	0.125 in

TABLE 3: Eigenvalues and frequencies of the ten modes of the solid beam.

Mode	Eigenvalue, λ	Frequency
1	1.19E+03	5.5
2	4.30E+04	33
3	2.90E+05	85.8
4	2.98E+05	86.9
5	9.85E+05	158
6	2.29E+06	241
7	2.61E+06	257
8	4.34E+06	332
9	7.21E+06	427
10	7.21E+06	427

mode are listed in Table 3. The dynamic responses of the beam is subject to the transient force $\mathbf{F}(t)$ induced by the surrounding fluid.

The beam is discretized into 720 triangular elements with 427 nodes. Starting from the lower left corner, we index the structure boundary from 1 to 127 (61 points on each of the left and right sides and 5 on the top); see Figure 7. These 127 nodes are used to communicate data between the structure code and the fluid code. Initially, the structure is at rest, and the fluid motion is set as parallel flow with a constant velocity $\mathbf{u_0}$. The fluid solver calculates $\mathbf{F}$ using the Direct Forcing Approach and passes $\mathbf{F}$ to the structure code; the structural motion is computed using the Newmark method [1]. It then returns the structural velocity $\mathbf{U}^s$ at the boundary nodes(127 in total) to the fluid code.

Through the interaction with the fluid flow, the beam oscillates on the horizontal direction (left and right). Note again that the bottom of the beam is fixed. In Figure 9, we highlight the vibration and deformation of the beam over time. The computational domain here is set

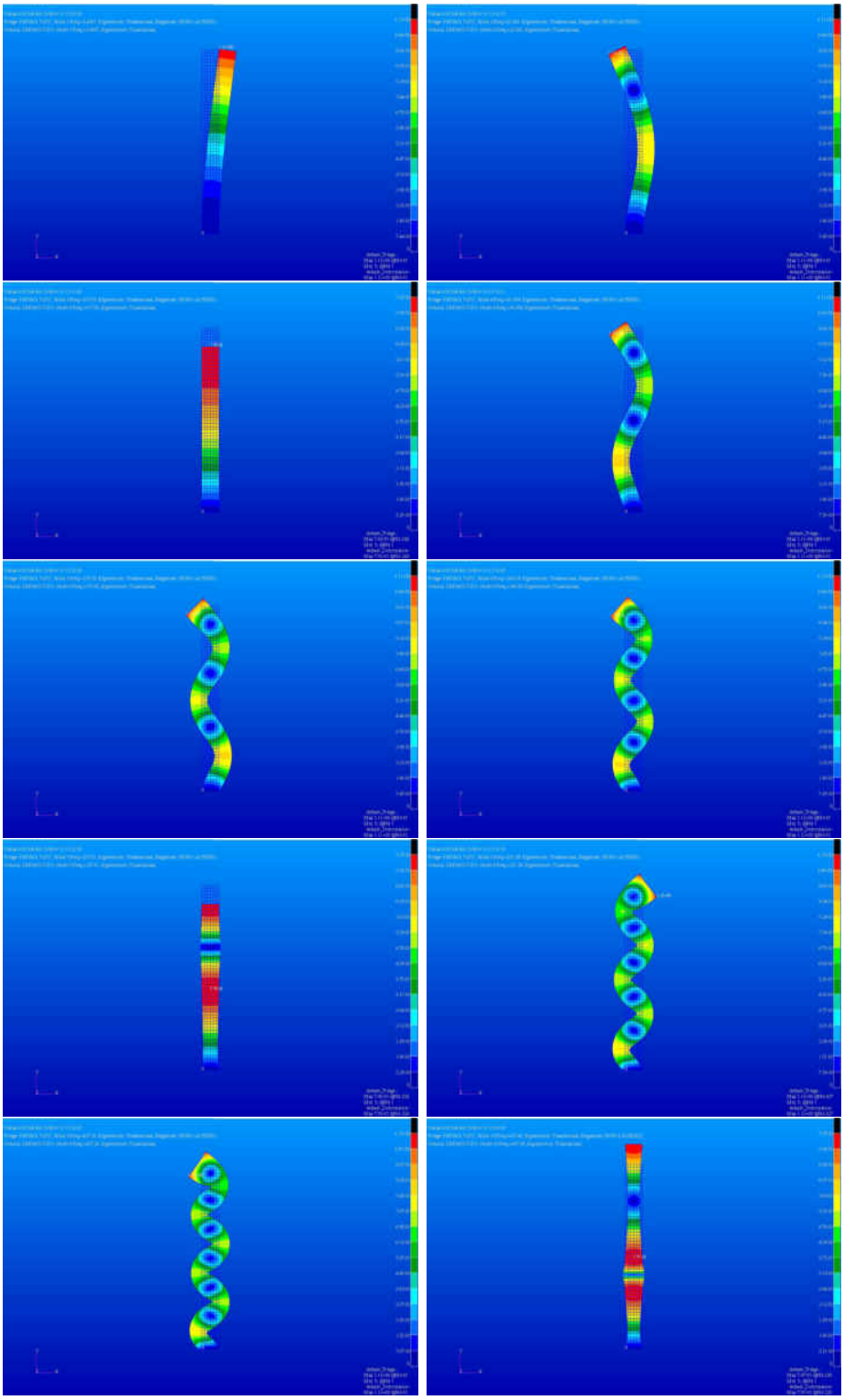

FIG. 8: Ten mode shapes of the elastic solid beam.

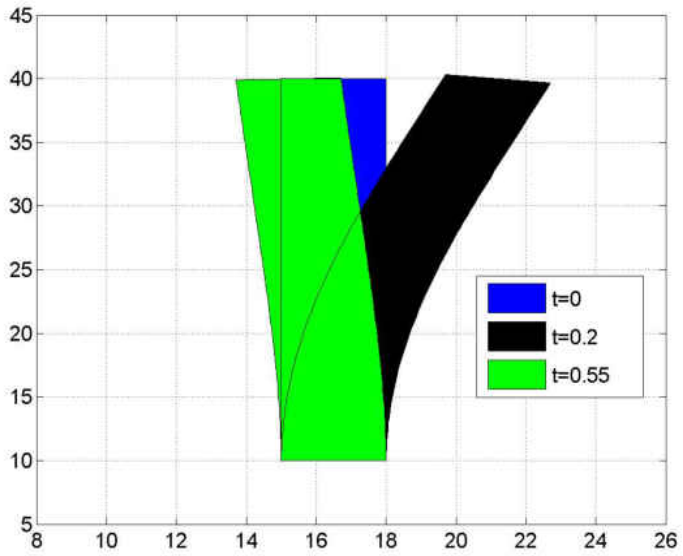

FIG. 9: Movement of the solid beam.

as $[0, 50] \times [0, 50]$ which, we have found, is large enough so that the fluid boundary does not play a role in the structural motion. The other parameters for the simulation are $\mu = 0.1$, $\mathbf{u}_0 = 50$, $\rho^f = 1.5$, $\frac{\Delta q}{h} = 0.64$, and $\Delta t = 0.001$. As can be naturally expected, the beam has a larger displacement in the direction of the flow and a smaller displacement in the opposite way.

Figure 10 illustrates the case of larger deformations with a more flexible body, where the Young's modulus E is decreased by 100 times; i.e., $E = 3 \times 10^7$ psi, to make the beam softer and more deformable.

In Figure 11, we visualize the flow field and the structural stresses at different times. The structural stresses are obtained based upon equation (38) described in Section 2.3.2. We observe that a vortex is formed near the fixed end of the beam shortly after the flow starts, and another vortex is created near the other end later as the beam starts coming back to the original position. In order to examine the dynamics more carefully, we pick a particular tip of the beam at the free end; i.e., node 61 for the upper left corner of the beam, and look into its detailed motion. Figure 12 shows the displacement of this node over a long period of time, where we clearly observe a regular oscillation with decaying amplitude over time. Moreover, the oscillation in the positive direction (i.e., the direction of the fluid

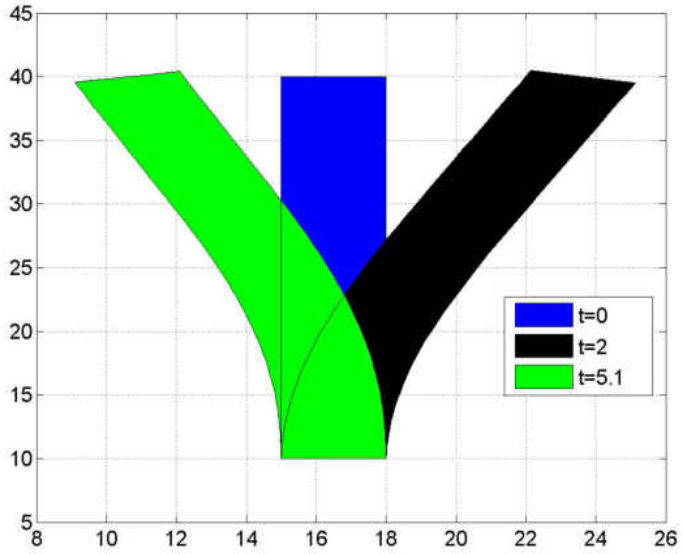

FIG. 10: Larger displacement with a more elastic body.

flow) has larger amplitude than that in the negative (i.e., opposite) direction. The fluid parameters used in this simulation are $\mu = 0.1$, $\mathbf{u}_0 = 10$, and $\rho^f = 0.5$. Figure 13 compares the displacement of the 61^{st} node over one cycle for different choices of Δt , and we observe close agreement of these curves.

As a means to verify our methods and results, we have also conducted the numerical simulation using a different approach proposed by Zhang et al. [34]. This method calculates the FSI force $\mathbf{F}$ based on a predictor-corrector procedure using an intermediate fluid velocity. The method originally employs stream functions, and we have generated a variant using the velocity-pressure formulation which seems more suitable for our simulation and comparison. For this method, we calculate an intermediate velocity $\mathbf{u}^*$ and interpolate it to the Lagrangian grid to obtain $\mathbf{U}^*$. Then, the force at the interface is calculated using two steps as shown below,

$$\mathbf{F}'^n = (\frac{\mathbf{U}^s - \mathbf{U}^*}{\triangle t})\triangle q \tag{47a}$$

$$\mathbf{F}^n = \mathbf{F}'^n + \mathbf{F}^{n-1}. \tag{47b}$$

For distinction, we refer to the algorithm originated from [34] as described above as Method

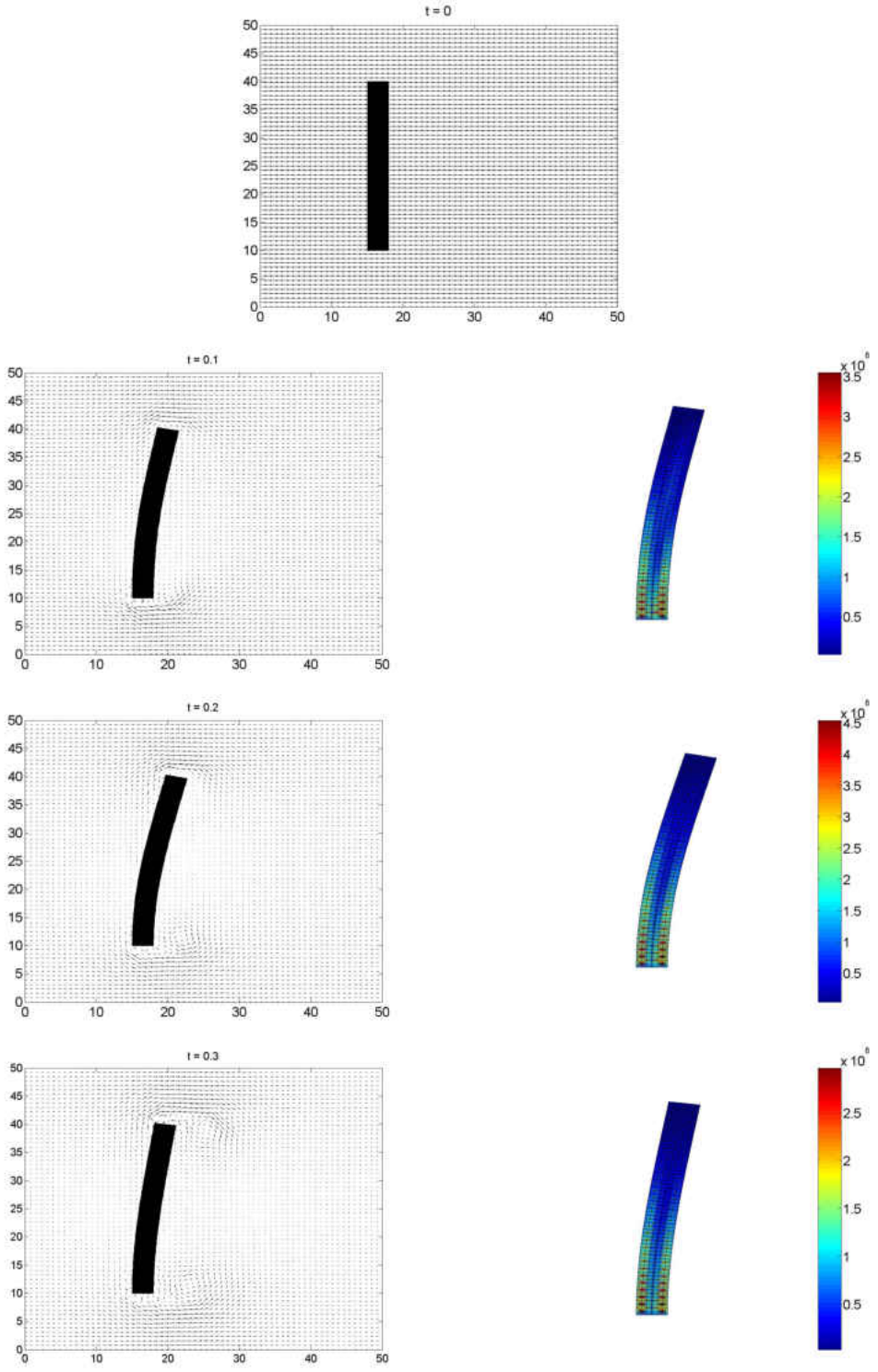

FIG. 11: The solid beam with fluid flow at different times and its stress plots.

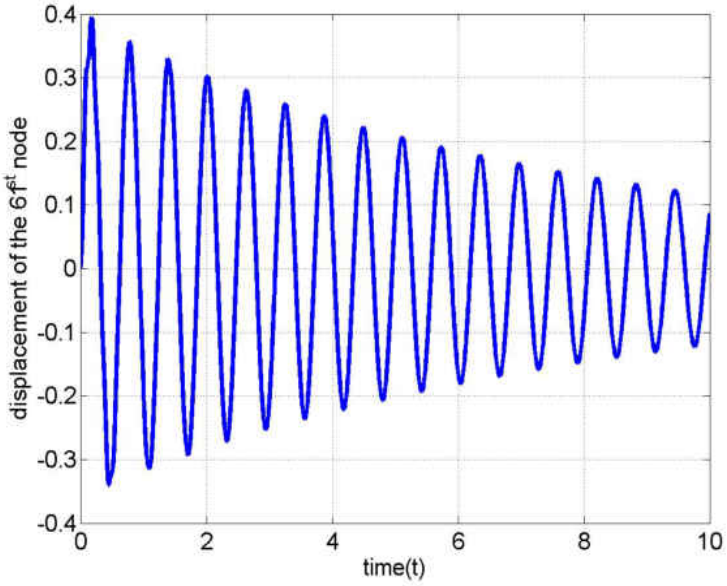

FIG. 12: Tip displacement of the solid beam in the x-direction.

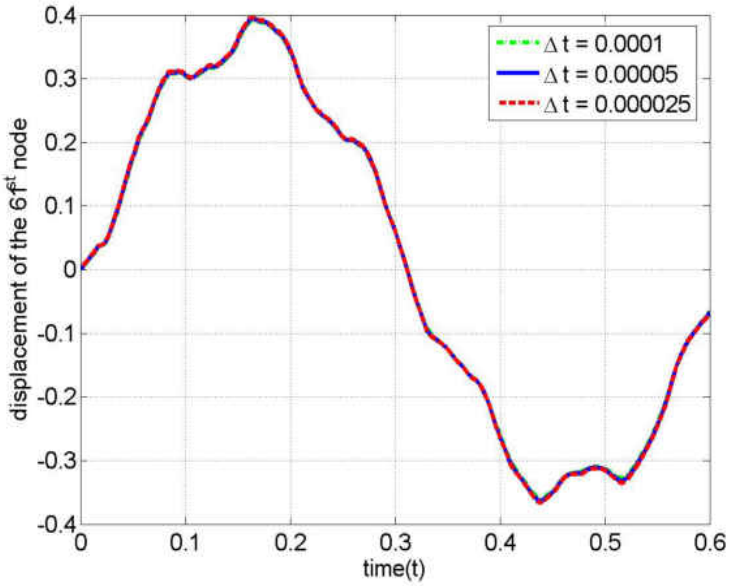

FIG. 13: Tip displacement of the solid beam with different Δt.

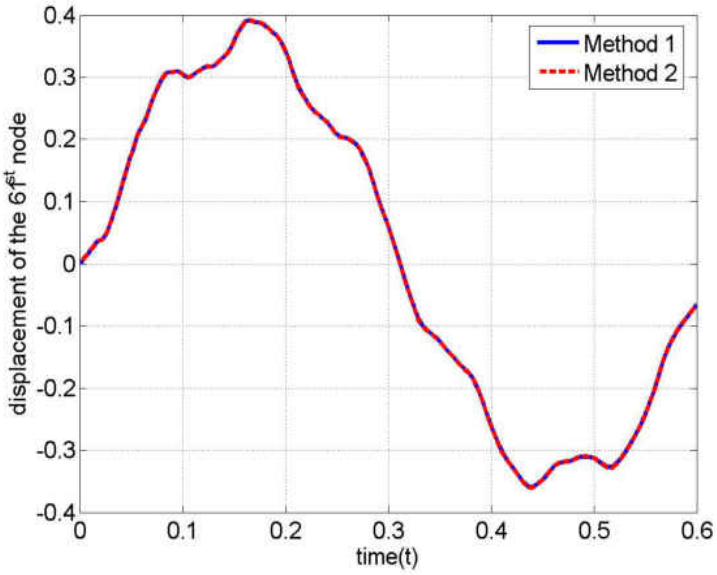

FIG. 14: Comparison of the two numerical methods for the solid beam.

2, and the algorithm described in Section 2.4.3 as Method 1. We have applied these two methods in our numerical simulation of the elastic solid beam problem, and their results match each other very well. In particular, Figure 14 shows the displacement of the 61^{st} node using the two methods with the same parameters. We observe excellent agreement between the two numerical solutions.

The close match in Figure 13 indicates convergence of the numerical results. In order to confirm this convergence property, we conduct a formal grid refinement test. We compute the L_1 and L_2 norms of the results; since the exact solution is unknown, extrapolation of the numerical solution is applied. We calculate the temporal error of the scheme at $T = 1$,

Method 1:

$$\frac{||\mathbf{u}_{\Delta t} - \mathbf{u}_{\Delta t/2}||_2}{||\mathbf{u}_{\Delta t/2} - \mathbf{u}_{\Delta t/4}||_2} = 1.85 \tag{48a}$$

$$\frac{||\mathbf{u}_{\Delta t} - \mathbf{u}_{\Delta t/2}||_1}{||\mathbf{u}_{\Delta t/2} - \mathbf{u}_{\Delta t/4}||_1} = 1.91 \tag{48b}$$

Method 2:

$$\frac{||\mathbf{u}_{\Delta t} - \mathbf{u}_{\Delta t/2}||_2}{||\mathbf{u}_{\Delta t/2} - \mathbf{u}_{\Delta t/4}||_2} = 1.86 \tag{48c}$$

$$\frac{||\mathbf{u}_{\Delta t} - \mathbf{u}_{\Delta t/2}||_1}{||\mathbf{u}_{\Delta t/2} - \mathbf{u}_{\Delta t/4}||_1} = 2.03 \tag{48d}$$

We observe a first order accuracy in the temporal direction for the whole scheme, both the structural and fluid part combined. The accuracy might be affected due to a couple of reasons: i) the sharp interface of the beam and ii) use of an explicit direct forcing approach in both methods.

2.5.4 FLOW PAST AN ELASTIC HOLLOW BEAM

In this example, we investigate the more challenging FSI problem of an immersed elastic hollow beam interacting with a viscous fluid flow. We consider the same set-up as shown in Figure 7, except that the solid beam is now replaced by a hollow beam which has an outside dimension of 30×3 (in^2) and a 28×1 (in^2) rectangular hole in the middle. The material properties of the beam remain the same as those in the previous example and the key parameters are listed in Table 2. We again consider ten mode shapes of the hollow beam (see Figure 15) to form $\boldsymbol{\psi}$ in equation (26). The corresponding eigenvalues and frequencies of each mode are listed in Table 4. The inside part of the beam is hollow and the beam is closed on all sides, so that the fluid cannot pass inside. The entire computational domain remains as $[0, 50] \times [0, 50]$. The hollow beam is discretized into 496 triangular elements with 372 nodes. We again use the 61^{st} node in reference to the top left corner of the hollow beam.

TABLE 4: Eigenvalues and frequencies of the ten modes of the hollow beam.

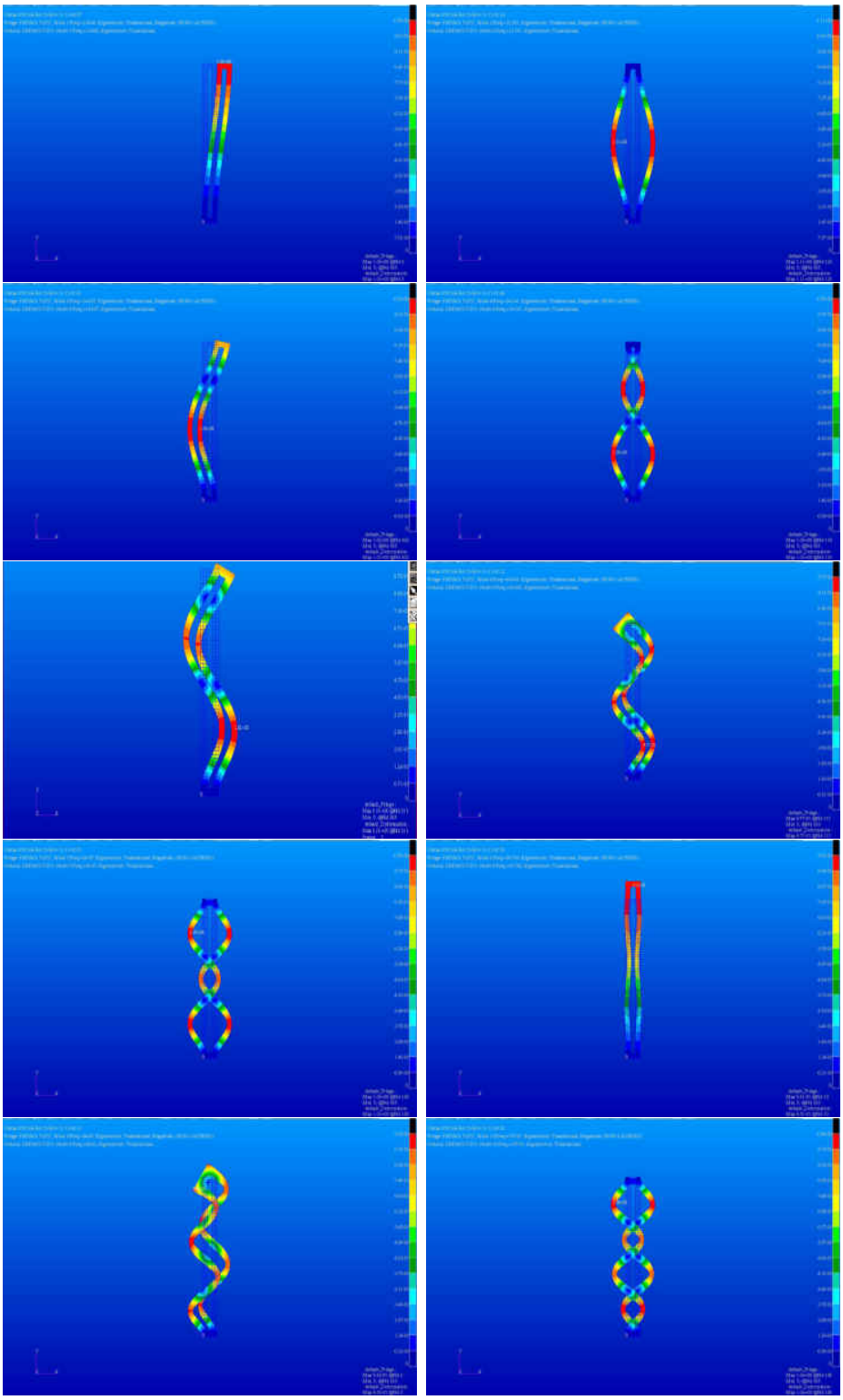

FIG. 15: Ten Mode Shapes of the hollow beam.

Mode	Eigenvalue, λ	Frequency
1	2.85E+02	2.68
2	6.17E+03	12.50
3	8.52E+03	14.69
4	4.60E+04	34.14
5	4.98E+04	35.50
6	1.66E+05	64.89
7	1.72E+05	66.07
8	2.58E+05	80.79
9	3.54E+05	94.63
10	4.57E+05	107.61

We have conducted similar simulation tasks as those in the previous example, and results show that our methods are able to accurately track the fluid - hollow beam interaction and resolve the detailed movement and deformation of the structure. In particular, Figure 16 illustrates the motion of the beam at different times. Similar to the solid case, the hollow beam exhibits a larger displacement in the direction of the flow and a smaller displacement in the opposite direction.

Figure 17 shows the movement of the structure and the fluid together, and the structural stresses at different times. We observe similar pattern of vortex formation as in Example 2.5.3.

Figure 18 shows the horizontal displacement of the 61^{st} node of the hollow beam over a long period of time, with a regular oscillation of decaying amplitude. The material and numerical parameters are the same as those in the previous example. Compared to the solid case (see Figure 12), the tip of the hollow beam exhibits larger displacements, in both positive and negative directions, as well as larger periods (or, smaller frequencies). Figure 19 compares the tip displacement of the 61^{st} node over one cycle for different Δt, where we see again the three curves closely match each other. Figure 20 shows the results of the displacement of the 61^{st} node using the two numerical approaches described before; again very good agreement is observed for these two results. The grid convergence test showed similar results as the previous example, where the overall scheme in the temporal direction is first order accurate.

Finally, we compare the displacement of the 61st node between the hollow beam and the

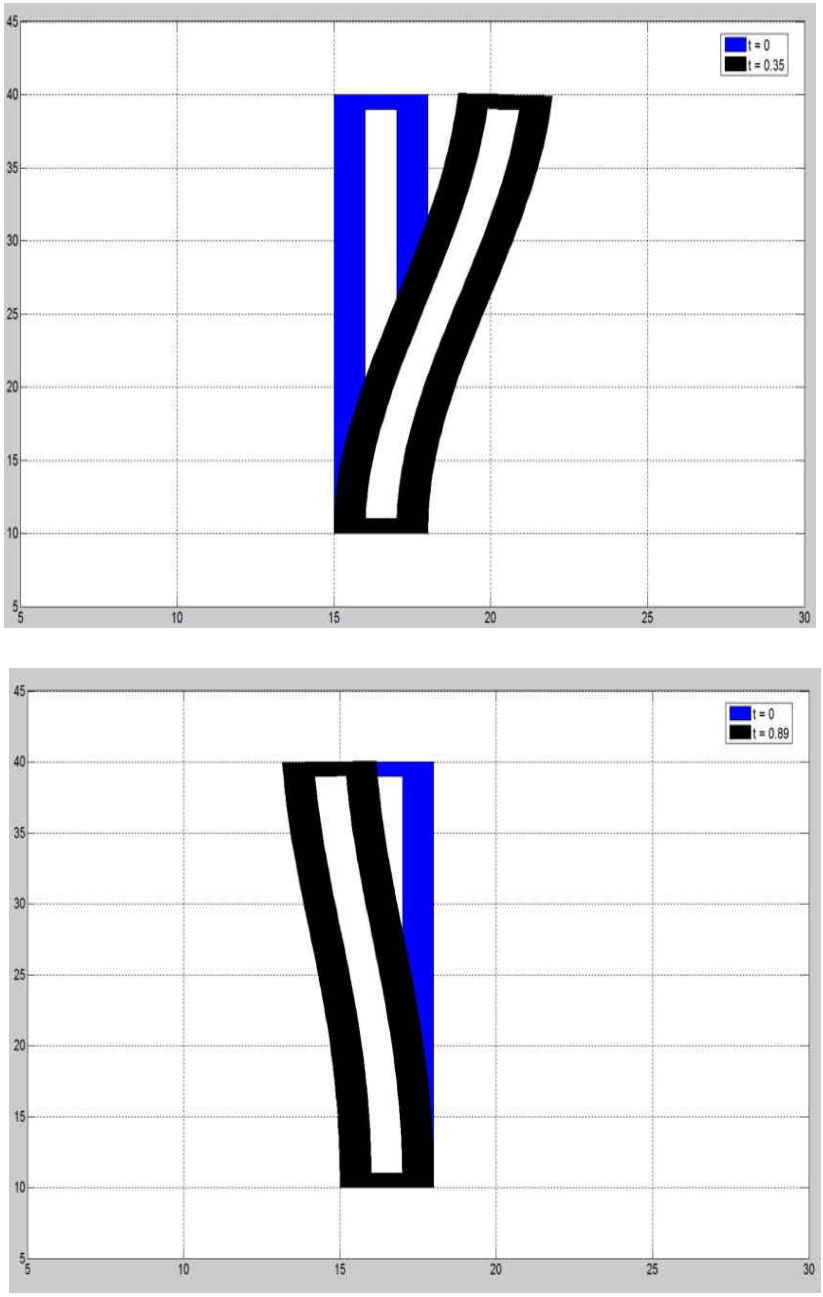

FIG. 16: Movement of the hollow beam.

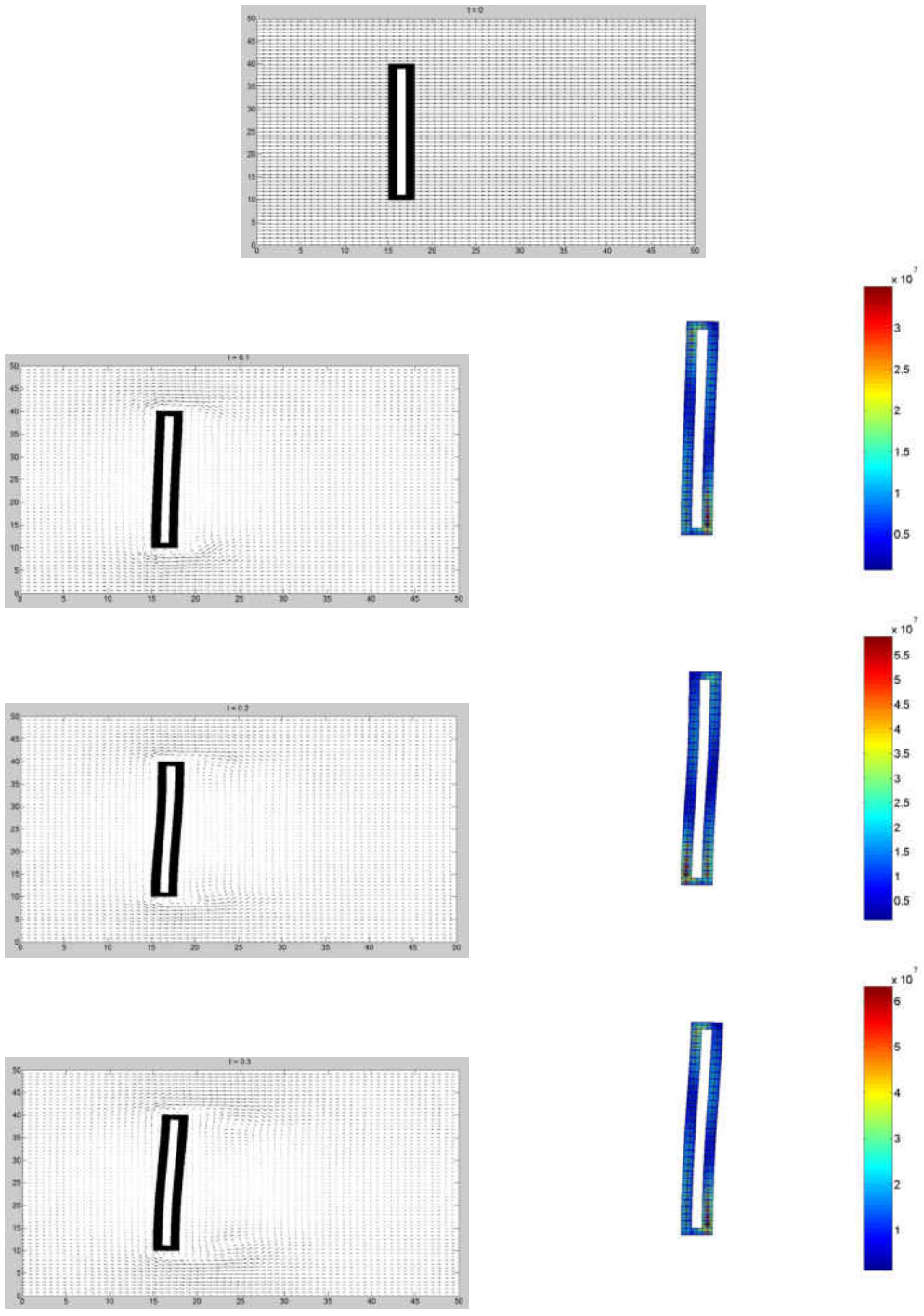

FIG. 17: The hollow beam with fluid flow at different times and its stress plots.

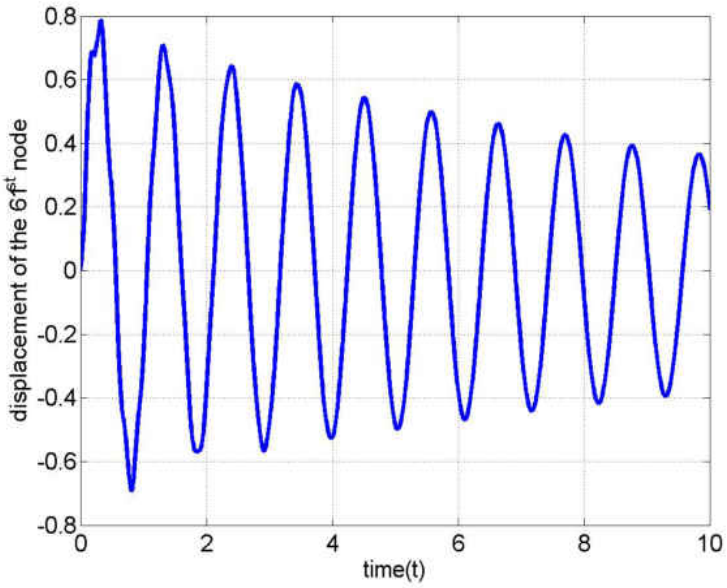

FIG. 18: Tip displacement of the hollow beam in the x-direction.

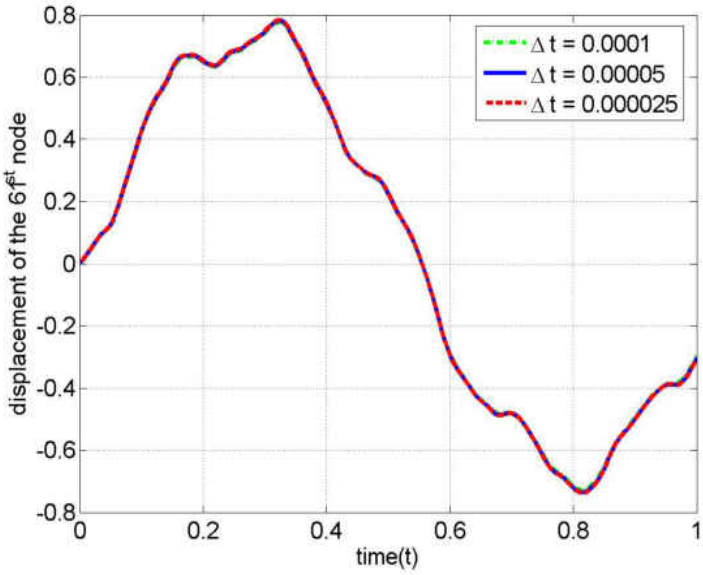

FIG. 19: Tip displacement of the hollow beam for different Δt.

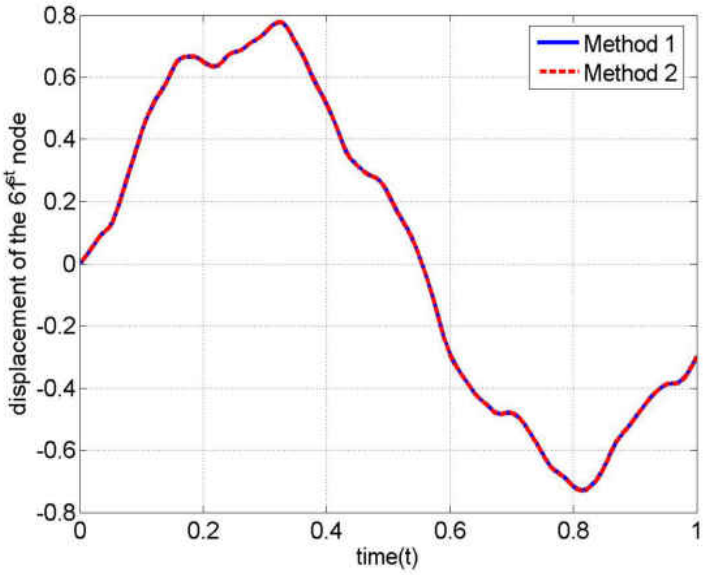

FIG. 20: Comparison of the two numerical methods for the hollow beam.

solid beam using the same material and numerical parameters, and the result is displayed in Figure 21. As is clearly shown, the solid beam vibrates faster than the hollow beam, whereas the deformation of the hollow beam is larger than that of the solid beam.

We have tested our method using two algorithms and the results are very promising. We observe a first order convergence rate in the temporal direction. Throughout our analysis we use h and Δq to be approximately of the same order to compromise the efficiency and accuracy as described in [10]. Due to the complexity of the problem and the algorithm, analysis on the numerical stability is difficult. Nevertheless, from several numerical tests, we observed that the algorithm achieves good stability property for a range of physical and numerical parameters, especially when the time step is sufficiently small. There also has been some questions raised on how to handle the flow inside the structural body. Fadlun et al. [5] suggested three possible ways for internal body treatment; none of then negatively influencing the accuracy of the flow when direct forcing method is used. The first is to apply the forcing at every point inside the body without smoothing; the second way is to let the flow develop without any constrictions; and the third is to reverse the velocity at the first point inside the body to match the desired velocity at the boundary. In our case, we adopt the second method. The external flow is not affected by the internal treatment in finite

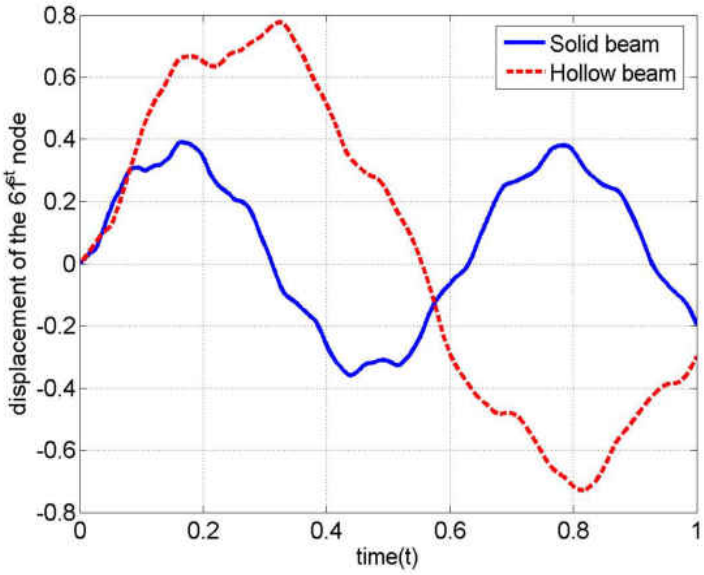

FIG. 21: Comparison of the tip displacement for the solid and hollow beams with the same material and numerical parameters.

differences methods due to the smaller width of stencils in the matrices [33]. Conservation of the mass at the immersed boundary is also satisfied by such a treatment. And, we have shown that numerical simulations of flow past an elastic body results in a first order temporal accuracy using our method. The method proposed is very attractive since it is relatively simple to implement, and is computationally inexpensive.

2.6 DISCUSSION

We have presented a new framework to compute fluid-structure interactions by integrating the immersed boundary techniques and the direct-forcing method. Through a partitioned approach, our algorithms allow well-developed disciplinary methods and codes to solve the respective fluid and structural equations, whose solutions are connected at the fluid-structure interface by communicating forces and velocities. Unlike most of the existing FSI methods which are restricted to relatively simple structural settings, our framework makes it possible to explore highly challenging FSI problems that involve complex fluid motion and sophisticated structural shapes and configurations. We have demonstrated our methods through careful numerical simulations that involve viscous fluid flow interacting with rigid, elastic

solid, and elastic thin-walled, structures. Results clearly show that our numerical approach is capable of handling various structural types and resolving the detailed movement and deformation of the structures when interacting with fluid flow. Our work generalizes the original immersed boundary method to accommodate structures that occupy finite volumes and that are represented by realistic material constitutive laws. Meanwhile, our approach extends the conventional direct-forcing technique to the simulation of FSI problems involving elastic structures. To our knowledge, these represent a first-of-its-kind advance in FSI computational study.

The advantages of the partitioned approach lie in its flexibility and portability in FSI simulation. Each of the fluid and structure systems can be handled independently with different solvers and meshes, and details of the solution procedure for one system can be easily modified without affecting the other party. These features make the foundation to employ disciplinary solvers that have been well developed, rigorously validated, and constantly updated, in the FSI computation for attacking the potentially most sophisticated problems in the field. The typical challenge in the implementation of the partitioned approach, however, is the coupling of the fluid and structural solvers for an accurate representation of the interaction at the fluid-structure interface. In this work, we have applied numerical techniques originated from the immersed boundary and the direct-forcing methods to link the fluid and structural solutions for an accurate, stable and efficient FSI computational procedure.

FSI problems are inherently interdisciplinary, and this chapter strongly emphasizes interdisciplinary collaboration in advancing the study in this fast-growing scientific field. Our work provides a platform that can naturally assemble researchers in the fluid and structure dynamics fields to collaborate on FSI simulation and analysis. Future development of this work would involve exploration of more accurate and efficient techniques for coupling the fluid and structural solutions, and extension of the methodology from 2D space to 3D space.

CHAPTER 3

MODELING AND SIMULATION OF TUMOR VIROTHERAPY AND STABILITY ANALYSIS

3.1 BACKGROUND

Cancer is characterized by abnormal cell growth without control. Cancer cells typically grow and divide rapidly, with a high potential of invading and spreading to other parts of the body. The causes for cancer are complicated and could involve biological, environmental, and genetical factors, as well as related to the age, life style, and health conditions of individuals. Cancer has long been a leading cause of death in developed countries. The World Health Organization (WHO) estimates that in 2012, about 14 million new cases of cancer occurred, which led to about 8.2 million deaths [66]. Meanwhile, there are tremendous financial costs in connection with cancer, estimated at 1.16 trillion US dollars per year as of 2010 [67].

There have been a number of options available for cancer management. Surgery, the primary method of treatment for most isolated cancers, aims to remove the entire tumor from the body. However, complete surgical excision is often difficult, with success mainly for small and localized tumors. The procedure may be impossible for tumors that either have metastasized to other sites of the body or possess metastatic potential. Chemotherapy, on the other hand, is the treatment of cancer with one or more drugs that can kill the tumor cells. Such anti-cancer drugs typically target cells that divide rapidly, an essential property of tumor cells, though healthy cells with a high replacement rate can be potentially harmed. The effectiveness of chemotherapy thus depends on the type and stage of the cancer, and the toxicity introduced to other tissues in the body. Radiation therapy, another common approach for treating cancers, utilizes ionizing radiation in an attempt to damage the genetic materials of tumor cells and prevent these cells from continuing growth and division. The radiation (inevitably) injures normal cells and tissues, as a side effect, and it is often used in combination with surgery and/or chemotherapy. Other tumor treatment options include,

but not limited to, hormonal therapy, immunotherapy, angiogenesis inhibitors, and palliative care.

A relatively new, yet propitious, strategy in treating cancer is the virotherapy [52, 58], which makes use of genetically engineered oncolytic viruses that are specific to tumor cells. Once entering the tumor (typically through intralesional injection), the oncolytic viruses infect cancer cells and replicate inside them, while leaving normal cells and tissues unharmed. Through the lysis of the infected cells, the viruses spread within the tumor and go on to infect other cancer cells. Distinct advantages of the virotherapy includes: (1) viruses infect and replicate in a highly tumor-selective way, and thus are relatively non-pathogenic to healthy tissues; (2) viruses can utilize multiple genetic means to attack tumor cells and cause cell lysis; (3) viruses can be genetically manipulated to include additional features for improving safety and efficacy [38]. The therapy has shown promising results in preclinical tests and clinical trials for a number of tumor types [46–48, 55].

At present, despite producing hundreds of infectious viruses per one infected tumor cell, most virus species are unable to eradicate the tumor [40]. It has been known that the immune responses to the viruses injected play a critical role in the overall efficacy of the tumor viral therapy. Importantly, however, the tumor cell oncolysis process induces immune responses for both the viruses and the tumor: the innate immunity tends to limit virus replication and/or spread, whereas the adaptive immunity works in a manner against the tumor [38, 49, 53]. Thus, the interactions of oncolytic viruses and the immune systems may contribute to therapeutic outcomes in two opposite fashions: negatively through the anti-virus immune response, and positively through the anti-tumor immune response.

Despite the promising future of the virotherapy, our knowledge in the field is still limited and several challenges remain in current clinical study [49, 52, 58]. For example, what is the relative contribution of direct viral oncolysis and indirect immune suppression to the overall therapeutic efficacy? How to effectively combine the oncolysis and the virus mediated immunity, and how to strategically manipulate the balance between anti-virus and anti-tumor immune responses? Meanwhile, genetically reprogramming the viruses so as to improve tumor cell oncolysis, while provoking robust and long-lasting anti-tumor immunity, will be particularly important for the success of the therapy [64]. In addition, the mechanisms underlying tumor sensitivity and resistance under the therapy are unclear at present and demand further investigation.

Mathematical modeling, analysis and simulation, as a power means of theoretical research, have long provided useful insight into the complications of tumor growth and the effectiveness of various tumor treatments. Such findings can offer potentially critical guidelines in the design, validation, and improvement of cancer management strategies. Recent reviews on mathematical tumor modeling can be found in [36, 39, 50, 63], and representative work in the field can be found at the references therein.

In particular, a number of mathematical studies have been devoted to the virotherapy and its impact on tumor growth. Wodarz [62] and Novozilov et al. [54] proposed ordinary differential equation (ODE)-based models, with two compartments representing the infected and uninfected tumor cell populations. Each cell population is assumed to grow in a logistic fashion, and there is no separate equation for viral dynamics. Karev et al. [45] extended these models to a more general differential equation modeling framework, with an emphasis on tumor cell heterogeneity. Tian [60] analyzed the interaction between tumor cells and viruses, also using an ODE model, and focused on the bifurcation study of the virus replicability that is measured by the burst size. Wu et al. [65] formulated a model using a system of partial differential equations (PDEs) and compared the evolution of a tumor under different initial conditions that resulted from three virus-injection strategies. Friedman et al. [41] proposed a PDE-based model to investigate tumor virotherapy with host immunity. Their model, however, only considered the innate immune response and did not include the adaptive immunity.

One of the goals of this chapter is to establish a new mathematical and computational modeling framework for tumor virotherapy that can describe the complex interaction among tumor cells, oncolytic viruses, and immune systems, and that can incorporate both innate and adaptive immune responses. To that end, we construct a reaction-convection-diffusion system, with the motion of cells represented by a convection process and that of viruses represented by a diffusion process. The cell-virus interaction follows an 'epidemic' route: the viruses work as the pathogen that attack and infect the normal (or, susceptible) tumor cells. The infected tumor cells stimulate immune responses, both for the anti-virus innate immunity and the anti-tumor adaptive immunity. Meanwhile, new viruses are generated and spread through the lysis of the infected tumor cells and continue infecting other tumor cells. Most importantly, our model contains a moving boundary that explicitly describes the change of the tumor size with time.

The strongly nonlinear PDE system and the presence of an unknown moving boundary

make our model analytically intractable. Nevertheless, using carefully designed computational methods that ensure high accuracy and robust numerical stability, we are able to conduct an extensive numerical study. In particular, we have investigated the growth pattern of the tumor, which is a direct indication for the efficacy of the tumor therapy, under a wide range of settings that include variations of several key parameters and comparisons of tumor growth with and without delay in the adaptive immunity, as well as different types of viral dose administrations.

In the second half of the chapter, we look at stability analysis based on a reduced ordinary differential equations. We analyze the stability of boundary equilibrium points using the linear stability analysis, and the endemic equilibrium are analyzed using Newton Raphson iterative method. Qualitative phase portraits are shown for a given set of parameters that display characteristics of the stability of the tumor. These analysis provide insightful results for controlling the growth of the tumor.

3.2 MATHEMATICAL FORMULATION

We first present our mathematical model that describes the interaction among tumor cells, oncolytic viruses, and immune responses, and the growth of the tumor that results from such interaction.

We consider a radially symmetric tumor. Let t denote the time and ρ denote the spatial distance measured from the center of the tumor. Let also $R(t)$ be the moving boundary of the tumor (that is changing with time). In addition, we define

$X(\rho, t)$ = number density of tumor cells not yet infected by the viruses;
$Y(\rho, t)$= number density of tumor cells already infected by the viruses;
$Z_1(\rho, t)$= number density of innate immune cells;
$Z_2(\rho, t)$= number density of adaptive immune cells;
$V(\rho, t)$= number density of viruses;
$N(\rho, t)$= number density of dead tumor cells;
$U(\rho, t)$= radial velocity of the tumor cells.

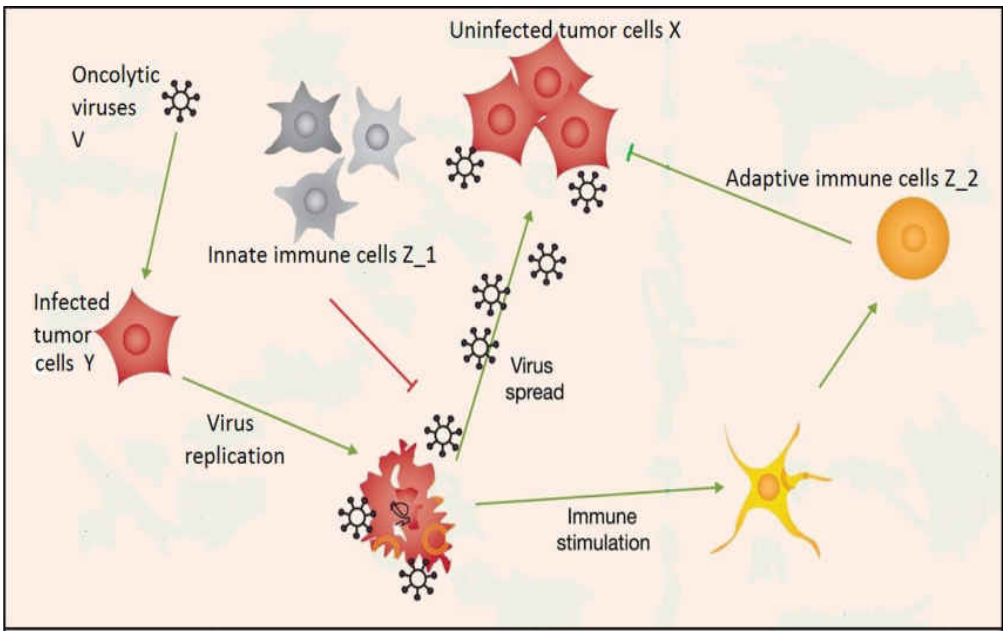

FIG. 22: The interaction among oncolytic viruses, tumor cells, and immune responses (picture modified from Figure 1 in Ref. [38]).

We assume that all the above mentioned cells have the same size and are uniformly distributed in the tumor. We also assume that the total cell density is a constant; i.e.,

$$X + Y + Z_1 + Z_2 + N = \theta = \text{Const.} \tag{49}$$

where $\theta \approx 10^6$ cells/mm^3 [41]. For convenience of discussion, we will normalize the total cell density such that $\theta = 1$. Consequently, X, Y, Z_1, Z_2 and N become the percentages (or volume fractions) out of the constant total for their respective cell densities.

The uninfected tumor cells grow at a proliferation rate λ. Meanwhile, they are infected by the viruses (through cell-virus contact) at a rate β and subsequently enter the class of infected tumor cells. In addition, the anti-tumor adaptive immune response kills these tumor cells (through cell-cell contact) at a rate k_2 and these subsequently enter the class of dead tumor cells. In contrast, the innate immune response works against the virotherapy and kills the infected tumor cells at a rate k_1. Additionally, the infected tumor cells has a lysis rate of δ. The innate and adaptive immune cells are stimulated through their interaction with the infected tumor cells at rates of s_1 and s_2, respectively, and are cleared at rates of c_1 and c_2.

The dead cells are removed at a rate μ. New viruses are produced through the lysis of the infected tumor cells with a burst size b. Moreover, the viruses are cleared at a rate γ, as well as killed by the innate immune response (through cell-virus contact) at a rate k_0. Finally, we assume that all cells undergo a convection process along the radial direction of the tumor with a convection velocity U. Viruses, on the other hand, are much smaller than cells in size (typically, the diameter of a cell is 100 times larger than that of a virus) and their motion tends to be random and non-unidirectional. Thus we assume that viruses follow a diffusion process with a diffusion rate D. A picture illustrating the virus-tumor-immune interaction is shown in Figure 22.

These assumptions yield the following differential equations

$$\frac{\partial X}{\partial t} + \frac{1}{\rho^2}\frac{\partial}{\partial \rho}(\rho^2 U X) = \lambda X - \beta X V - k_2 X Z_2 \tag{50a}$$

$$\frac{\partial Y}{\partial t} + \frac{1}{\rho^2}\frac{\partial}{\partial \rho}(\rho^2 U Y) = \beta X V - k_1 Y Z_1 - \delta Y \tag{50b}$$

$$\frac{\partial Z_1}{\partial t} + \frac{1}{\rho^2}\frac{\partial}{\partial \rho}(\rho^2 U Z_1) = s_1 Y Z_1 - c_1 Z_1 \tag{50c}$$

$$\frac{\partial Z_2}{\partial t} + \frac{1}{\rho^2}\frac{\partial}{\partial \rho}(\rho^2 U Z_2) = s_2 Y Z_2 - c_2 Z_2 \tag{50d}$$

$$\frac{\partial N}{\partial t} + \frac{1}{\rho^2}\frac{\partial}{\partial \rho}(\rho^2 U N) = k_1 Y Z_1 + k_2 X Z_2 + \delta Y - \mu N \tag{50e}$$

$$(\rho^2 \frac{\partial V}{\partial \rho}) = b\delta Y - k_0 Z_1 V - \gamma V \tag{50f}$$

$$\frac{1}{\rho^2}\frac{\partial}{\partial \rho}(\rho^2 U) = \lambda X + s_1 Y Z_1 + s_2 Y Z_2 - c_1 Z_1 - c_2 Z_2 - \mu N \tag{50g}$$

Here the last equation is obtained by adding up the first five equations and using the fact that the total cell density is a constant. These equations hold on the spherical domain $0 \le \rho \le R(t)$ for $t \ge 0$. Meanwhile, the free boundary, $R(t)$, satisfies the kinematic condition,

$$\frac{dR}{dt} = U(R(t), t). \tag{51}$$

Boundary and initial conditions are necessary to complete the model. In particular, we need to prescribe the boundary conditions for V, which is governed by a parabolic equation,

and U, which satisfies an ordinary differential equation. We consider the ideal situation that all the free viruses remain in the tumor, and impose a homogeneous Neumann condition for V at the tumor boundary:

$$\frac{\partial V}{\partial \rho}(R(t), t) = 0. \tag{52a}$$

At the tumor center, the spherical symmetry implies that

$$U(0, t) = 0, \tag{52b}$$

$$\frac{\partial V}{\partial \rho}(0, t) = 0. \tag{52c}$$

3.3 NUMERICAL METHODS

A difficulty in the design of numerical algorithms for the model (50) is the presence of a moving boundary, $R(t)$, which describes the growth of the tumor with time and which has to be determined as part of the solution. To partially overcome this challenge, we choose to map the original domain with the moving boundary into a fixed domain, by introducing a new co-ordinate:

$$r = \frac{\rho}{R(t)}\,. \tag{53}$$

Obviously, equation (53) transforms the original domain, $0 \leq \rho \leq R(t)$, into a regular interval, $0 \leq r \leq 1$. Based on such a mapping, we are able to develop accurate and robust numerical methods.

Equation (49) enables us to drop one variable, N. Using the change of co-ordinates, the

original equations in (50) can be written as

$$\frac{\partial X}{\partial t} + \frac{U - rR'}{R}\frac{\partial X}{\partial r} = F_1, \tag{54a}$$

$$\frac{\partial Y}{\partial t} + \frac{U - rR'}{R}\frac{\partial Y}{\partial r} = F_2, \tag{54b}$$

$$\frac{\partial Z_1}{\partial t} + \frac{U - rR'}{R}\frac{\partial Z_1}{\partial r} = F_{3a}, \tag{54c}$$

$$\frac{\partial Z_2}{\partial t} + \frac{U - rR'}{R}\frac{\partial Z_2}{\partial r} = F_{3b}, \tag{54d}$$

$$\frac{\partial V}{\partial t} - \Big(\frac{rR'}{R} + \frac{2D}{R^2 r}\Big)\frac{\partial V}{\partial r} - \frac{D}{R^2}\frac{\partial^2 V}{\partial r^2} = F_4, \tag{54e}$$

$$\frac{1}{Rr^2}\frac{\partial}{\partial \rho}(r^2 U) = F_5, \tag{54f}$$

for $0 \le r \le 1$ and $t > 0$, where $R' = \frac{dR}{dt}$. The terms on the right-hand sides are:

$$\begin{aligned}
F_1 &= \lambda X - \beta XV - k_2 X Z_2 - FX, \\
F_2 &= \beta XV - k_1 Y Z_1 - \delta Y - FY, \\
F_{3a} &= s_1 Y Z_1 - c_1 Z_1 - F Z_1, \\
F_{3b} &= s_2 Y Z_2 - c_2 Z_2 - F Z_2, \\
F_4 &= b\delta Y - k_0 Z_1 V - \gamma V, \\
F_5 &= F,
\end{aligned}$$

where

$$F = \lambda X + s_1 Y Z_1 + s_2 Y Z_2 - c_1 Z_1 - c_2 Z_2 - \mu(1 - X - Y - Z_1 - Z_2).$$

The kinematic condition in equation (51) and boundary conditions in equation (52) become

$$\frac{dR}{dt}(t) = U(1,t), \tag{55}$$

$$\frac{\partial V}{\partial r}(1,t) = 0, \tag{56}$$

$$U(0,t) = 0, \tag{57}$$

$$\frac{\partial V}{\partial r}(0,t) = 0. \tag{58}$$

The initial conditions are given below. In particular, the initial values for R and V are taken from [41], based on lab experiments conducted on rats with brain tumors. When the virotherapy starts, the oncolytic viruses are injected into the center of the tumor, which is measured at 2 mm at that time. Meanwhile, a Gaussian distribution centered at 0 is used to represent the initial profile of the viruses inside the tumor. Additionally, we note that all the cell densities have been normalized so that the total is $\theta = 1$ cell/mm^3.

$$R(0) = 2\,\text{mm}\,, \tag{59}$$

$$V(r,0) = \alpha e^{-\frac{4r^2}{a^2}}, \quad \text{where} \quad \alpha \int_0^1 \mathrm{r}^2 \mathrm{e}^{-\frac{4\mathrm{r}^2}{\mathrm{a}^2}}\,\mathrm{dr} = 0.45, \tag{60}$$

$$X(r,0) = 0.8\,\text{cell/mm}^3, \quad \mathrm{Y}(\mathrm{r},0) = 0.1\,\text{cell/mm}^3, \tag{61}$$

$$Z_1(r,0) = 0.05\,\text{cell/mm}^3, \quad \mathrm{Z_2}(\mathrm{r},0) = 0.05\,\text{cell/mm}^3. \tag{62}$$

The numerical simulation of equation (54) is essentially a time-marching problem. We denote the numerical solution at the n^{th} time step by

$$(R^n, X^n, Y^n, Z_1^n, Z_2^n, U^n, V^n).$$

We use the second-order Adams-Bashforth method to advance R in time. Applying it to equation (55) yields

$$R^{n+1} = R^n + \frac{\Delta t}{2}(3U^n - U^{n-1}). \tag{63}$$

The hyperbolic type equations, for example equation (54a), is solved by a leapfrog scheme:

$$\frac{X_j^{n+1} - X_j^{n-1}}{2\Delta t} + A_j^n \frac{X_{j+1}^n - X_{j-1}^n}{2\Delta r} = (F_1)_j^n, \tag{64}$$

where

$$A = \frac{U - rR'}{R}\,, \tag{65}$$

and the subscript j refers to the j^{th} spatial grid point in the radial direction. Meanwhile, we supplement the leapfrog method with a a simple average in time: $X_j^n = \frac{1}{2}(X_j^{n+1} + X_j^{n-1})$, implemented in our code for every 10 steps. This additional time-average procedure is introduced to overcome potential mesh drifting instability [57] when applying the leapfrog method to nonlinear equations, yet retaining its second-order accuracy [61]. In addition, Y,

Z_1, and Z_2 are updated in a similar way.

Once we have X^{n+1}, Y^{n+1}, Z_1^{n+1} and Z_2^{n+1} calculated, we compute U^{n+1} using the Trapezoidal Rule for equation (54f):

$$r_{j+1}^2 U_{j+1}^{n+1} - r_j^2 U_j^{n+1} = \frac{R^{n+1}}{2}\Delta r\Big(r_{j+1}^2 (F_5)_{j+1}^{n+1} + r_j^2 (F_5)_j^{n+1}\Big)\,. \tag{66}$$

Finally, we solve the parabolic equation (54e). For convenience, we write the equation in the following form:

$$\frac{\partial V}{\partial t} + A_1 \frac{\partial V}{\partial r} + A_2 \frac{\partial^2 V}{\partial r^2} = F_4, \tag{67}$$

with

$$A_1 = -\Big(\frac{rR'}{R} + \frac{2D}{R^2 r}\Big) \quad , \quad A_2 = -\frac{D}{R^2}\,. \tag{68}$$

Since F_4 is a linear function of V^{n+1}, the above equation is a linear parabolic equation at time step $n+1$. We use the second-order Backward Difference Formula (BDF) in time and central differences in space to approximate equation (67):

$$\frac{3V_j^{n+1} - 4V_j^n + V_j^{n-1}}{2\Delta t} + (A_1)_j^{n+1}\frac{V_{j+1}^{n+1} - V_{j-1}^{n+1}}{2\Delta r} + (A_2)_j^{n+1}\frac{V_{j+1}^{n+1} - 2V_j^{n+1} + V_{j-1}^{n+1}}{(\Delta r)^2} = (F_4)_j^{n+1}\,. \tag{69}$$

The discretized equation can be written in a tridiagonal algebraic form as follows,

$$b_j V_{j-1}^{n+1} + d_j V_j^{n+1} + a_j V_{j+1}^{n+1} = S_j, \quad j = 1, 2, ...J, \tag{70}$$

where

$$\begin{aligned}
b_j &= \frac{2\Delta t}{\Delta r^2}(A_2)_j^{n+1} - \frac{\Delta t}{\Delta r}(A_1)_j^{n+1},\\
d_j &= 3 - \frac{4\Delta t}{\Delta r^2}(A_2)_j^{n+1} + 2k_0\Delta t (Z_1)_j^{n+1} + 2\gamma\Delta t,\\
a_j &= \frac{2\Delta t}{\Delta r^2}(A_2)_j^{n+1} + \frac{\Delta t}{\Delta r}(A_1)_j^{n+1},
\end{aligned}$$

and

$$S_j = 4V_j^n - V_j^{n-1} + 2b\delta\Delta t Y_j^{n+1}.$$

Such a system can be solved efficiently [43]. We implement the simplified version of Gaussian Elimination Method for a tridiagonal system, called the Thomas algorithm to solve the above system of linear equations. Once solved, a full cycle of the time marching is completed, and the procedure repeats at the next cycle.

The methods presented here achieve second-order accuracy in both time and space, and possess strong numerical stability, which allows us to conduct a careful numerical study on the complex interaction among the tumor, the viruses, and the immune systems involved in the tumor virotherapy.

3.4 RESULTS

Mathematical analysis of the system (50) is challenging since it is strongly nonlinear with mixed types of PDEs. Meanwhile, the presence of an unknown moving boundary adds more difficulty. Instead, we have chosen to utilize numerical simulation in order to gain useful biological insight using the algorithms described in Section 3.3. Essentially, we map the original spatial domain with a moving boundary, $0 \leq \rho \leq R(t)$, into a fixed domain, $0 \leq r \leq 1$, through a time-dependent coordinate transformation, which enables us to design and implement numerical methods of second-order accuracy and robust stability.

Using such algorithms, we have conducted extensive numerical simulation to our model. We then present the simulation results throughout this section with detailed explanations. The base values of the model parameters used in our simulation are listed in Table 5. Most of these parameter values are taken from [41, 61] but with necessary adjustments to be consistent with our normalized variables.

We use the same initial conditions as given in [41], which are based on lab experiments conducted on rats with brain tumors. They are also listed in the Numerical Method section of this chapter. The tumor size is initialized as $R(0) = 2$ mm, at which time the oncolytic viruses are injected into the center of the tumor and the process of virotherapy starts. A Gaussian distribution is used to represent the initial profile of the viruses inside the tumor.

Throughout the numerical simulation, we focus our attention on the change of the tumor size with respect to time. The tumor size is a crucial factor in the measurement of the

TABLE 5: Parameters and baseline values for tumor virotherapy

Symbol	Description	Value
λ	Proliferation rate of tumor cells	2.0 h^{-1}
β	Viral infection rate	3.5 mm^3 h^{-1} $virus^{-1}$
k_1	Innate immune killing rate	2.0 mm^3 h^{-1} $cell^{-1}$
k_2	Adaptive immune killing rate	2.0 mm^3 h^{-1} $cell^{-1}$
s_1	Innate immunity stimulation rate	56.0 mm^3 h^{-1} $cell^{-1}$
s_2	Adaptive immunity stimulation rate	56.0 mm^3 h^{-1} $cell^{-1}$
c_1	Clearance rate of innate immune cells	2.0 h^{-1}
c_2	Clearance rate of adaptive immune cells	2.0 h^{-1}
D	Diffusion coefficient of viruses	3.6 mm^2 h^{-1}
δ	Infected cell lysis rate	5.6 h^{-1}
k_0	Take-up rate of viruses by innate immunity	1.0 mm^3 h^{-1} $cell^{-1}$
γ	Clearance rate of viruses	2.5 h^{-1}
μ	Removal rate of dead cells	2.1 h^{-1}
b	Viral burst size	1.0 virus $cell^{-1}$

degree of cancer and the efficacy of a therapy; continual growth of a tumor is typically an indication of the malignancy (and progressive worsening) of the tumor. (As reported in [42] for the experiments on rats, when the brain tumor grows to a size with 6 mm in radius, it usually kills a rat.) Thus, in our numerical study, we will especially examine the time evolution of the tumor boundary $R(t)$, which directly measures the size of the tumor, to help us understand the effects of the virotherapy.

3.4.1 BASELINE SOLUTIONS

Figure 23 displays the change of $R(t)$ with respect to time under the virotherapy, using parameter values described in Table 5, referred to as the base values. We observe that the tumor grows almost linearly for the first 50 hours, due to the fact that the viruses are injected into the center of the tumor and it takes time for the viruses to spread, to interact with the tumor cells, and to stimulate immune response throughout the tumor. Thus the efficacy of the therapy is not fully reflected in this initial period. During the next 150 hours or so, however, the tumor completely stops growing, and even decays slightly, indicating that the virotherapy is taking effect. Finally, the tumor starts to re-grow after the effective period of the treatment. Despite the re-growth of the tumor, the contribution of the therapy is clear:

it has suppressed the tumor growth for a significant period of time (around 150 hours).

Figure 24 shows the profiles of the densities for the uninfected tumor cells (X), the innate immune cells (Z_1) and the adaptive immune cells (Z_2) at several times during this process, under the same setting as in Figure 23. The uninfected tumor cells are initially set at 80% with a uniform distribution on the transformed spatial domain, $0 \leq r \leq 1$ (see Figure 24a). At $t = 100$ hours, their density has been reduced to a much lower level, ranging between $9\% - 20\%$, due to the interaction with the oncolytic viruses. The reduction is most significant for the region near the center of the domain ($r = 0$), where the viruses have the highest concentration. We also note that the time falls within the period of non-growth of the tumor in Figure 23. When $t = 200$ hours, however, X has increased to a level of $45\% - 65\%$ (again the lowest density occurs near the center); correspondingly, we see from Figure 23 that the tumor has started to re-grow. As time goes on, X continues increasing and, at $t = 360$ hours, it is already close to 100%. On the other hand, the densities of the immune cells, Z_1 and Z_2 , show an opposite trend (see Figure 24b and Figure 24c). They are initially set as 5% uniformly for each, and then increase owing to the stimulation of the infected tumor cells. At $t = 100$ hours, Z_1 reaches a level ranging between $30\% - 40\%$, with the highest density occurring near the center of the domain, whereas Z_2 ranges between $12\% - 20\%$, with the highest density near the boundary of the domain. Afterwards the densities of the immune cells start decreasing and, at $t = 360$ hours, both Z_1 and Z_2 are almost 0%. These are consistent with the pattern of the tumor growth exhibited in Figure 23.

3.4.2 EFFECTS OF PARAMETER VARIATION

Naturally, we hope to improve the baseline result presented in Figures 23 and 24. To that end, it is necessary that we understand, and quantify, the contribution of the various parameters that appear in the model (50). Hence, we proceed to analyze the effects of the variation of a few key parameters and conditions on the growth of the tumor.

Figure 25 displays the results of varying the two immune killing rates: k_1 for the innate immunity and k_2 for the adaptive immunity. As we know, the innate immune response works in an anti-viral manner, whereas the adaptive immune response tends to be anti-tumor. Figure 25 shows that when fixing $k_2 = 2$ at its base value and increasing k_1 from its base value to 20, the tumor would grow faster than its baseline scenario after an initial

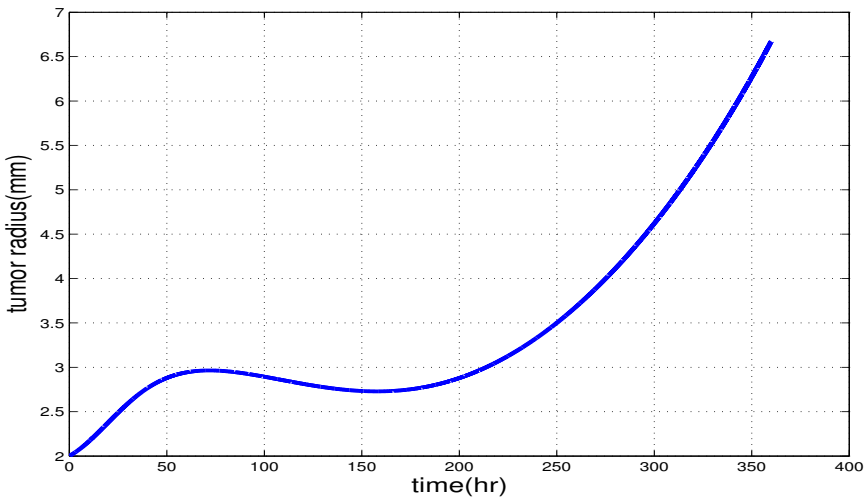

FIG. 23: Change of tumor radius with time.

transient period. In contrast, when fixing $k_1 = 2$ at the base value and increasing k_2 to 20, the tumor would grow slower, and eventually decay in size, demonstrating a higher level of anti-tumor effect with the increased adaptive immunity. In addition, when k_1 and k_2 are both decreased to a small value, 0.2, the tumor would grow significantly faster; when both parameters are increased to a large value, 200, the tumor would decay from the very beginning, implying that immune responses are necessary for the success of the virotherapy. To gain more insight into the effects of the two immune killing rates on tumor growth, we have created a bifurcation diagram in the $(k_1,\ k_2)$ plane, shown in Figure 26. The red curve in Figure 26 displays the boundary that separates two parameter regions; i.e., the tumor grows in one region, and decays in the other.

Figure 27 shows the parameter variation effect of the two immune stimulation rate, s_1 for innate and s_2 for adaptive immunity. From the baseline value of 56, increasing s_1 would result in the tumor growing faster. If s_2 is increased, i.e. if the adaptive immunity is stimulated at a faster rate, then the tumor decays. However, the decay is not long lasting and the tumor quickly shows sign of re-growth. Nevertheless, it is important to note that higher values of s_2 and lower values of s_1 aides in the virotherapy process.

Figure 28 shows the effect of parameter variation on the clearance rate of immune cells, c_1 for innate and c_2 for adaptive immunity. As c_1 and c_2 are increased from the base value of 2, higher values of c_1 shows positive response in tumor control, whereas higher values of

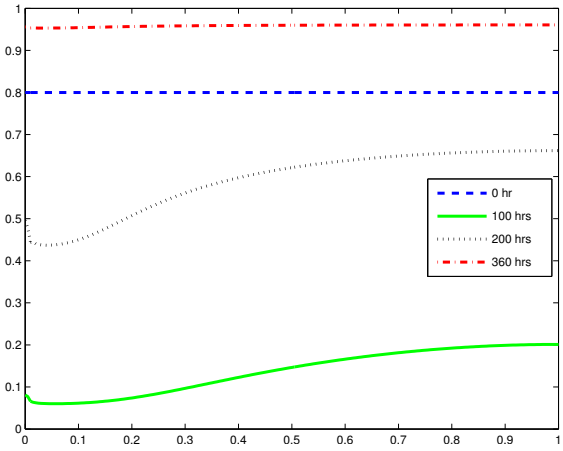

(a) Uninfected tumor cells

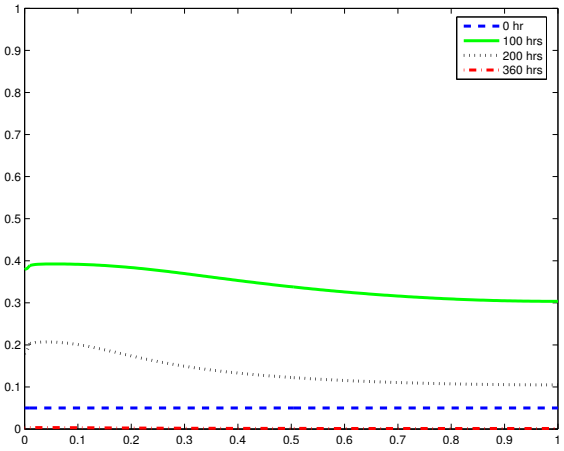

(b) Innate immune cells

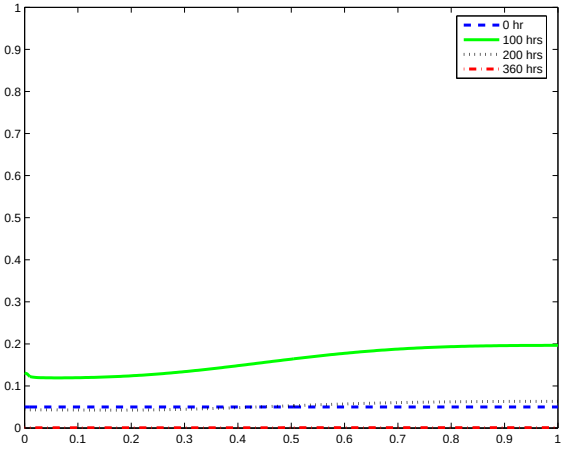

(c) Adaptive immune cells

FIG. 24: Distribution of uninfected tumor cells and immune cells at different times.

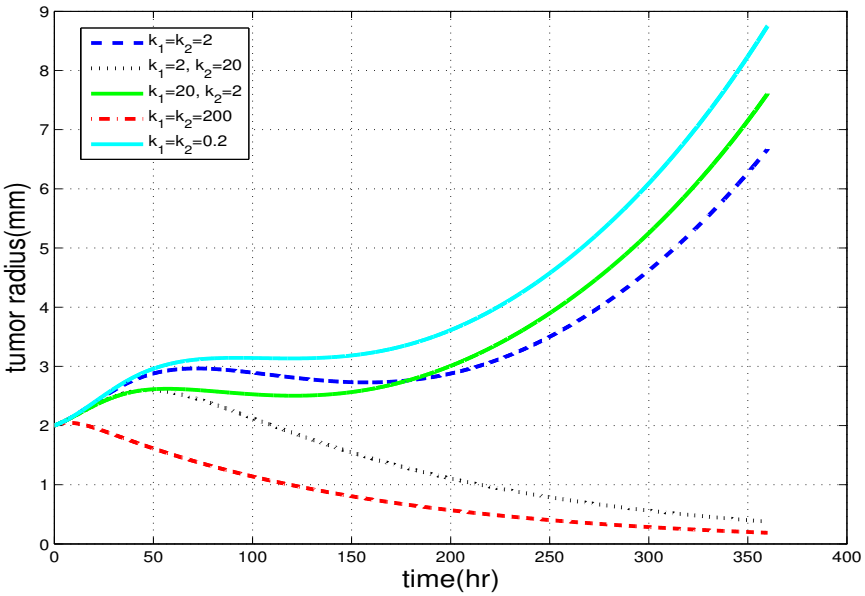

FIG. 25: Tumor growth with different immune killing rates.

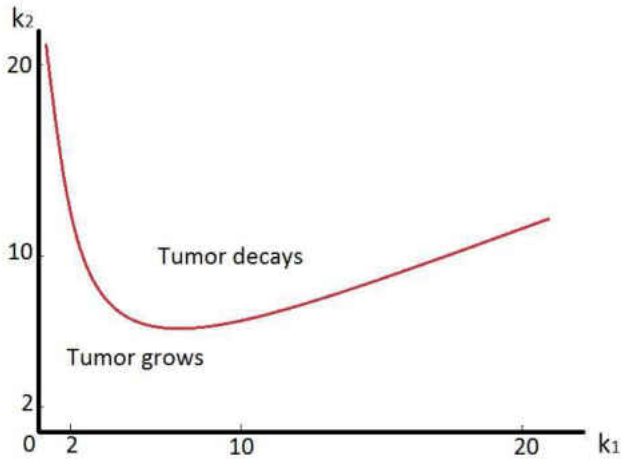

FIG. 26: A bifurcation diagram for tumor growth with respect to the two immune killing rates.

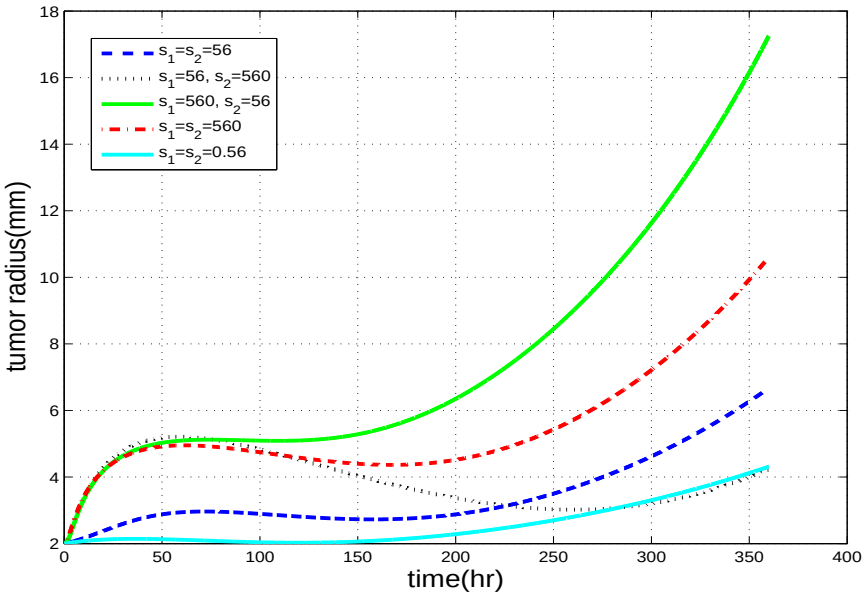

FIG. 27: Tumor growth with different immune stimulation rates.

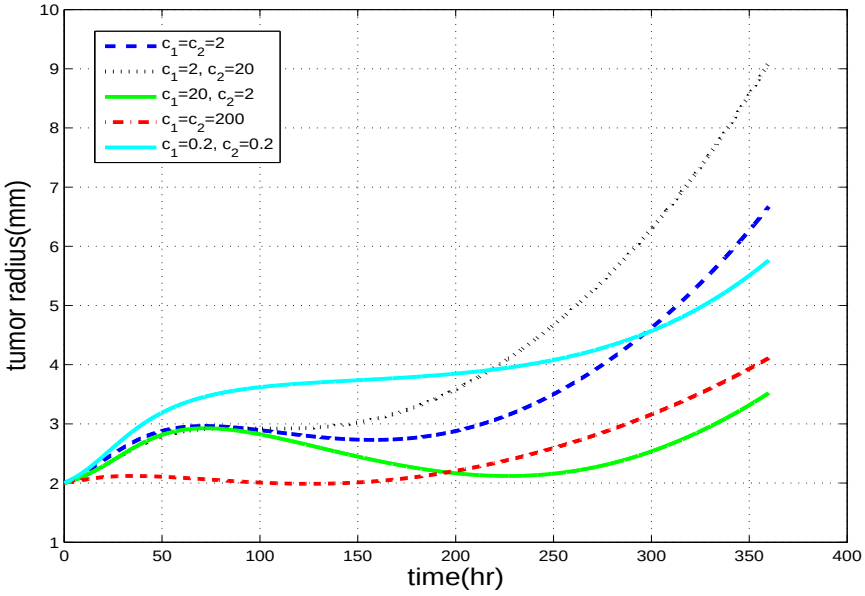

FIG. 28: Tumor growth with different immune clearing rates.

c_2 shows signs of tumor growth at a faster rate. Similar to Figure 27, although long term decay is not achieved, it is necessary to note that higher values of c_1 (and lower values of c_2) have positive influences in the virotherapy process. The parameter variation in k_1, k_2, s_1, s_2, c_1, and c_2 complement our knowledge of how the two immune cells work in opposing fashion. For a positive response in the virotherapy process, parameters values implicating lower activity of innate immunity(for example- low innate immune killing rate, low innate stimulation rate, and high innate clearance rate) and higher activity of adaptive immunity are preferable.

Next, we perform a study on the viral burst size, b, representing the number of new viruses coming out from a lysis of an infected tumor cell. The burst size is a direct measurement of the replicability of the viruses and is expected to play an important role in the virotherapy. With higher values of b, new viruses are generated faster which could promote the efficacy of the therapy. Figure 29 shows the growth of the tumor with respect to several different values of b, while fixing all other parameters at their base values. The pattern is clear: when b decreases, the tumor grows faster; when b increases, the growth of the tumor slows down. In particular, with a relatively big value $b = 8$, the tumor decreases in size for a period as long as 250 hours ($50 \leq t \leq 300$), before it starts re-growing.

In addition, we are interested in explicitly assessing the contribution from each of the two types of immune responses. We do this through comparing the baseline solution with two hypothetical (and extreme) cases: (1) only the innate immunity is present; (2) only the adaptive immunity is present. As can be observed from the system (50), if $Z_1 = 0$ at $t = 0$, then Z_1 would stay at 0 for all the time. The same is true for Z_2. Thus, we may remove one type of immunity from the model, while retaining the other, by changing the initial conditions. Figure 30 shows several scenarios along this line. We see that for the two cases where the adaptive immunity is absent ($Z_2 = 0$), the tumor grows faster in comparison with the baseline growth curve, and the one with higher initial value of Z_1 outcompetes the other. In contrast, for the two cases where the innate immunity is absent ($Z_1 = 0$), the tumor grows slower, and has a much longer non-growth period, than that for the baseline curve.

3.4.3 EFFECTS OF DELAYED ADAPTIVE IMMUNITY

In the model (50), we have assumed that the two types of immune responses, innate and adaptive, would be stimulated simultaneously and get started at the same time. In reality,

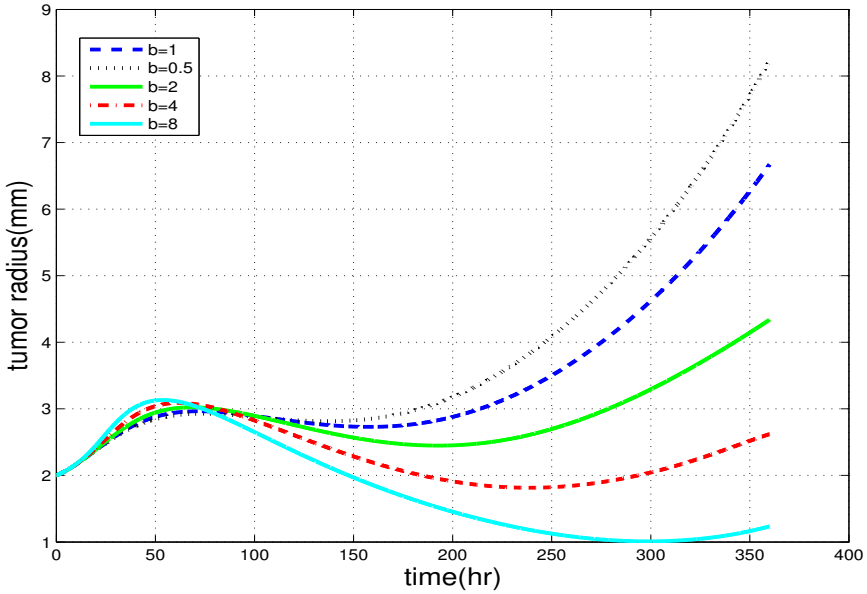

FIG. 29: Tumor growth with different values of viral burst size.

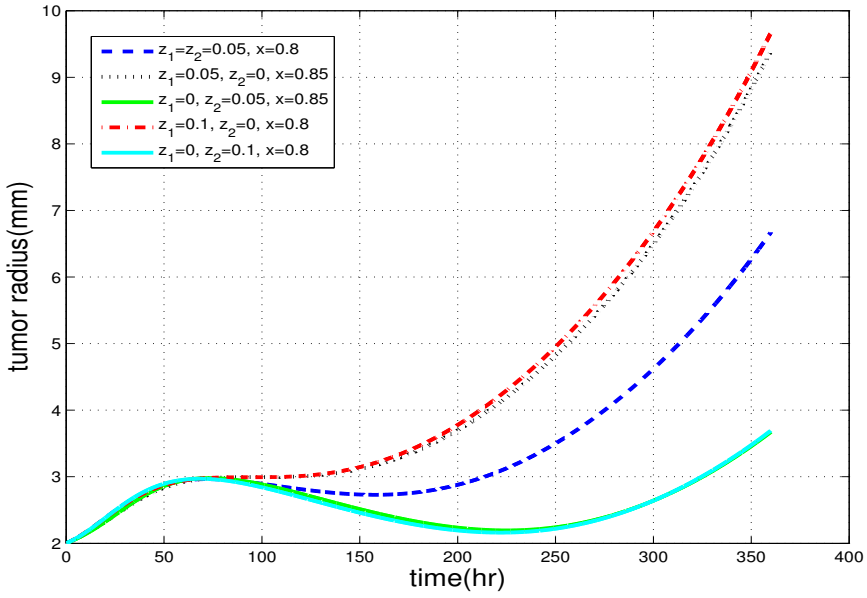

FIG. 30: Impact of the two immune systems on tumor growth, where x, z_1 and z_2 denote the initial profiles of X, Z_1 and Z_2 , respectively.

however, it is observed that although the innate immune response is fast and can be treated as instantaneous, the adaptive immune response is typically on a slower pace; it may take a time frame of several hours to activate the adaptive immune system after the viruses are injected into, and start interacting with, the tumor [49, 53]. Thus, there could be a gap between the starting times of the two immune responses, and such non-synchronization may have additional impact on the efficacy of the virotherapy.

To investigate this issue, we introduce a time delay to our equation for the adaptive immunity (Z_2). Thus, equation (50d) becomes

$$\frac{\partial Z_2}{\partial t} + \frac{1}{\rho^2}\frac{\partial}{\partial \rho}(\rho^2 U Z_2) = s_2 Y(\rho, t-T) Z_2(\rho, t-T) - c_2 Z_2 \,, \tag{72}$$

where T is a constant that represents the delay in the stimulation of the adaptive immune response. Consequently, equation (50g) will be replaced by

$$\frac{1}{\rho^2}\frac{\partial}{\partial \rho}(\rho^2 U) = \lambda X + s_1 Y Z_1 + s_2 Y(\rho, t-T) Z_2(\rho, t-T) - c_1 Z_1 - c_2 Z_2 - \mu N \,. \tag{73}$$

Other equations in the system (50) will remain the same.

The numerical methods described in the previous section can be applied, with minor modification, to compute our tumor model with the time delay. Results are presented below.

Figure 31 shows the comparison for the growth of the tumor without delay ($T = 0$) and with several different delays ($T = 5$, 10, 80, 100 hours), using the baseline parameter values given in Table 5. For the first 100 hours or so, there is little difference among the five cases, as the cell-virus interaction is in the initial phase of adjustment and the tumor is still growing for most of this initial period. The difference becomes apparent later on, especially when the tumor starts re-growing after the non-growth period ($t > 200$). It appears that the re-growth rate increases with T; the case with the largest delay ($T = 100$ hours) grows the fastest among the five, though the two curves with $T = 80$ and $T = 100$ almost coincide with each other. An implication is that a delayed start of the adaptive immune response would not significantly impact the virotherapy in the short term; i.e., the first few days, when the therapy is not yet, or just starts being, fully effective. Instead, the delayed adaptive immunity would make a difference for the longer-term development of the tumor, in a negative way: the more delayed (up to $T = 100$ hours), the faster the tumor re-grows.

With the delayed adaptive immunity, we have also performed a study on the variation of a few key model parameters, and we observe similar patterns as shown in Figure 25 for different immune killing rates, Figure 29 for different burst sizes, as well as Figure 30 for different initializations of the two immune responses. For illustration, Figure 32 compares the two cases of $T = 0$ (without delay) and $T = 5$ hours (with delay) for two sets of hypothetical values of the immune killing rates. For each set of values for k_1 and k_2, the anti-tumor immune effects have been strong enough so that the tumor radius would quickly decrease immediately after the initial growth, and there is no re-growth happening. For each case, however, there is a difference between the scenario of no delay and that of 5 hours delay: the curve with $T = 5$ is above the one with $T = 0$, showing a slower decay rate. The difference is only apparent during the decay phase of the tumor and is not noticeable during the initial growth period. Meanwhile, Figure 33 shows two choices of the burst size for the cases $T = 0$ and $T = 5$, while other model parameters are fixed at their base values. For each choice of b, the tumor development exhibits three phases: initial growth, non-growth (decay), and re-growth. The two curves $T = 0$ and $T = 5$, for each b, almost coincide with each other during the first two phases, but only move away from each other during the re-growth phase; the one with delay re-grows faster than the other. In all these results, a delayed adaptive immunity appears to have a negative impact on the efficacy of the virotherapy, but only for the longer-term development of the tumor.

In addition, we remark that our model provides an explicit means to represent the delay of the adaptive immune response. Alternatively, such a delay may be incorporated in an implicit manner. For example, if we assume that the innate immune response plays a role in triggering the adaptive immune response (see more discussion in [56]), we may modify the right-hand side of equation (72) by $s_2 Y Z_1 Z_2 - c_2 Z_2$, without explicit dependence on the delay T. We have found through our numerical simulation that such an implicit approach could reproduce some of the results shown here for our explicit delay model.

3.4.4 EFFECTS OF LARGE BURST SIZE

It has been shown that the viral burst size, b, plays an important role in the process of virotherapy. In particular, increased efficacy of the therapy has been observed with higher values of b (see Figures 29 and 33). Biomedically, the oncolytic viruses can be engineered so as to produce different burst sizes, possibly at large values. For example, Kambara et

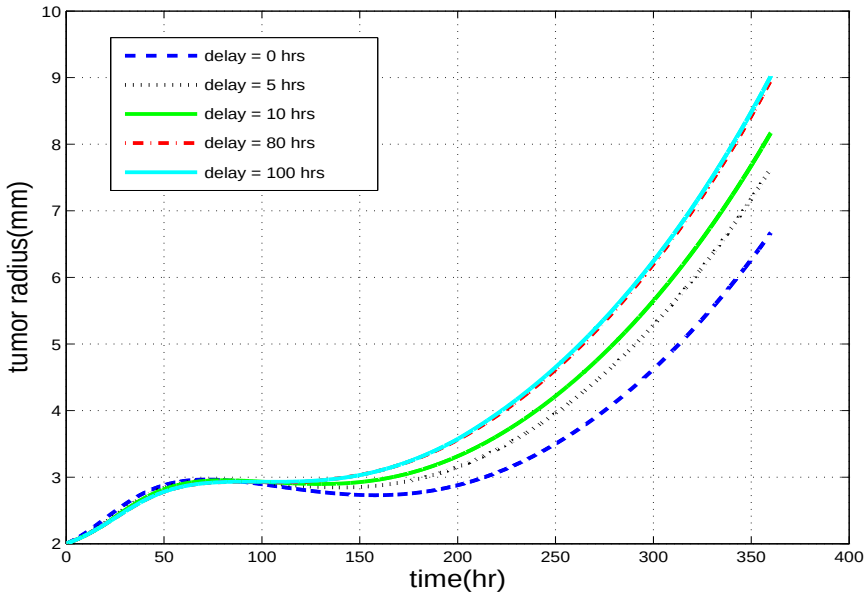

FIG. 31: Tumor growth with and without delay in the adaptive immune response.

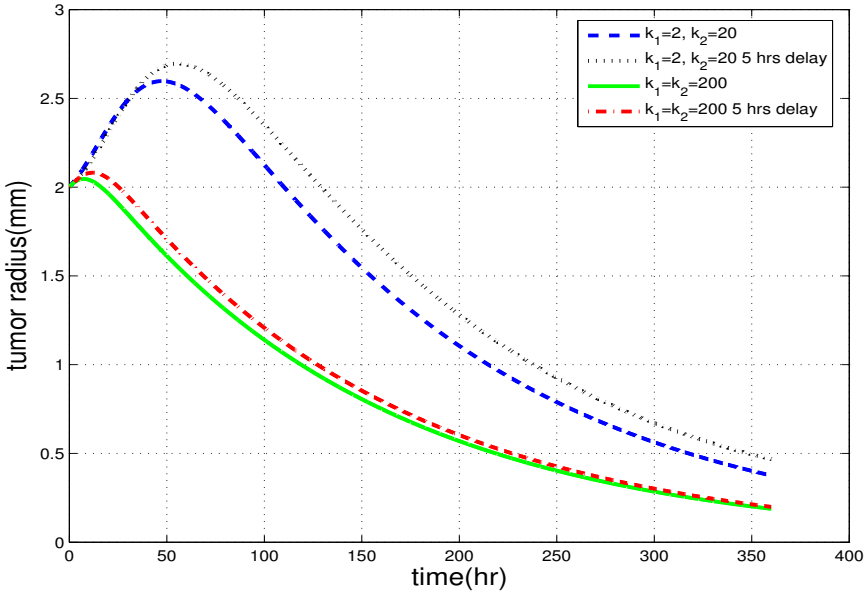

FIG. 32: Tumor growth with and without delay for two different sets of immune killing rates.

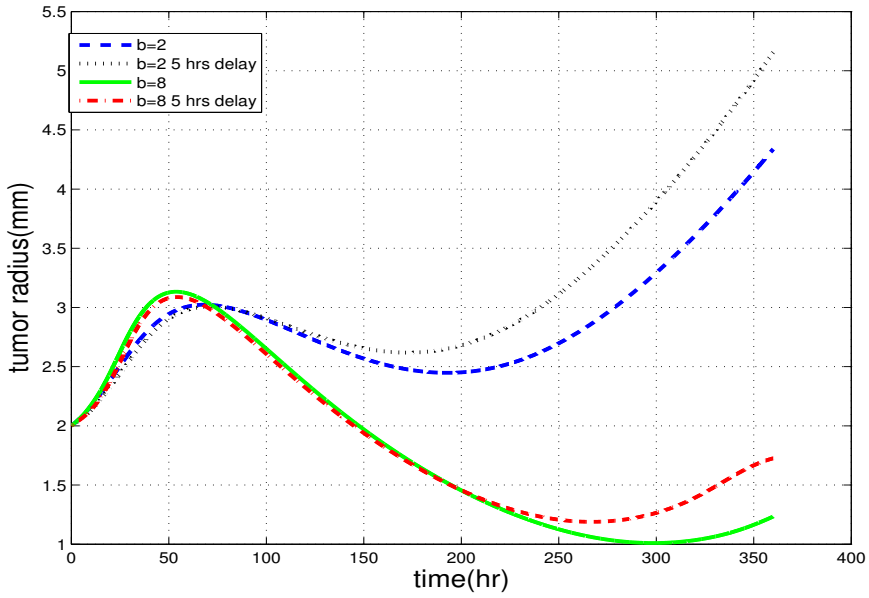

FIG. 33: Tumor growth with and without delay for two different choices of viral burst size.

al. [44] reported a new glioma-specific virus (herpes simplex virus type 1 mutant) with a high replication capability that led to significantly increased survivals of animals (mice) with brain tumors. Additionally, it is known that for some wild-type herpes simplex viruses, the burst size ranges in the thousands [41]. Thus, a natural question in our study is to explore the consequence of large burst size (hence high replicability) regarding the tumor development, in the complex interaction among tumor cells, viruses, and immune responses, and even with delayed adaptive immunity.

As shown in Figure 29, when increasing the value of b slightly above its baseline value, the length of the non-growth period is increased, though the tumor would eventually re-grow. Additional numerical investigation reveals that when b gets even larger, the efficacy will be further increased: when $b \geq 10$, the tumor will eventually shrink to a level almost at 0, after several cycles of decay and re-growth; when $b \geq 50$, there will be no re-growth taking place for the tumor. Figure 34 illustrates the situations with three larger burst sizes: 10, 25, 100. For $b = 10$ and 25, we still observe some re-growth trends, but all happening after $t = 300$ hours. For $b = 100$, the tumor development only exhibits two phases: an initial growth, followed by a quick decay to a size very close to 0 at $t \approx 700$. Once approaching there, the tumor size remains at that extremely low level for all the time $t > 700$, indicating that the

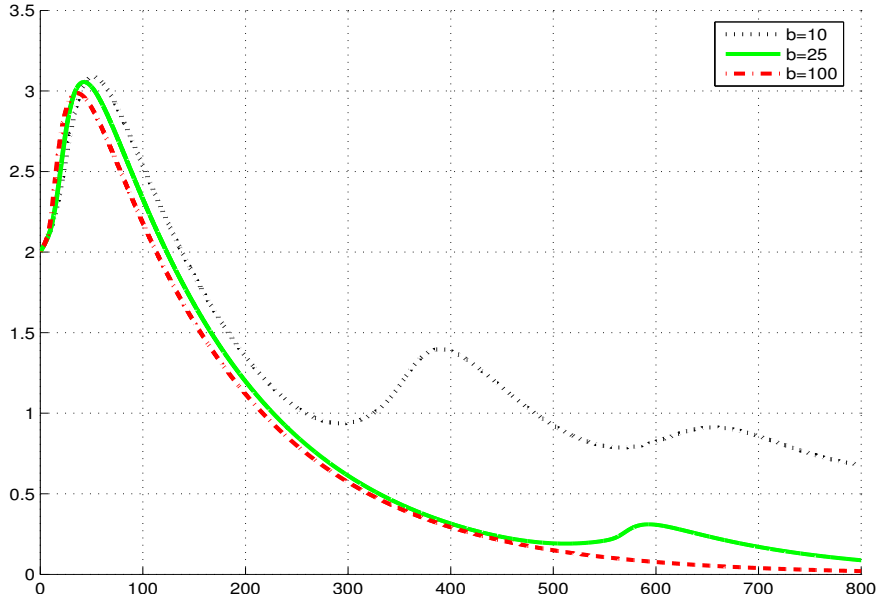

FIG. 34: Tumor growth with large values of viral burst size.

tumor has essentially been eliminated.

Figure 35 shows the time evolution of the distributions for the uninfected tumor cells and the innate immune cells, with the same initial settings as those in Figure 24, but with a large burst size $b = 100$. In contrast to the results in Figure 24, we now observe that X keeps decreasing and, at $t = 12.5$ hours, the value of X is already very close to 0. Though not shown here, X will stay at that level for all the later times, an indication of the success of the therapy. Meanwhile, the values of Z_1 and Z_2 keep increasing and eventually reach the levels around 65% and 15%, respectively, due to the continuing stimulation of the viruses and infected tumor cells. These are consistent with the tumor growth pattern shown in Figure 34.

3.4.5 EFFECTS OF REPEATED VIRUS INJECTION

Our study so far has focused on the case with a single virus injection which is administered in the beginning of the treatment ($t = 0$). In a recent virotherapy clinical trial [35], a virus dose was administered (via intratumoral injection) every two weeks to several hundreds of patients with skin cancer and the outcomes were encouraging, with demonstrated therapeutic benefit for patients with metastatic tumors. This result suggests the importance

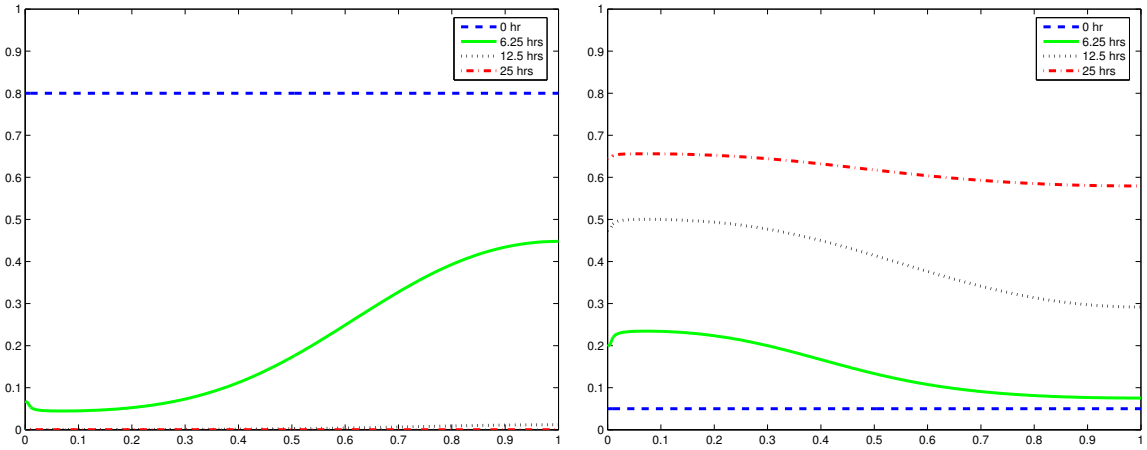

(a) Uninfected tumor cells

(b) Innate immune cells

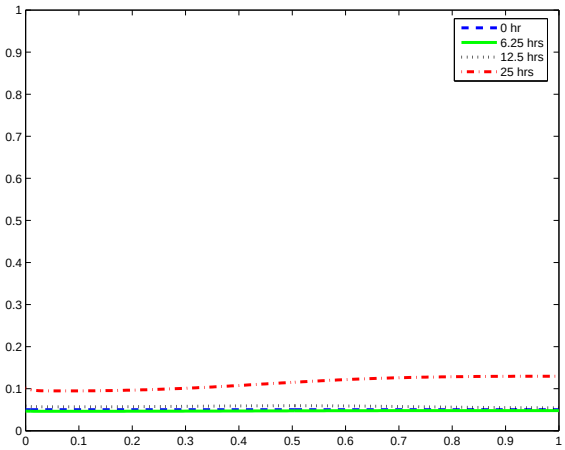

(c) Adaptive immune cells

FIG. 35: Distribution of uninfected tumor cells and immune cells at different times with a large burst size $b = 100$.

of continuing treatment through repeated virus injection.

We proceed to numerically test this scenario by re-setting the virus distribution to its initial configuration (see equation 59b) in every two weeks, or 336 hours. This represents a biweekly injection of viruses into the tumor center. Other conditions and parameters are kept at their default (or, baseline) values. Figure 36 compares the tumor growth with such a biweekly virus injection and with a single virus injection (at $t = 0$), where $b = 1$, 10 and 100, respectively. For the first two cases, the improvement of efficacy with the repeated virus doses is evident; particularly, for $b = 10$, the tumor shrinks much faster than that with a single virus dose in the beginning. For the third case, $b = 100$, the two types of virus administrations do not make any difference, as the viral burst size has been large enough so that only a single virus dose is needed to quickly control (and conquer) the tumor.

3.5 ODE MODEL FOR STABILITY ANALYSIS

In order to study the stability of the tumor model, we will start with the partial differential equations based model presented earlier and reduce it to an ordinary differential equations(ODE) model. In this section, we present complete detail of the mathematical model and stability based on ODEs along with the numerical method. We chose to implement an ODE based model for the stability study mainly because of their flexibility, robustness, ease of analysis, ability to capture complex interaction along with the simplicity of implementing. We present numerical results that conform to the theoretical findings. In the final part, we analyze the stability of the boundary and positive equilibrium points using various analytical and numerical methods.

3.5.1 MATHEMATICAL MODEL

The relationship between the effect of virus and the growth of tumor is very complex in nature. There are several models that have been developed and analyzed based on virotherapy treatment of tumor cells, see [69] and references therein for detail. A defining feature of the ODE models is the compartmentalization of uninfected tumor, infected tumor, and virus. In this section, we stick with this idea but with an addition of innate and adaptive immune cells which play a major role in the virotherapy treatment of cancer. Note that in this section we will constantly refer back to the PDE model as presented in equation (50).

In order to obtain a simplified ODE model from the previously discussed model, assume

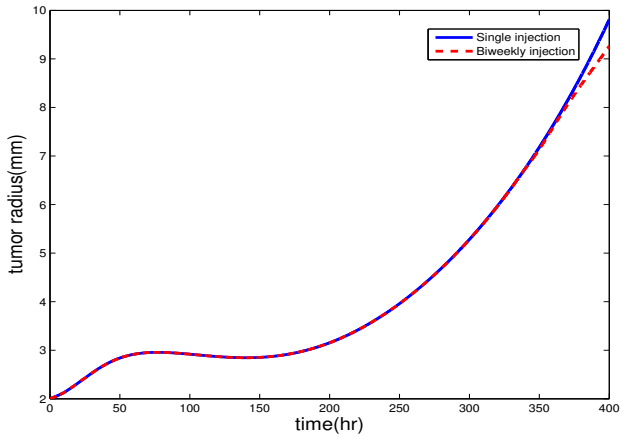

(a) $b = 1$

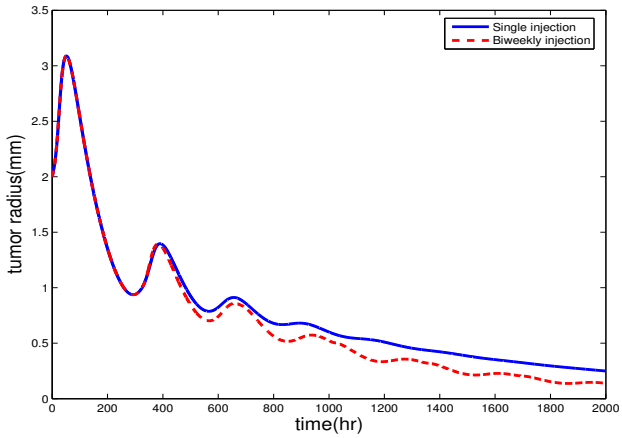

(b) $b = 10$

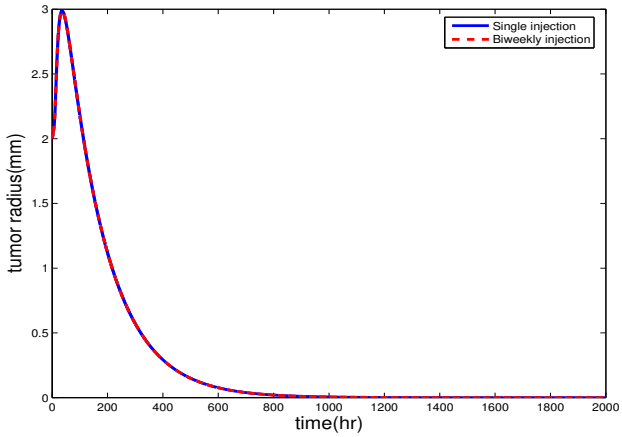

(c) $b = 100$

FIG. 36: Tumor growth with single virus injection and repeated biweekly virus injection, using different values of viral burst size.

X=$X(t)$ = number density of uninfected tumor cells
Y=$Y(t)$= number density of infected tumor cells
Z_1=$Z_1(t)$= number density of innate immune cells(natural killer cells)
Z_2=$Z_2(t)$= number density of adaptive immune cells(T cells)
V=$V(t)$= number density of viruses(HSV) that are not contained in cancer cells
N=$N(t)$= number density of dead tumor cells

Then, $\frac{1}{\rho^2}\frac{\partial}{\partial\rho}(\rho^2 UX) = X\frac{1}{\rho^2}\frac{\partial}{\partial\rho}(\rho^2 U)$.

Using equation (50g), equation (50a) becomes

$$\frac{dX}{dt} = \lambda X - \beta XV - k_2 XZ_2 - X[\lambda X + s_1 YZ_1 + s_2 YZ_2 - c_1 Z_1 - c_2 Z_2 - \mu N]$$

Substituting $N = \theta - X - Y - Z_1 - Z_2$, we obtain

$$\begin{aligned}\frac{dX}{dt} &= (\lambda + \mu\theta)X - (\lambda+\mu)X^2 - \mu XY - (\mu - c_1)XZ_1 \\ &\quad - (\mu - c_2 + k_2)XZ_2 - \beta XV - s_1 XYZ_1 - s_2 XYZ_2,\end{aligned} \tag{74a}$$

Repeating the process for all the equations in (50), we obtain the following system of nonlinear ordinary differential equations:

$$\begin{aligned}\frac{dY}{dt} &= (\mu\theta - \delta)Y - (\lambda+\mu)XY + \beta XV - \mu Y^2 \\ &\quad - (k_1 + \mu - c_1)YZ_1 - (\mu - c_2)YZ_2 - s_1 Y^2 Z_1 - s_2 Y^2 Z_2,\end{aligned} \tag{74b}$$

$$\begin{aligned}\frac{dZ_1}{dt} &= (\mu\theta - c_1)Z_1 - (\lambda+\mu)XZ_1 + (s_1 - \mu)YZ_1 + (c_1 - \mu)Z_1^2 \\ &\quad + (c_2 - \mu)Z_1 Z_2 - s_1 YZ_1^2 - s_2 YZ_1 Z_2,\end{aligned} \tag{74c}$$

$$\begin{aligned}\frac{dZ_2}{dt} &= (\mu\theta - c_2)Z_2 - (\lambda+\mu)XZ_2 + (s_2 - \mu)YZ_2 + (c_1 - \mu)Z_1 Z_2 \\ &\quad + (c_2 - \mu)Z_2^2 - s_1 YZ_1 Z_2 - s_2 YZ_2^2,\end{aligned} \tag{74d}$$

$$\frac{dV}{dt} = b\delta Y - k_0 Z_1 V - \gamma V, \tag{74e}$$

Finally multiplying equation (50g) by ρ^2 and integrating both sides from 0 to R, we get

$$\frac{dR}{dt} = \frac{R}{3}\big[\lambda X + s_1 Y Z_1 + s_2 Y Z_2 - c_1 Z_1 - c_2 Z_2 - \mu(\theta - X - Y - Z_1 - Z_2)\big] \tag{74f}$$

We assume that all the above mentioned cells have the same size and are uniformly distributed in the tumor. We also assume that the total cell density is a constant , i.e.

$$X + Y + Z_1 + Z_2 + N = \theta = Constant \tag{75}$$

The values of the parameters in the above equations are the same as the ones in Table 5.

3.5.2 NUMERICAL METHOD AND RESULTS

Based on experimental results, we use the following initial conditions in (76) to start the numerical solution.

$$R(0) = 2\,\text{mm} \tag{76a}$$

$$V(0) = 1 \tag{76b}$$

$$X(0) = 0.8\,\text{cells/mm}^3, \quad \text{Y}(0) = 0.1\,\text{cells/mm}^3, \tag{76c}$$

$$Z_1(0) = 0.05\,\text{cells/mm}^3, \quad \text{Z}_2(0) = 0.05\,\text{cells/mm}^3 \tag{76d}$$

We use the four-stage fourth order Runge Kutta method to update X, Y, Z_1, Z_2, V and R. We present few cases here that will confirm to our earlier findings and theoretical expectations. This will also help verify our ODE model and the numerical method being used. We start with a numerical simulation with initial virus configuration $V(0)$ of 14.5 (which is simply a mean approximation of the virus profile used earlier in the PDE system) and test out several burst sizes. As seen in Figure 37, the tumor decays irrespective of the burst size.

We then change the initial virus size to 1 and repeat the same test in Figure 38. With this much smaller virus injection, we clearly see that burst size is indirectly proportional to the tumor growth, i.e. as burst size increases tumor decreases. This shows that even on a much smaller dose, there are ways to stabilize the tumor and prevent tumor regrowth. It also

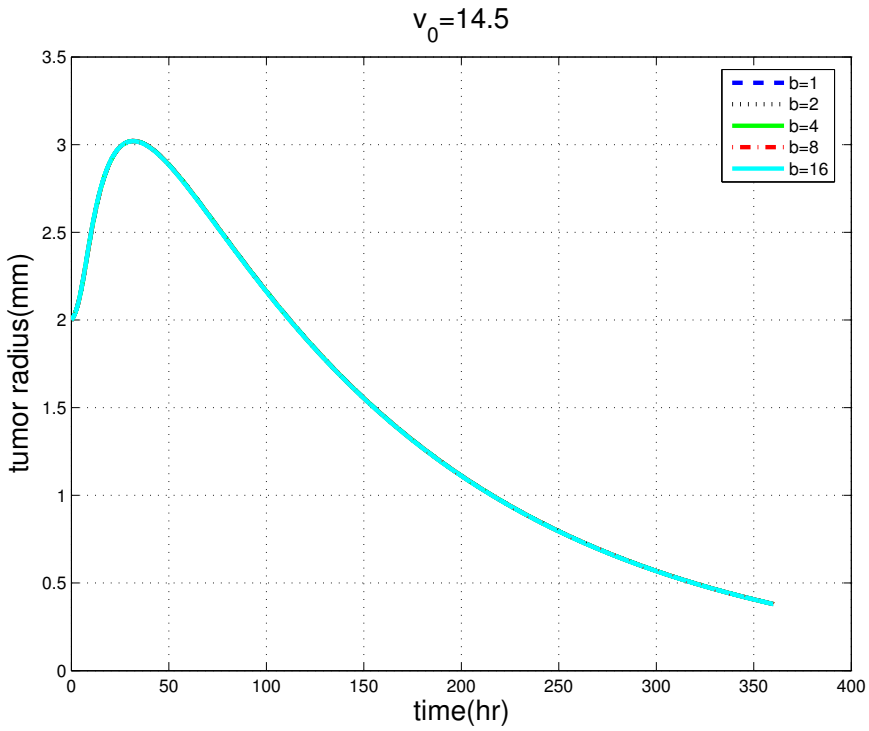

FIG. 37: Variation in b, fixed initial $v_0 = 14.5$

displays same phases as we have seen before in Figure 23, i.e. tumor growth, non-growth(or decay), and re-growth.

Figure 39 shows the effect of variation of initial virus configuration for a fixed burst size, $b = 1$. The higher the initial virus size, the lower the growth rate of the tumor, which is as expected. This is an attest to the fact that higher initial dose of virus administration will lead to tumor decay irrespective of other parameters; however this is not always a feasible approach as large doses of viruses can also cause deadly effects on normal cells.

The subplots in Figure 40 show the profile of uninfected tumor cells, infected tumor cells, innate and adaptive tumor cells, and virus cells over time for different burst sizes b. The uninfected tumor cells show an initial phase of decrease in cells followed by an increase, where for the higher burst sizes we see a sharper decline in the first phase and slower increase in the second phase. For burst sizes greater than 4, the uninfected tumor cells does not increase past its initial setting, i.e. the uninfected tumor is controlled. The infected tumor cells in general show a quick decay after an initial increase, albeit higher burst sizes implies faster decay.

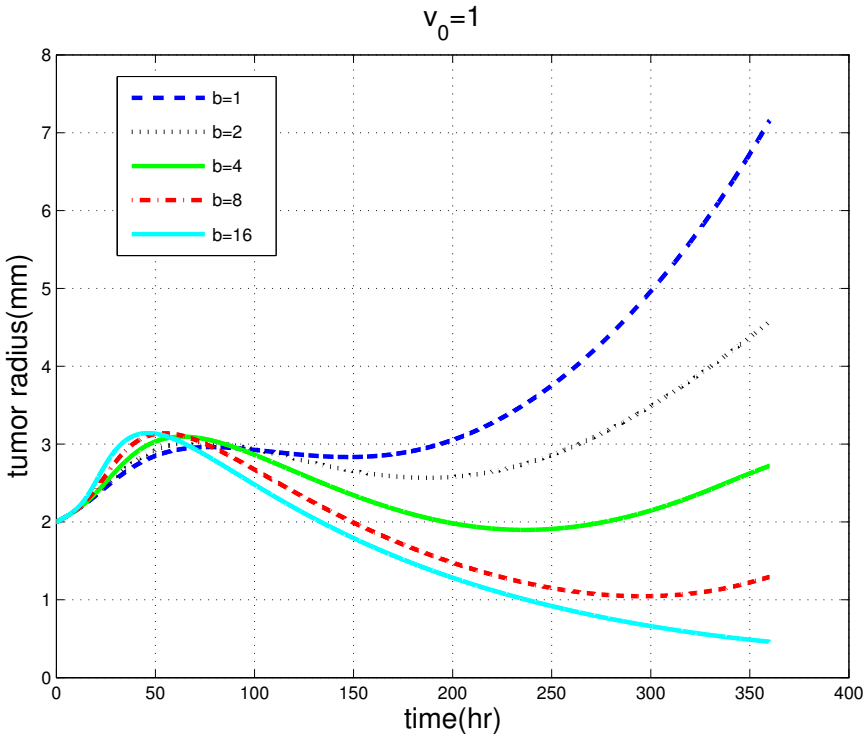

FIG. 38: Variation in b, fixed initial $v_0 = 1$

Both the immune cells increase in a similar fashion as the burst size decreases, however we have use same values for parameters related to the immune system, for example the killing rates, the stimulation rates, etc. More experiments are required to distinguish the values of such parameters. The virus cells show an initial phase of increase as the burst size increases, followed by a second phase where the virus cells get closer to 0 around 150 hours for all burst sizes; i.e. the viruses are almost completely eliminated from the system.

3.5.3 STABILITY ANALYSIS OF BOUNDARY EQUILIBRIUM

An equilibrium point or critical point is a solution of the differential equation that is constant over time. An equilibrium may or may not be stable. It is useful to be able to identify equilibrium points based on their stability as they provide greater insight in the dynamics of the system. An equilibrium point is said to be locally stable if initial conditions that start near an equilibrium point tend to move towards the equilibrium over time. If this is true irrespective of initial conditions, we call this a globally stable equilibrium point. We

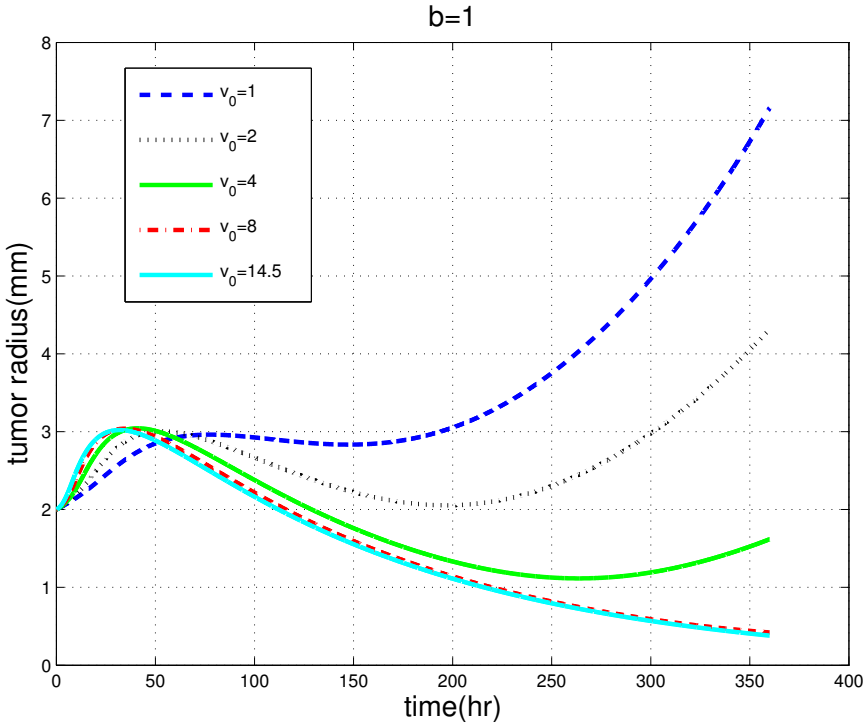

FIG. 39: Variation in v_0, fixed b

will divide the stability analysis section into two parts; first we will look at the boundary equilibrium using the linear stability analysis; then we will focus on the endemic solution using computational methods.

Let $\vec{R} = (\ X(t),\ Y(t),\ Z_1(t),\ Z_2(t),\ V(t)\ )$. Writing out the set of ordinary differential equations in Equation 74 in vector form, we get $\dot{\mathbf{R}} = \mathbf{f}(\mathbf{R})$. If $\mathbf{r}$ is an equilibrium point, then by definition $\mathbf{f}(\mathbf{r}) = \mathbf{0}$. We then expand the right hand side of the differential equation using multivariate Taylor expansion. The first order term should be sufficient to understand the behavior of the trajectories close to the equilibrium point, so we have

$$\dot{\mathbf{R}} = \mathbf{f}(\mathbf{r}) + \left.\frac{\partial \mathbf{f}}{\partial \mathbf{R}}\right|_{\mathbf{r}} (\mathbf{R} - \mathbf{r}) + ... \tag{77a}$$

$$= \left.\frac{\partial \mathbf{f}}{\partial \mathbf{R}}\right|_{\mathbf{r}} (\mathbf{R} - \mathbf{r}) + ... \tag{77b}$$

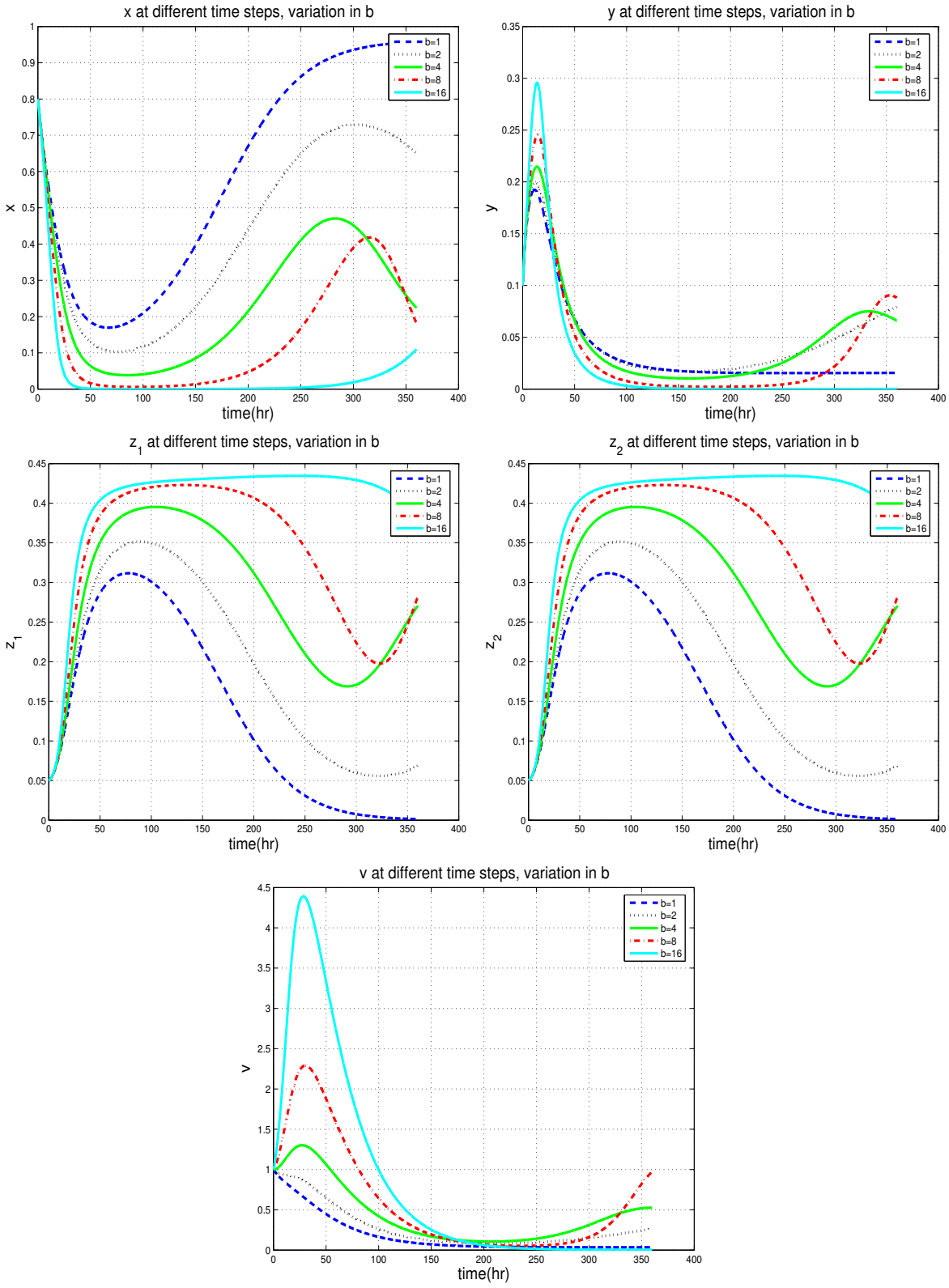

FIG. 40: Cell densities and viruses over time, variation in b

The components of $\mathbf{f}$ are given by,

$$f_1 = (\lambda + \mu\theta)X - (\lambda + \mu)X^2 - \mu XY - (\mu - c_1)XZ_1 \tag{78a}$$
$$- (\mu - c_2 + k_2)XZ_2 - \beta XV - s_1XYZ_1 - s_2XYZ_2,$$
$$f_2 = (\mu\theta - \delta)Y - (\lambda + \mu)XY + \beta XV - \mu Y^2 \tag{78b}$$
$$- (k_1 + \mu - c_1)YZ_1 - (\mu - c_2)YZ_2 - s_1Y^2Z_1 - s_2Y^2Z_2,$$
$$f_3 = (\mu\theta - c_1)Z_1 - (\lambda + \mu)XZ_1 + (s_1 - \mu)YZ_1 + (c_1 - \mu)Z_1^2 \tag{78c}$$
$$+ (c_2 - \mu)Z_1Z_2 - s_1YZ_1^2 - s_2YZ_1Z_2,$$
$$f_4 = (\mu\theta - c_2)Z_2 - (\lambda + \mu)XZ_2 + (s_2 - \mu)YZ_2 + (c_1 - \mu)Z_1Z_2 \tag{78d}$$
$$+ (c_2 - \mu)Z_2^2 - s_1YZ_1Z_2 - s_2YZ_2^2,$$
$$f_5 = b\delta Y - k_0Z_1V - \gamma V, \tag{78e}$$

Ignoring the higher order terms in the expansion, equation (77) can be interpreted as a Jacobian matrix. Then the Jacobian matrix of Equation 78 evaluated at the equilibrium point $\mathbf{r}(\ x,\ y,\ z_1, z_2,\ v)$, which is obtained by differentiating the right hand side of the system (78 with respect to x, y, z_1, z_2 and v, is given by the following

$$\hat{J} = \begin{bmatrix}
\begin{matrix}(\lambda+\mu\theta)-2x(\lambda+\mu)\\ -\mu y-(\mu-c_1)z_1\\ -(\mu-c_2+k_2)z_2\\ -\beta v-s_1yz_1-s_2yz_2\end{matrix} & \begin{matrix}-\mu x-s_1xz_1\\ -s_2xz_2\end{matrix} & \begin{matrix}-(\mu-c_1)x\\ -s_1xy\end{matrix} & \begin{matrix}-(\mu-c_2+k_2)x\\ -s_2xy\end{matrix} & -\beta x \\
\begin{matrix}-(\lambda+\mu)y+\beta v\end{matrix} & \begin{matrix}(\mu\theta-\delta)-(\lambda+\mu)x\\ -2\mu y-(k_1+\mu-c_1)z_1\\ -(\mu-c_2)z_2\\ -2s_1yz_1-2s_2yz_2\end{matrix} & \begin{matrix}-(k_1+\mu-c_1)y\\ -s_1y^2\end{matrix} & \begin{matrix}-(\mu-c_2)y\\ -s_2y^2\end{matrix} & \beta x \\
\begin{matrix}-(\lambda+\mu)z_1\end{matrix} & \begin{matrix}(s_1-\mu)z_1-s_1z_1^2\\ -s_2z_1z_2\end{matrix} & \begin{matrix}(\mu\theta-c_1)\\ -(\lambda+\mu)x\\ +(s_1-\mu)y\\ +(c_2-\mu)z_2\\ +2z_1(c_1-\mu)\\ -2s_1yz_1\\ -s_2yz_2\end{matrix} & \begin{matrix}(c_2-\mu)z_1\\ -s_2yz_1\end{matrix} & 0 \\
\begin{matrix}-(\lambda+\mu)z_2\end{matrix} & \begin{matrix}(s_2-\mu)z_2-s_2z_2^2\\ -s_1z_1z_2\end{matrix} & \begin{matrix}(c_1-\mu)z_2\\ -s_1yz_2\end{matrix} & \begin{matrix}(\mu\theta-c_2)\\ -(\lambda+\mu)x\\ +(s_2-\mu)y\\ +(c_1-\mu)z_1\\ +2z_2(c_2-\mu)\\ -2s_2yz_2\\ -s_1yz_1\end{matrix} & 0 \\
0 & b\delta & -k_0v & 0 & \begin{matrix}-k_0z_1\\ -\gamma\end{matrix}
\end{bmatrix}$$

In this section and the next one, we analyze the boundary equilibrium points analytically and the interior (or positive) equilibrium through numerical simulations. The equilibrium

is said to be locally asymptotically stable if all the eigenvalues of the Jacobian matrix have negative real parts. For all cases, we set $\theta = 1$, and assume that all parameters like λ, μ, etc are greater than 0.

3.5.4 $\mathbf{R} = (0, 0, 0, 0, 0)$

The Jacobian for this trivial equilibrium point is given by,

$$\hat{J} = \begin{bmatrix} \lambda+\mu & 0 & 0 & 0 & 0 \\ 0 & \mu-\delta & 0 & 0 & 0 \\ 0 & 0 & \mu-c_1 & 0 & 0 \\ 0 & 0 & 0 & \mu-c_2 & 0 \\ 0 & b\delta & 0 & 0 & -\gamma \end{bmatrix}$$

The eigenvalues of the above 5x5 matrix is given by the solution of the deterministic equation $|\hat{J} - qI| = 0$, where q are the eigenvalues.

It is easy to verify that the roots are: $\lambda+\mu$, $\mu-\delta$, $\mu-c_1$, $\mu-c_2$, $-\gamma$. Since $(\lambda+\mu) > 0$, we conclude that this equilibrium is not locally stable.

The biological interpretation of this equilibrium point is that the infected, uninfected, innate immune, adaptive immune cells and viruses are all destroyed. This scenario is almost impossible in real situation and the solution is not stable.

3.5.5 $\mathbf{R} = (1, 0, 0, 0, 0)$

The Jacobian for this simple equilibrium is given by,

$$\hat{J} = \begin{bmatrix} (\lambda+\mu)-2(\lambda+\mu) & -\mu & -(\mu-c_1) & -(\mu-c_2+k_2) & -\beta \\ 0 & (\mu-\delta)-(\lambda+\mu) & 0 & 0 & \beta \\ 0 & 0 & (\mu-c_1)-(\lambda+\mu) & 0 & 0 \\ 0 & 0 & 0 & (\mu-c_2)-(\lambda+\mu) & 0 \\ 0 & b\delta & 0 & 0 & -\gamma \end{bmatrix}$$

$$= \begin{bmatrix} -(\lambda+\mu) & -\mu & -(\mu-c_1) & -(\mu-c_2+k_2) & -\beta \\ 0 & -(\delta+\lambda) & 0 & 0 & \beta \\ 0 & 0 & -(c_1+\lambda) & 0 & 0 \\ 0 & 0 & 0 & -(c_2+\lambda) & 0 \\ 0 & b\delta & 0 & 0 & -\gamma \end{bmatrix}$$

We now solve the deterministic equation $|\hat{J} - qI| = 0$. The equation simplifies to the following:

$$0 = [-(\lambda+\mu)-q][-(c_1+\lambda)-q][-(c_2+\lambda)-q] \begin{vmatrix} -(\delta+\lambda)-q & \beta \\ b\delta & -\gamma-q \end{vmatrix} \tag{79a}$$

$$= [-(\lambda+\mu)-q][-(c_1+\lambda)-q][-(c_2+\lambda)-q][(\delta+\lambda+q)(\gamma+q)-\beta b\delta] \tag{79b}$$

Clearly, the first three roots result in negative eigenvalues. So let's focus on the last two roots which are obtained by solving the quadratic equation:

$$0 = (\delta+\lambda+q)(\gamma+q) - \beta b\delta$$
$$0 = q^2 + (\lambda+\delta+\gamma)q + (\delta\gamma + \lambda\gamma - \beta b\delta)$$

Therefore,

$$q = \frac{-(\lambda+\delta+\gamma) \pm \sqrt{(\lambda+\delta+\gamma)^2 - 4(\delta\gamma+\lambda\gamma-\beta b\delta)}}{2}$$

Case when: $(\lambda+\delta+\gamma)^2 \leq 4(\delta\gamma+\lambda\gamma-\beta b\delta)$. Then $Re(q) < 0$ since λ, δ, $\gamma > 0$.

Case when: $(\lambda+\delta+\gamma)^2 > 4(\delta\gamma+\lambda\gamma-\beta b\delta)$. Let $\epsilon = \sqrt{(\lambda+\delta+\gamma)^2 - 4(\delta\gamma+\lambda\gamma-\beta b\delta)}$, $\epsilon > 0$.

i) $q = \frac{-(\lambda+\delta+\gamma)-\epsilon}{2}$. Here, $q < 0$.

ii) $q = \frac{-(\lambda+\delta+\gamma)+\epsilon}{2}$. For a negative real eigenvalue, we need $(\lambda+\delta+\gamma) > \epsilon$. This is true when $\delta\gamma + \lambda\gamma > \beta b\delta$.

This equilibrium is locally asymptotically stable for $\delta\gamma + \lambda\gamma > \beta b\delta$.

The biological interpretation of this equilibrium point is that all the other cells destroy but the uninfected tumor cells remain. This is not ideal for the removal of the tumor. So the stability, although stable for certain condition, is not very helpful for the virotherapy.

3.5.6 $\mathbf{R} = (0, 1, 0, 0, 0)$

The Jacobian for this simple equilibrium is given by,

$$\hat{J} = \begin{bmatrix} \lambda & 0 & 0 & 0 & 0 \\ -(\lambda+\mu) & -(\mu+\delta) & -(k_1+\mu-c_1+s_1) & -(\mu-c_2+s_2) & 0 \\ 0 & 0 & (s_1-c_1) & 0 & 0 \\ 0 & 0 & 0 & (s_2-c_2) & 0 \\ 0 & b\delta & 0 & 0 & -\gamma \end{bmatrix}$$

We now solve the deterministic equation $|\hat{J} - qI| = 0$. After inspecting the first eigenvalue λ, we conclude that the equilibrium is not locally stable.

The biological interpretation of this equilibrium point is that all the other cells destroy but the infected tumor cells remain. This is similar to the previous case and is not ideal for the removal of the tumor.

3.5.7 $\mathbf{R} = (0, 0, 1, 0, 0)$

The Jacobian for this simple equilibrium is given by,

$$\hat{J} = \begin{bmatrix} (\lambda+c_1) & 0 & 0 & 0 & 0 \\ 0 & -(k_1-c_1+\delta) & 0 & 0 & 0 \\ -(\lambda+\mu) & -\mu & -(\mu-c_1) & (c_2-\mu) & 0 \\ 0 & 0 & 0 & (c_1-c_2) & 0 \\ 0 & b\delta & 0 & 0 & -\gamma \end{bmatrix}$$

We now solve the deterministic equation $|\hat{J} - qI| = 0$. After inspecting the first eigenvalue $\lambda + c_1$, we conclude that the equilibrium is not locally stable.

The biological interpretation of this equilibrium point is that all the other cells destroy but the innate immune cells remain. This equilibrium is not stable.

3.5.8 R $= (0, 0, 0, 1, 0)$

The Jacobian for this simple equilibrium is given by,

$$\hat{J} = \begin{bmatrix} (\lambda + c_2 - k_2) & 0 & 0 & 0 & 0 \\ 0 & -(\delta - c_2) & 0 & 0 & 0 \\ 0 & 0 & (c_2 - c_1) & 0 & 0 \\ -(\lambda + \mu) & -\mu & (c_1 - \mu) & (c_2 - \mu) & 0 \\ 0 & b\delta & 0 & 0 & -\gamma \end{bmatrix}$$

We now solve the deterministic equation $|\hat{J} - qI| = 0$. The equation simplifies to the following:

$$[-(\lambda + c_2 - k_2) - q][-(\delta - c_2) - q][(c_2 - c_1) - q][(c_2 - \mu) - q][-\gamma - q] = 0$$

After inspecting the eigenvalues, we conclude that the equilibrium is locally stable if it satisfies the following conditions:

i) $k_2 < \lambda + c_2$

ii) $c_2 < \delta$

iii) $c_2 < c_1$

iv) $c_2 < \mu$

The biological interpretation of this equilibrium point is that all the other cells destroy but the adaptive immune cells remain. This equilibrium is conditionally stable. The tumor can be totally eradicated given the above conditions.

3.5.9 R $= (X, Y, 0, 0, 0)$

This reduces to previous cases: (0,0,0,0,0) and (1,0,0,0,0).

3.5.10 R $= (0, Y, 0, 0, V)$

Setting $z_1 = 0$ in equation (74e), we get $v = \frac{b\delta y}{\gamma}$.

From equation (74b), we get $(\mu - \delta)y - \mu y^2 = 0$. Either $y = 0$ or $y = \frac{\mu - \delta}{\mu}$.

When $y = 0$, $v = 0$. We have already looked at this case. When $y = \frac{\mu - \delta}{\mu}$, $v = \frac{b\delta(\mu - \delta)}{\mu\gamma}$. We will analyze this case here.

The Jacobian for this equilibrium is given by,

$$\hat{J} = \begin{bmatrix} (\lambda+\mu)-\mu y-\beta v & 0 & 0 & 0 & 0 \\ -(\lambda+\mu)y+\beta v & (\mu-\delta)-2\mu y & -(k_1+\mu-c_1)y-s_1y^2 & -(\mu-c_2)y-s_2y^2 & 0 \\ 0 & 0 & (\mu-c_1)+(s_1-\mu)y & 0 & 0 \\ 0 & 0 & 0 & (\mu-c_2)+(s_2-\mu)y & 0 \\ 0 & b\delta & -k_0v & 0 & -\gamma \end{bmatrix}$$

We now solve the deterministic equation $|\hat{J}-qI|=0$. The equation simplifies to the following:

$$[(\lambda+\mu)-\mu y-\beta v-q][(\mu-c_1)+(s_1-\mu)y-q][(\mu-c_2)+(s_2-\mu)y-q] \\ [(\mu-\delta)-2\mu y-q][-\gamma-q]=0$$

Substituting the values of y and v, we get,

$$[(\lambda+\mu)-(\mu-\delta)-\frac{\beta b\delta(\mu-\delta)}{\mu\gamma}-q][(\mu-c_1)+(s_1-\mu)\frac{\mu-\delta}{\mu}-q][(\mu-c_2)+(s_2-\mu)\frac{\mu-\delta}{\mu}-q] \\ [(\mu-\delta)-2(\mu-\delta)-q][-\gamma-q]=0$$

After inspecting the eigenvalues, we conclude that the equilibrium is locally stable if it satisfies the following conditions:

i) $(\lambda-\delta)<(\mu-\delta)\frac{\beta b\delta}{\mu\gamma}$

ii) $(\mu-c_1)<(\mu-s_1)\frac{\mu-\delta}{\mu}$

iii) $(\mu-c_2)<(\mu-s_2)\frac{\mu-\delta}{\mu}$

iv) $\delta<\mu$

The biological interpretation of this equilibrium point is that the infected cells and the viruses exist and the equilibrium is conditionally stable which means that the size of the tumor is constant and will not increase.

3.5.11 STABILITY ANALYSIS OF ENDEMIC EQUILIBRIUM

The endemic equilibrium state is the state where the disease cannot be totally eradicated but remains in the population [68]. The endemic equilibrium, where each component is strictly positive, is biologically most interesting, but also analytically most challenging. So, we use the Newton Raphson iterative method to solve the system of equations and thus compute endemic equilibrium $\mathbf{r} = (x, y, z_1, z_2, v)$. The system of non linear equations $\mathbf{f}(\mathbf{r}) = \mathbf{0}$ using the higher dimensional Newton-Raphson iterative method can be summarized as follows. This method is a generalization of the one dimensional case to solve multiple simultaneous algebraic equations given by

$$f_i(x, y, z_1, z_2, v) = f_i(\mathbf{r})$$

The Newton-Raphson formula for multi-variate problem is

$$\mathbf{r} \Leftarrow \mathbf{r} - J_f^{-1}(\mathbf{r})\mathbf{f}(\mathbf{r})$$

where $J_f(\mathbf{r})$ is the Jacobian of $\mathbf{f}(\mathbf{r})$.

For the numerical analysis in this section, we will adhere to the parameters in 5 unless otherwise noted. We ran multiple simulations, mainly around the parameter- burst size b in order to test the stability of the system. After careful numerical simulation, we conclude that there is a burst size b^* such that when $b <= b^*$, there exists a endemic equilibrium; when $b > b^*$, there exists a limit cycle for the given set of parameters in Table 5. After numerous simulations, b^* is found to be 20. Figure 41 tracks tumor and immune cell densities along with viruses over time for $b = 20$. As seen in the plot, all the cells and viruses converge to a stable point after some time. In the next few sections, we will provide examples of four different cases which will yield stable equilibrium, and limit cycles. Furthermore, we have identified the dependence of the solution in certain initial condition setting where we can achieve either a globally or a multiple locally stable equilibria.

3.5.12 GLOBALLY STABLE ENDEMIC EQUILIBRIUM WHEN INITIAL CONDITION $Z_1 = Z_2$ FOR $b <= 20$

Here, we analyze the equilibrium points where the initial condition $z_1 = z_2$, for $b <= 20$. Due to our choices of parameters ($c_1 = c_2$, $k_1 = k_2$, $s_1 = s_2$) and the ODE system related to the innate and adaptive immune responses, the initial condition $z_1 = z_2$ will lead to

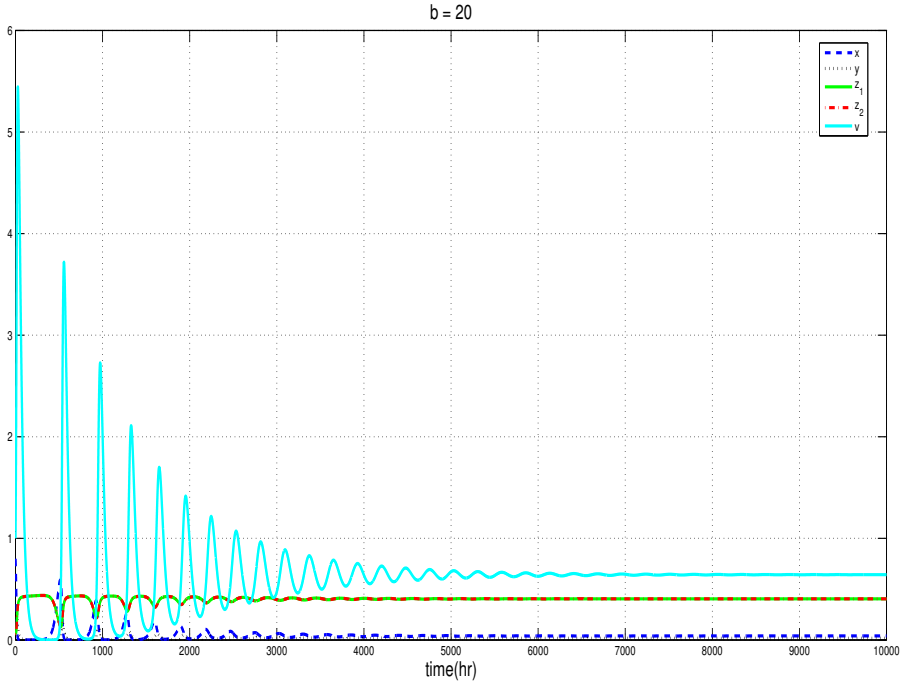

FIG. 41: Tumor and immune cell densities and virus for $b = 20$

$z_1 = z_2$ at all times. After careful numerical simulation of numerous initial conditions we conclude that we have a globally stable endemic equilibrium whenever $z_1 = z_2$. Here are some examples that display the phase portrait of these globally stable endemic equilibrium points with different initial conditions for a given set of parameters. In particular, we will closely look at two different initial conditions for $b = 8$, where $z_1 = z_2$. We tested this scenario with other values of $b <= 20$ and found similar results.

The endemic equilibrium for $b = 8$, with other parameters the same as before, is $(0.1089, 0.0298, 0.3559, 0.3559, 0.4634)$ for any initial conditions as long as $z_1 = z_2$. Although several different initial conditions were tested to validate our result, the initial conditions that will be presented here are $(0.8, 0.1, 0.05, 0.05, 1)$ and $(0.5, 0.1, 0.2, 0.2, 3)$, and will be referred to as Initial Condition 1 and 2 respectively. Figure 42 and 43 have two plots each showing: i) tumor and immune cells, and viruses that stabilizes over a long period of time, and ii) a phase portrait of the tumor cells that shows, in both cases, converge to the same global endemic equilibrium. The biological interpretation of this equilibrium point is that

all the cells and viruses exist and the equilibrium is stable. So the tumor can be controlled and it will not grow, no matter the initial densities of tumor and immune cells as long as the adaptive and innate cells are equal and the burst size $b <= 20$.

3.5.13 MULTIPLE LOCALLY STABLE EQUILIBRIUM WHEN INITIAL CONDITION $Z_1 \neq Z_2$ FOR $b <= 20$

This section differs from the previous section only in the initial values of innate and adaptive immune cell densities. We have multiple locally stable endemic equilibrium points whenever $z_1 \neq z_2$, for $b <= 20$. Below are some examples of such cases using different initial conditions for $b = 16$. All other parameters are kept the same as before. Two different initial conditions that will be presented here are $(0.3, 0.2, 0.1, 0.4, 0.5)$ and $(0.4, 0.4, 0.18, 0.02, 2)$, and will be referred to as Initial Condition 3 and 4 respectively. The system with the initial condition 3 converges to the endemic equilibrium $(0.0407, 0.0156, 0.1593, 0.6372, 0.5268)$, whereas the system that's initiated with the fourth condition converges to the endemic equilibrium $(0.0657, 0.0251, 0.7074, 0.0786, 0.6963)$. Several other initial conditions that satisfy $z_1 \neq z_2$ and the given set of parameters with $b <= 20$ are tested, and they all converge to different equilibrium points. Figures (44) and (45) show the cell densities over time along with the phase portrait of the tumor cell for two initial conditions that justifies the stability of the solution. The biological interpretation of these equilibria points are that all the cells and viruses exist in the system and the equilibrium is stable for the given set of parameters, and the tumor can be controlled.

3.5.14 LIMIT CYCLE FOR $b > 20$

With this choice of initial setting, we get a periodic solutions around the positive equilibrium point. This implies that the infected and uninfected tumor cells undergo oscillation. We present three examples for different burst sizes and initial conditions(two of them with $z_1 = z_2$ and one with $z_1 \neq z_2$). The simulations are run for a long period of time(> 10000 hours). For $b = 32$, we start with an initial condition of $(0.8, 0.1, 0.05, 0.05, 1)$, which we will refer to as Initial Condition 5. For $b = 50$, we will use the initial condition of $(0.5, 0.1, 0.2, 0.2, 3)$, which we will refer to as Initial Condition 6. Figures (46) and (47) show the plots of limit cycle for Initial conditions 5 and 6 respectively.

We provide one last example as a final case in the stability analysis of endemic equilibrium

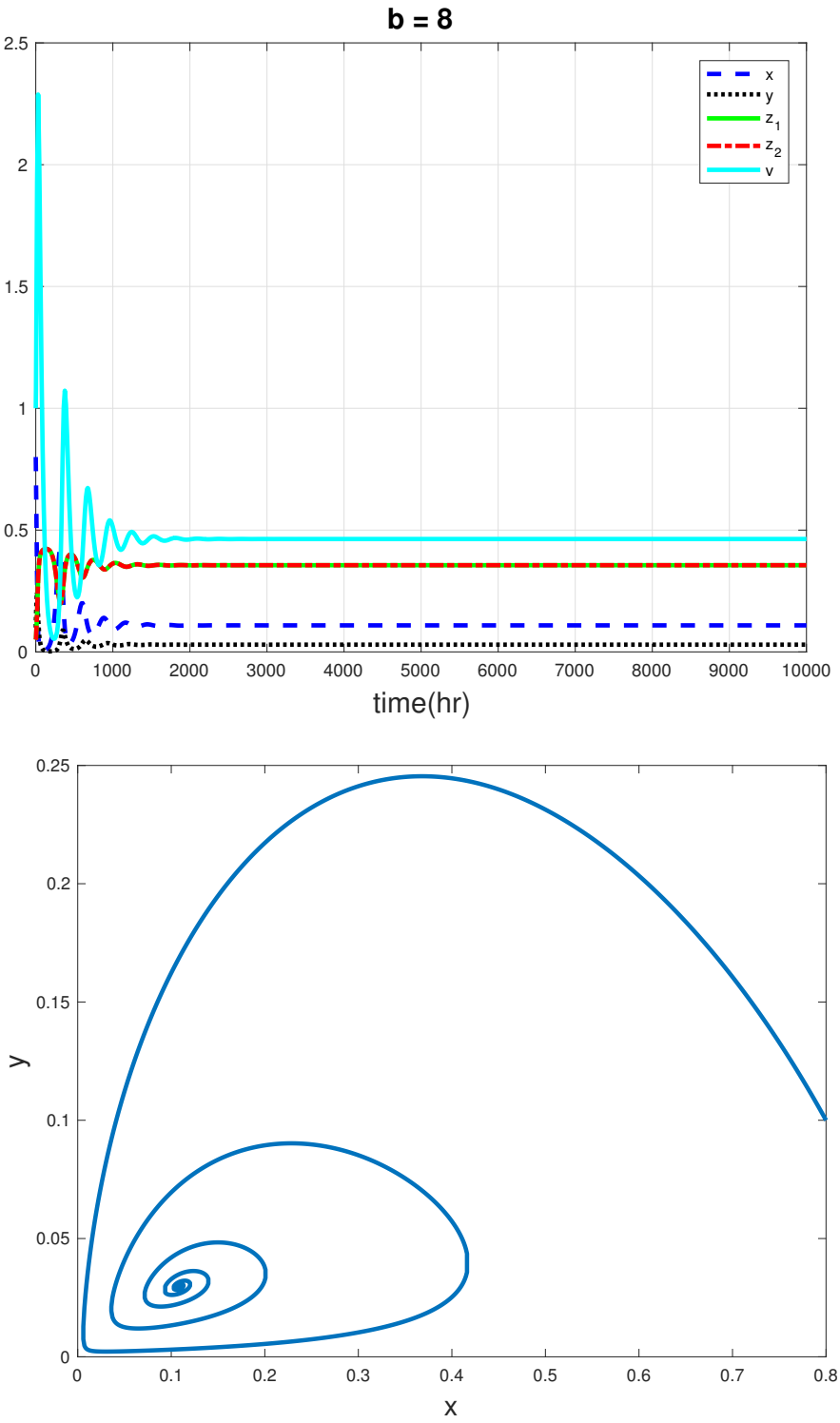

FIG. 42: Cell densities, viruses over time and phase portrait of tumor cells for Initial Condition 1, $b = 8$

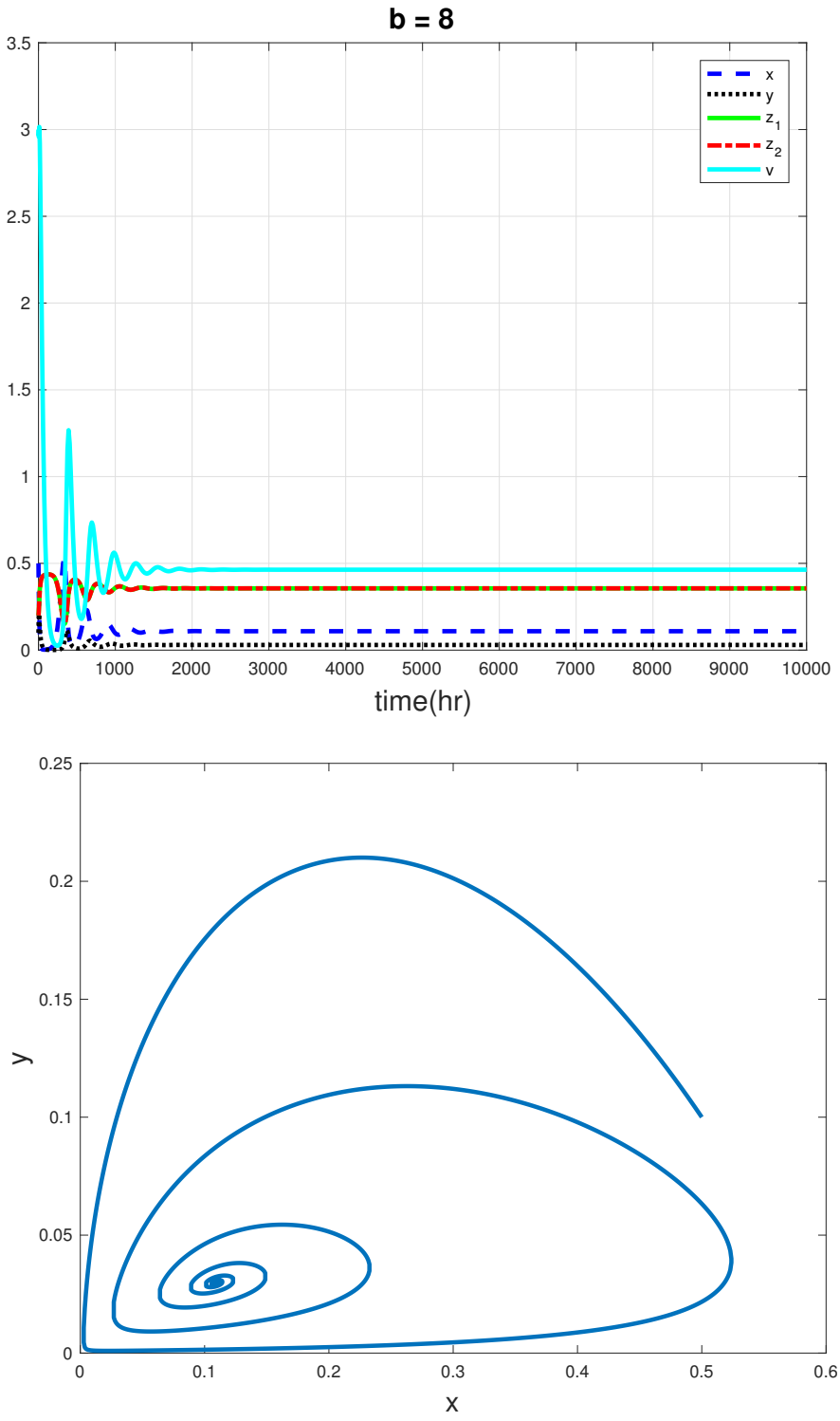

FIG. 43: Cell densities, viruses over time and phase portrait of tumor cells for Initial Condition 2, $b = 8$

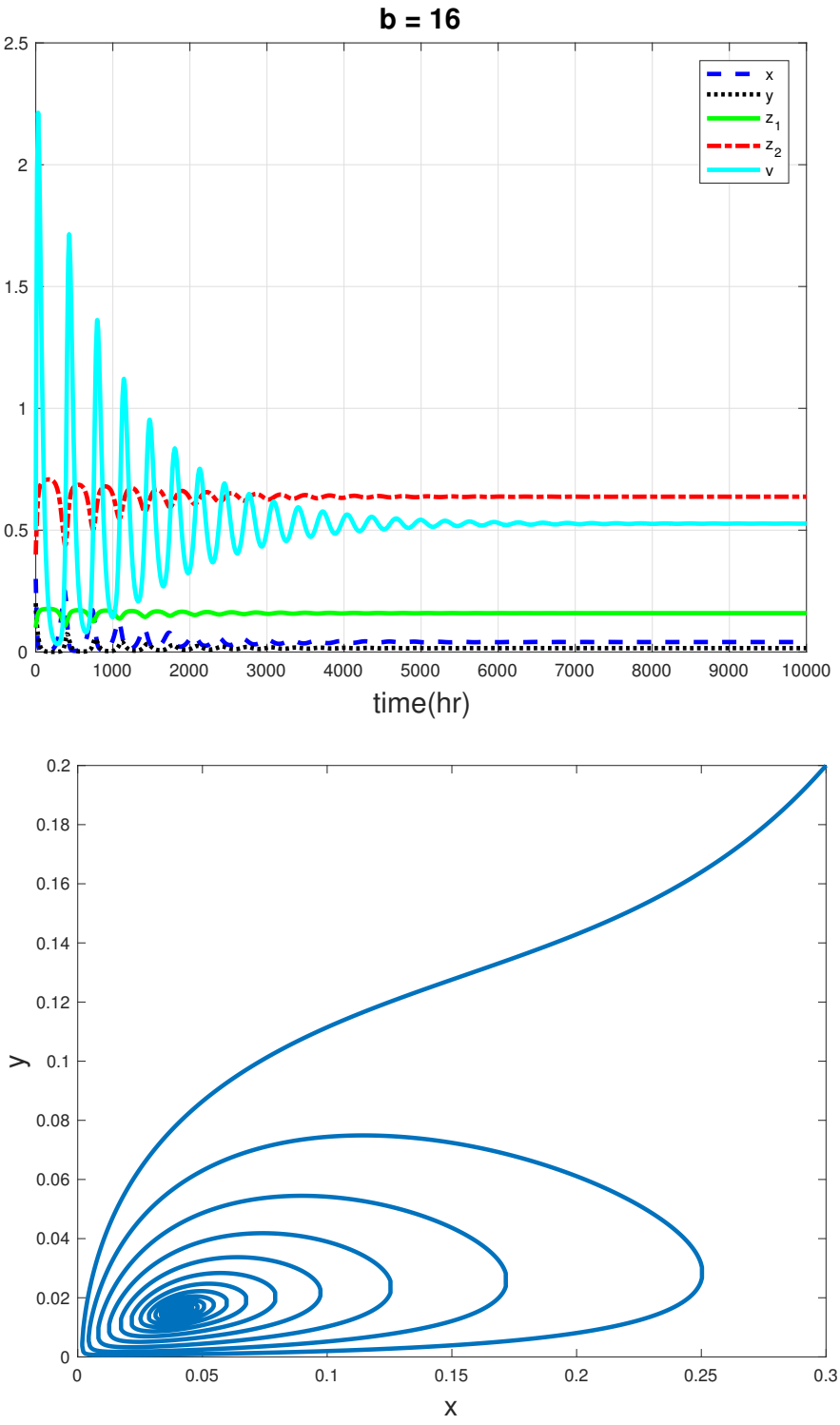

FIG. 44: Cell densities, viruses over time and phase portrait of tumor cells for Initial Condition 3, $b = 16$

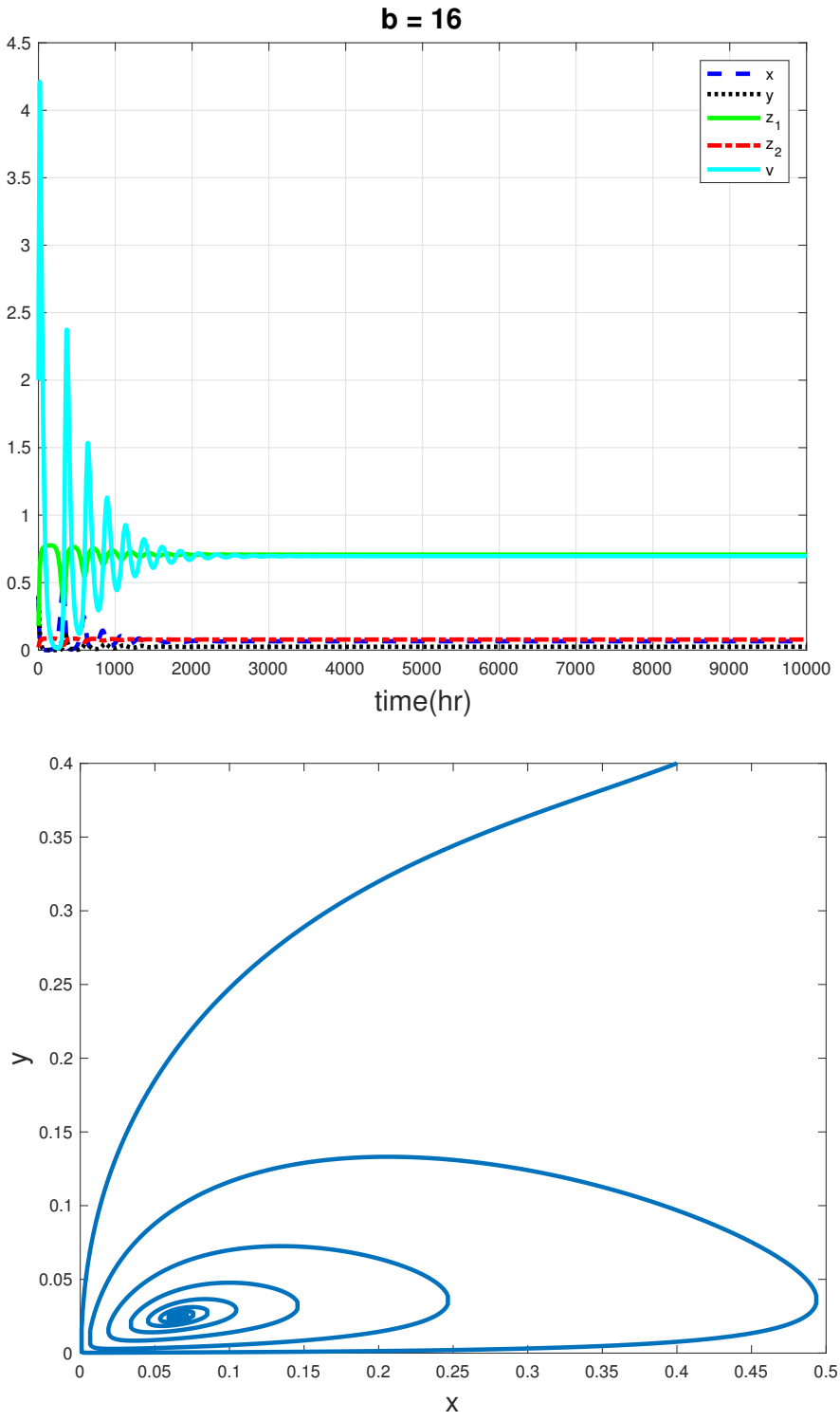

FIG. 45: Cell densities, viruses over time and phase portrait of tumor cells for Initial Condition 4, $b = 16$

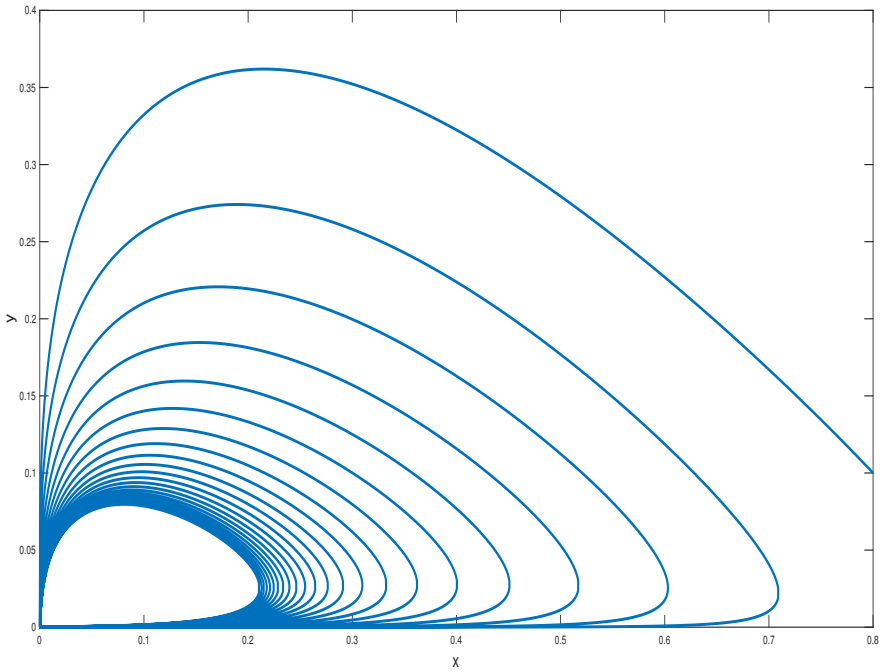

FIG. 46: Limit cycle for tumor cells for Initial Condition 5, $b = 32$

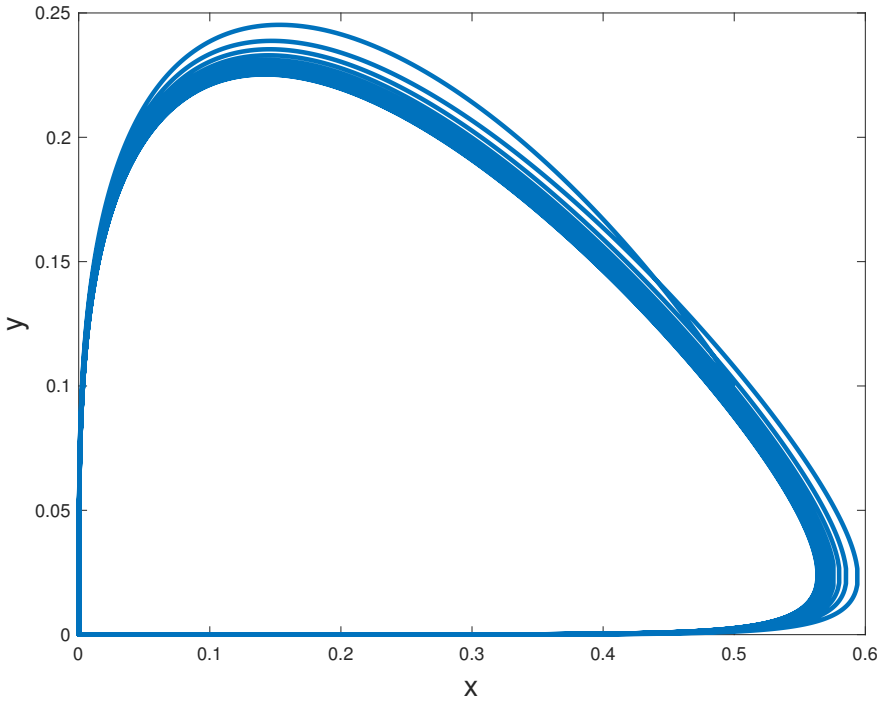

FIG. 47: Limit cycle for tumor cells for Initial Condition 6, $b = 50$

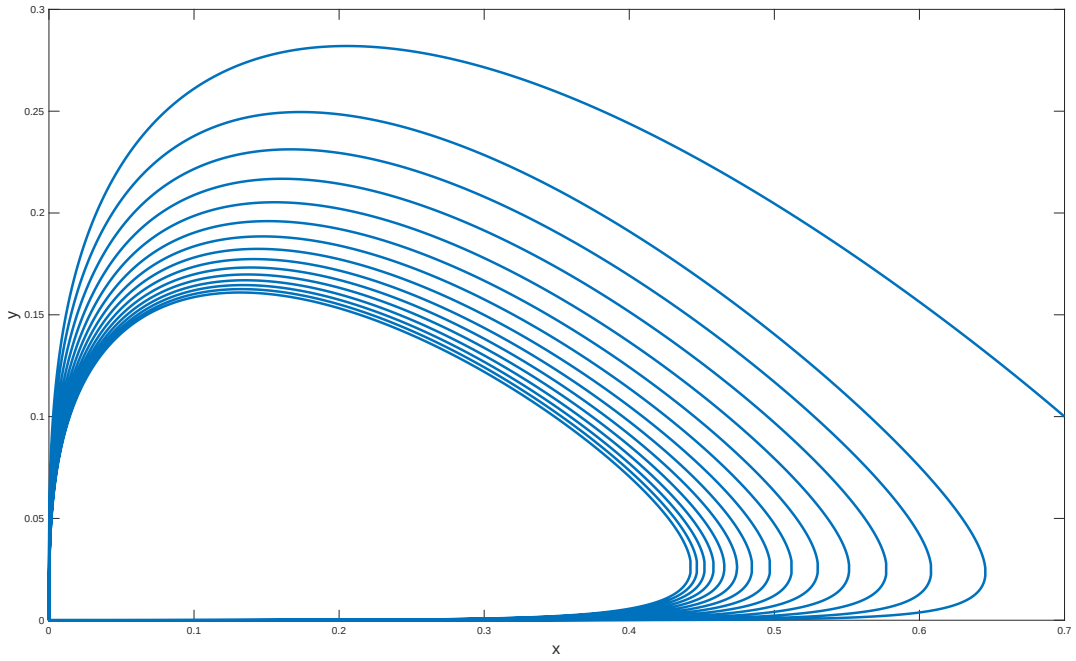

FIG. 48: Limit cycle for tumor cells for Initial Condition 7, $b = 32$

based on the selection of parameter burst size b and the initial condition on the two immune cells. Here we test a scenario where $z_1 \neq z_2$ for $b = 32$. For this, we set a slightly different initial condition of $(0.7, 0.1, 0.05, 0.15, 1)$ such that $z_1 \neq z_2$, which we will refer to as Initial Condition 7. This periodic solution as seen in Figure 48 is similar to the ones seen before in this section. This shows that we reach a limit cycle for $b > 20$ irrespective of the restriction on initial values of the innate and adaptive immune cells.

3.6 DISCUSSION

We have presented a new mathematical model for tumor virotherapy with virus mediated immune responses. The model is a system of PDEs that couples tumor growth with cell-virus-immune interactions and that describes the motion of tumor cells and viruses on a domain with a moving boundary. A distinctive feature of our model is the incorporation of both innate and adaptive immune responses in the course of tumor oncolysis, which, to our knowledge, has not been investigated in prior mathematical models and studies. The

modeling framework and the computational methods presented in this chapter allow us to conduct a novel and careful study on tumor dynamics under the virotherapy, in a wide range of settings that include varied parameters and initial conditions, delay in the adaptive immunity, and repeated viral doses.

Our results show that a typical scenario of tumor evolution under the virotherapy may exhibit three phases: initial growth, non-growth or even shrinking in size (which may correspond to a period of cancer dormancy), and re-growth (representing cancer recurrence). We have found, however, when the adaptive immune killing rate and/or the viral burst size are increased, the efficacy of the therapy is significantly improved. Particularly, with sufficiently large values for these parameters, tumor re-growth will not occur and the tumor will shrink to, and stabilize at, a size very close to 0. The findings suggest that genetically manipulating oncolytic viruses so as to promote the anti-tumor adaptive immunity and the viral replicability, would be potentially useful means to enhance the efficacy of the virotherapy. In addition, our results demonstrate that repeated administration of viral doses on regular intervals (e.g., two weeks) leads to improved efficacy, which is consistent with the clinical observation.

The presence of two different types of immune responses and their coupling with tumor growth and host-virus interaction are an emphasis of this work. We find that the immune responses are necessary for the success of the virotherapy. The ideal therapeutic outcome; i.e., removal of both the tumor and viruses, can be possibly achieved through genetically engineered viruses with enhanced oncolytic capability and through a right combination of the virus mediated innate and adaptive immune responses, particularly represented by the sizes of the two immune killing rates. A delay in the start of the adaptive immune response may not have a notable effect on the short-term dynamics of tumor growth, but may negatively impact the efficacy of the virotherapy in the longer-term, especially during the tumor re-growth phase.

The findings in this study can help us better understand the complications in tumor-viral dynamics, and can provide useful guidelines to design and improve the virotherapy. A limitation in our model is the relatively simple geometry; the assumption of spherical symmetry, though mathematically natural and computationally efficient, may not be able to reflect the realistic, often irregular, shapes of many tumors and the related intricacy in tumor growth. Our modeling framework can be extended to three-dimensional spatial domain for a more general investigation of tumor growth, though with a higher level of computational

challenge. We also hope to utilize clinical data to fit and validate our general mathematical formulation. Another limitation in our study is the assumption of homogeneity among all tumor cells. Practically, tumor cells may exhibit spatial heterogeneity that involves different levels of susceptibility and resistance to viral infection, varied strength of immune responses, and anisotropic movement of tumor cells and viruses. Incorporation of such heterogeneity into the modeling framework will potentially lead to deeper insight into tumor dynamics under the virotherapy.

In addition to this, we have analyzed several equilibrium points of a simplified ODE system to better understand the dynamics of tumor virotherapy. We have presented basic results with parameter variation in initial virus configuration and burst sizes that align very well with the PDE model and our expectation. We have shown a couple boundary and positive equilibrium points that are either globally or locally asymptotically stable, which means that the tumor cells can be controlled. Hence, if certain parameter conditions are satisfied, the virotherapy can be effective. We have also presented scenarios, based on burst size and initial cell densities, where the system undergo periodic oscillations. This stability analysis of a dynamic ODE system have enriched our understanding of tumor growth.

CHAPTER 4

FSI OF TUMOR CELLS

4.1 BACKGROUND

In 1995, Peter Friedl noticed a group of cancer cells moving as a single co-ordinated group. Although this theory was rejected multiple times early on, two decades later, the biological community has been increasingly convinced of the mobile cluster formation of the tumor cells [51]. Lately, the idea of cell "jamming" is gaining quite a bit of popularity as well among many physical scientists. The idea behind cell jamming is that the cells could be packed together so tightly that they form a single unit. Jeffrey Fredberg, Lisa Manning and other bio-physicists are extensively working on cancer models that incorporates the jamming idea that will help us better understand tumor FSI dynamics [51]. The researchers in this field believe that this principle of cell jamming provides justification for cancer cell movements and behavior. We are yet to see the medical and biological community fully backing up the jamming of cells theory. Nevertheless, it is clear that important biological processes including tissue repair and tumor metastasis and invasion require collective cell motions and to drive these motions cells exert forces on the surrounding (see [75] and [59]) for detail). Our preliminary research in this vast topic, however, will be more concerned with this clustering and movement of cells. Migration of clustered cells has been highlighted as being among the ten greatest unsolved mysteries in all of biology and significant amount of research needs to be done to properly understand the mechanism behind collective cellular migration [59].

The growth processes of cancer cells commonly include cell growth, division, and aggregation. However, due to complexity involved in the cell growth process along with other enlightening research that suggests the tendency of cells to move as a clustered unit , this chapter will only be focused on the aggregation dynamics of cells in the FSI study. Using the method described in Chapter 2 as our base model, the modified method here will allow us to study the clustering process of the cells that will act as one complex tissue during the

tumor progression. This is important in understanding the interaction between the cells and extra cellular matrix.

This chapter will highlight our preliminary work on cell aggregation which will serve as a starting point for further study of tumor growth. The parameters involved in fluid-structure interaction of tumor cells are very ill studied and not many clinical data are available in the literature. Therefore, our goal here is not to match the real time pattern of tumor cell aggregation and movement, but rather provide a solid foundation for studying the biophysical mechanism of tumor FSI. In this chapter, a cell is represented as a rigid freely moving disc. Due to the lack of actual cell properties in the disc (like elasticity for example), we will refer to the cell as simply disc in the rest of the chapter. However, it is important to note that our FSI framework is able to handle both rigid and deformable structure, so this work should seamlessly extend to our future work.

In the next few sections, we will describe the equations governing the structural motion, the numerical method and provide some results. We will simulate a fluid-structure model for a viscous incompressible fluid and a non-stationary solid disc. Please be advised that this is only a toy model and we will elaborate our work to elastic discs in the near future. We start this chapter with a single non-stationary rigid disc that is allowed to move freely under body forces and gravity. This is our first test of the fluid structure interaction of a rotating disc, which we will extend into multiple discs. We also provide an example of three disc aggregation that in effect handles discs touching, aggregation, and movement as a single unit. The framework, in general, is similar to the one explained in Chapter 2 that uses Direct Forcing Immersed Boundary Method with a partitioned approach, with some modifications in the Forcing term and the structure dynamics which will be described in the next section.

4.2 STRUCTURAL EQUATION OF MOTION

Here we derive the equation of motion for a free rigid body and is simplified for a circular disc in the next section. Figure 49 shows a rigid body occupying the domain, Ω. Two coordinate systems are used here to describe the motion of the rigid body. One is the global coordinate system, $X - Y - Z$, which is fixed on the ground. The other is the body-fixed coordinate system, $x' - y' - z'$, whose origin is placed at point O. The movement of an arbitrary point, P, in the rigid body can be measured by the relative motion between the body-fixed coordinate system and the global coordinate system. That is, the position vector

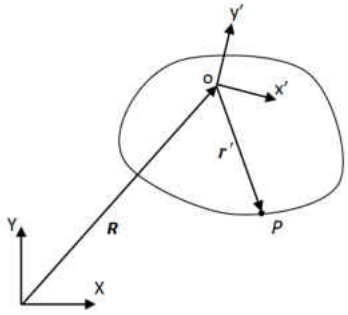

FIG. 49: A rigid body

of point P in the body, r, is defined in terms of the global coordinate system as

$$\mathbf{r} = \mathbf{R} + A\mathbf{r}' \tag{83}$$

where $\mathbf{R}$ is the position vector of the origin of the body-fixed coordinate system, $\mathbf{r}'$ is the position vector of the point in the body with respect to the body-fixed co-ordinate system, which is in terms of the local coordinate system, and A is the transformation matrix in terms of the angular displacements of the body. Thus, according to the presented model, the degrees of freedom of the rigid body are made of those describing the motion of the body-fixed coordinates; i.e., the translation, $\mathbf{R}$, and the orientation, θ , of the body-fixed coordinate system.

The matrix equation of the motion of a rigid body can be symbolically expressed by

$$M\ddot{\mathbf{q}} - \mathbf{f}^s(\mathbf{q}, \dot{\mathbf{q}}, t) = 0 \tag{84}$$

where the unknown vectors and their time derivatives are given as $\mathbf{q}^T = (\mathbf{R}^T \quad \theta^T)$, $\dot{\mathbf{q}}^T = (\dot{\mathbf{R}}^T \quad \mathbf{w}^T)$ and $\ddot{\mathbf{q}}^T = (\ddot{\mathbf{R}}^T \quad \boldsymbol{\alpha}^T)$ in which $\mathbf{w}$ is the angular velocity and $\boldsymbol{\alpha}$ is the angular acceleration. The mass matrix, M, and the force vector, $\mathbf{f}^s$, can be further spanned as follows, based upon their corresponding degrees of freedom.

$$M = \begin{bmatrix} M_{RR} & M_{R\theta} \\ M_{\theta R} & M_{\theta\theta} \end{bmatrix} \quad \mathbf{f}^s = \begin{bmatrix} \mathbf{f}_R \\ \mathbf{f}_\theta \end{bmatrix}.$$

In this section, $\mathbf{f}^s$ refers to the structural body forces that drive the motion of the structure.

For the case when the origin of the body-fixed coordinate system, Point O in Figure 49, lies at the centroid of the body, one has $M_{r\theta} = M_{\theta R} = 0$. Thus the mass matrix can be written as

$$M = \begin{bmatrix} M_{RR} & 0 \\ 0 & M_{\theta\theta} \end{bmatrix} = \begin{bmatrix} M & 0 \\ 0 & I_{\tilde{r}'\tilde{r}'} \end{bmatrix}$$

and the force vector as

$$\mathbf{f}^s = \begin{bmatrix} \mathbf{f}_R \\ \mathbf{f}_\theta \end{bmatrix} = \begin{bmatrix} \mathbf{F}_O + \nu \mathbf{f}_b \\ -\tilde{\mathbf{w}}' I_{\tilde{r}'\tilde{r}'} \mathbf{w}' + \mathbf{T}'_O \end{bmatrix}$$

Specifically, the equation of motion for a rigid body with its body-fixed coordinate system being placed at its centroid is given by

$$\begin{cases} M\ddot{\mathbf{R}} = \mathbf{F}_O + \nu \mathbf{f}_b \\ I_{\tilde{r}'\tilde{r}'} \boldsymbol{\alpha}' = -\tilde{\mathbf{w}}' I_{\tilde{r}'\tilde{r}'} \mathbf{w}' + \mathbf{T}'_O. \end{cases} \tag{85}$$

In general, $\tilde{\boldsymbol{\chi}}$ denotes a skew matrix made of vector $\boldsymbol{\chi}^T = (\chi_x \quad \chi_y \quad \chi_z)$ as

$$\tilde{\boldsymbol{\chi}} = \begin{bmatrix} 0 & -\chi_z & \chi_y \\ \chi_z & 0 & -\chi_x \\ -\chi_y & \chi_x & 0 \end{bmatrix}$$

Note that in equation (85), M is a 3x3 diagonal matrix with the value of the mass, ν is the volume of the body and $I_{\tilde{r}'\tilde{r}'}$ is the mass moment of inertia of the body which is defined as

$$\begin{aligned} I_{\tilde{r}'\tilde{r}'} &= \int_\Omega \rho \tilde{\mathbf{r}}' \tilde{\mathbf{r}}' \mathrm{d}v \\ &= \int_\Omega \rho \begin{bmatrix} z'^2 + y'^2 & -x'y' & -x'z' \\ -y'x' & z'^2 + x'^2 & -y'z' \\ -z'x' & -z'y' & y'^2 + x'^2 \end{bmatrix} \mathrm{d}v \end{aligned}$$

As for the terms on the right hand side of equation (85), they are associated with the external forces; $\mathbf{F}_O$ is the resultant forces applied at the origin of the body-fixed coordinate

system, Point O, in terms of the global coordinate system, $\nu\mathbf{f}_b$ is the body force due to the weight of the body and $\mathbf{T}'_\theta$ is the resultant torque produced by the external forces, applied at Point O in terms of the body-fixed coordinate system.

4.2.1 EQUATIONS OF MOTION FOR A CIRCULAR DISC

The problem of concern in this study is the motion of multiple cells in an internal flow. Each cell is modeled as a circular, rigid disc. The co-ordinate system of a circular disc is the same described above with the origin of the body-fixed co-ordinate system being placed at its center. The disc itself is subject to the gravity along the negative y direction and the circumference of the disc is subject to the distributed fluid pressure and the surface friction. The equation of motion for the structure described in this chapter, a freely moving circular rigid disc and its derivation, is the same as before. Since our problem is two dimensional in nature, with three degress of freedom, and the circular disc is symmetric with respect to the body-fixed coordinate system, equation(85) can be simplified as

$$\begin{bmatrix} m & 0 & 0 \\ 0 & m & 0 \\ 0 & 0 & I_{z'z'} \end{bmatrix} \begin{bmatrix} \ddot{\mathbf{R}}_x \\ \ddot{\mathbf{R}}_y \\ \ddot{\theta} \end{bmatrix} = \begin{bmatrix} \mathbf{F}_{ox} + \nu\mathbf{f}_{bx} \\ \mathbf{F}_{oy} + \nu\mathbf{f}_{by} \\ \mathbf{T}_{oz} \end{bmatrix} \equiv \begin{bmatrix} f_x \\ f_y \\ T_z \end{bmatrix} \tag{86}$$

The mass, the volume and the mass moment of inertia, can all be obtained as the sum of integrals, each of which is numerically evaluated in the associated quadrilateral element Ω_i. For instance, the mass moment of inertia is calculated as

$$I_{\tilde{z}'\tilde{z}'} = \sum \int_\Omega \rho(y'^2 + x'^2)\mathrm{d}v$$

The distributed loads due to surface pressure and friction can also be lumped into equivalent nodal forces based upon the definition of a quadrilateral finite element. With these computed boundary nodal forces, the induced, resultant forces (F_{ox} F_{oy}) and the torque T_{oz} can then be conveniently calculated.

4.3 NUMERICAL METHOD

The method used here, at least for now, is the same as described in Chapter 2, with a small change -particularly the addition of extra force to handle adhesion of cells. The

natural approach to do this is to introduce an "artificial" force acting at the centers of the discs as described in [74]. The force acts on two distinct boundary points ($\mathbf{X}_k(t)$, $\mathbf{X}_l(t)$) and satisfies Hooke's law with the constant spring stiffness K_{adh}. The formal model is given by

$$\mathbf{F}_{adh}(l,t) = \begin{cases} K_{adh}\dfrac{||\mathbf{X}_k(t) - \mathbf{X}_l(t)|| - 2r}{||\mathbf{X}_k(t) - \mathbf{X}_l(t)||}(\mathbf{X}_k(t) - \mathbf{X}_l(t)) & \text{if} \quad ||\mathbf{X}_k(t) - \mathbf{X}_l(t)|| <= 2r \\ \mathbf{0} & \text{otherwise.} \end{cases} \tag{87}$$

Here r is the radius of the disc, and the adhesion force $\mathbf{F}_{adh}$ is evaluated at each time step based on the position of the discs. Once the discs touch each other, this force kicks in and attempts to keep the discs as a union maintaining the distance between any two centers at $2r$. The final force $\mathbf{F}$ in the FSI process is calculated by summing up the force $\mathbf{F}$ as presented in chapter 2 and the adhesion force $\mathbf{F}_{adh}$. The rest of the process that involves interpolating the force $\mathbf{F}$ from Lagrangian grid to the Eulerian grid, and transfer of the force as a load to the structure follows as usual.

An overview of the method that is used in the subsequent sections can be summarized as follows, after we set up n number of discs with some initial velocity $\mathbf{V}_0$, all at least ϵ distance from each disc center, $\epsilon > 2r$,

- Calculate the total FSI forces, including the adhesion force, at the fluid-structure interface.
- Distribute the forces from the interface to the Eulerian grids.
- Solve the Navier Stokes equations.
- Interpolate the fluid velocity from the background Eulerian grids to the interfacial Lagrangian grids for all discs.
- Calculate the disc distances between all discs.
- Check to see if any discs touch each other, if so, an approximate mean of the velocity and force of the discs is used to estimate the velocity and force of the union of the discs.

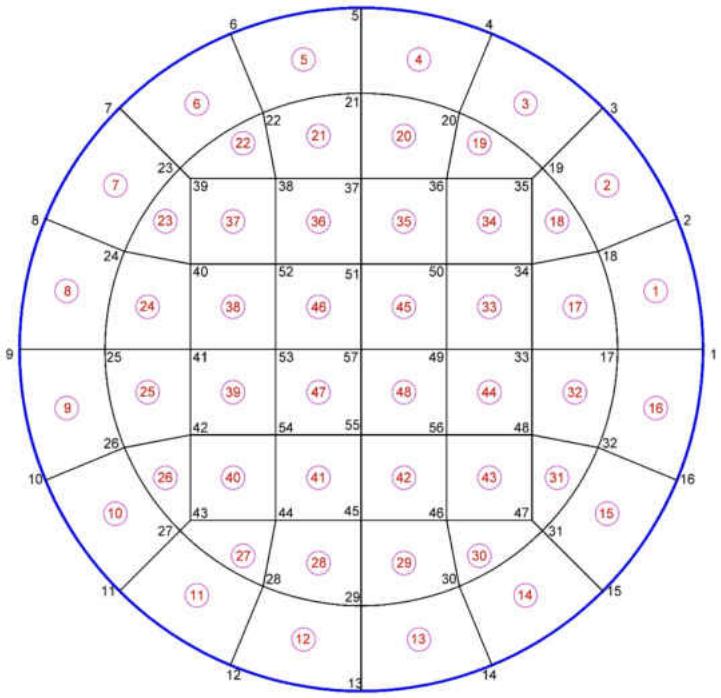

FIG. 50: Mesh of a disc

- With the boundary force, solve the governing equations for structures sequentially for all discs. Note that the boundary force is treated as a constant while solving equation (85) numerically from timestep t_n to t_{n+1}.
- Update the velocity and position of all structures and move on to the next time step.

When two discs collide, they attach on to one another with no future possibility of detaching, and act as a union of two discs for the remainder of the simulation. There is also a possibility of the discs forming multiple clusters, so it is essential for us to track the discs using "Groups" as well. Each disc starts out in a unique group, and if they all end up in the same group, we say that all the discs have clustered as one.

4.4 RESULTS

The computational domain is set to [0,50] x [0,50]. The material properties of the disc is given in Table 6. The other parameters used in the simulation are as follows: dynamic viscocity $\mu = 100$, fluid velocity in the horizontal direction $\mathbf{u}_0 = 10$, fluid density $\rho^f = 0.5$,

TABLE 6: Material properties of a disc

Young's modulus	Poisson's ratio	density
1000 psi	0.3	10 lb/in^3

and $\Delta t = 10^{-4}$, unless other wise noted. A disc of radius 2 is placed at the center of the fluid domain. Figure 50 shows the mesh of the disc that is discretized into 48 CQUAD elements with 57 grid points. The information between the fluid and the structure are exchanged at the 16 boundary nodes (Node 1 through 16 in the Figure 50). The position of the center (x, y, θ), velocity of the disc, and the boundary load is fed in to the structure solver. In return, the fluid solver gets the velocity and the displacement of the disc.

We will present two cases of interaction of fluid with the structure, single disc and multiple discs cases.

4.4.1 A SINGLE DISC

Here we present results for a single rigid disc, both stationary and non-stationary. To begin, we first run a simpler case of a stationary disc and the results are as expected. This is a special case of the rigid body motion where the disc's motion is 0. Figure 51 shows the streamline plots for Reynolds number 5 and 40 respectively.

Now, we turn our attention to a more realistic non-stationary disc governed by the translational and rotational laws of motion. A single disc of radius 2 is placed at the center of the domain, i.e. $(25, 25)$. All the parameters are the same as described in the previous section. The first result shows the affect of gravity on the position of the disc. Figure 52 shows the displacement of the center of the disc in the horizontal and vertical direction as t goes from 0 to 1. When there is no gravity, the disc moves in the x-direction only. As the gravity increases, the displacement in the negative y direction increases. In figure 53, the average torque force of the disc for the first 10,000 steps is shown. There is no rotation when the gravity is 0. The plot shows that the torque is positive for gravity greater than 0, i.e. the disc rotates in counter clockwise direction. The falling disc, due to gravity, will move from it's initial center position to the lower edge of the channel. That is, the flow underneath the disc will move faster than that above. Therefore the pressure is higher in the lower edge

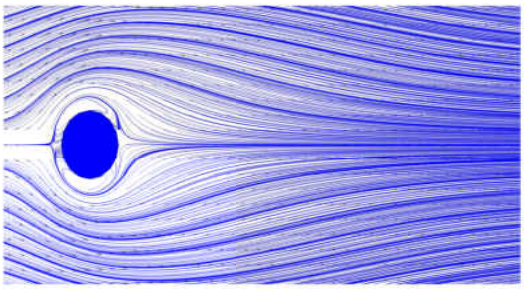

(a) Re=5

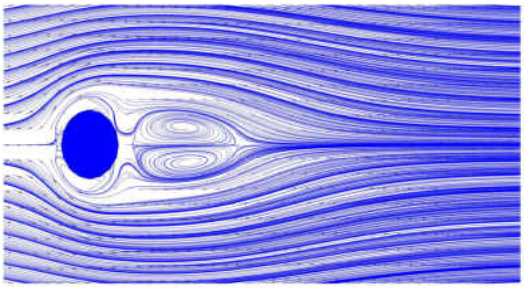

(b) Re=40

FIG. 51: Streamline visualization for a flow past a stationary disc.

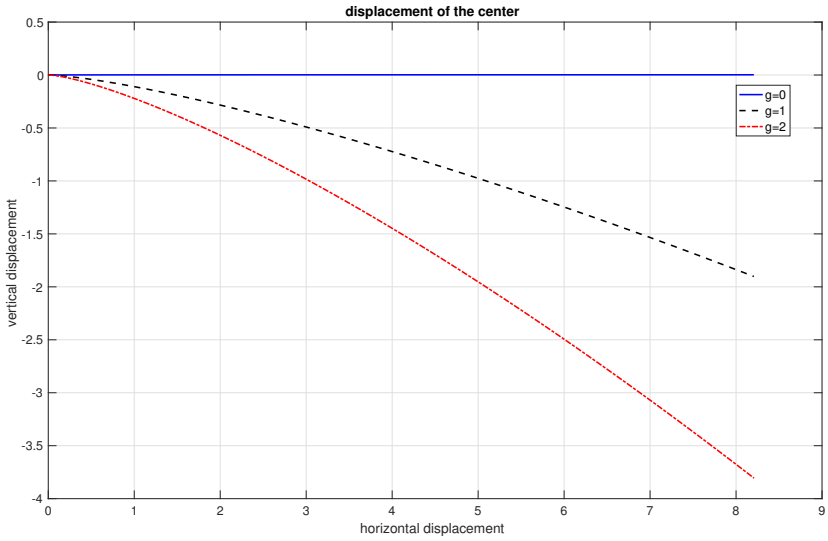

FIG. 52: Displacement of the center for different gravity

of the disc than above. As a result, the falling of the disc will slow down and the disc will rotate in counter clockwise direction. As seen in the plot, the rotation of the disc gradually increases as gravity increases because the distance between the disc and bottom edge of the channel will decrease faster for a higher value of gravity. Figure 54 shows the snapshot of the disc at several time steps for gravity = 1. The movement of the disc is as expected based on the parameters prescribed. Figure 55 shows the movement of a single disc along with the fluid flow at various time steps. The parameters are the same as before except for initial fluid velocity and dynamic viscosity which are set to 1 and 0.1 respectively.

4.4.2 MULTIPLE DISCS TEST

In this section, we start with the simulation of three discs to mimic the aggregation and movement process of the cells. The goal is to properly track the clustering of the discs over time. We place the discs around the middle of the computational domain centered at (20,25), (24.4,25), and (23,29) and refer it to Disc 1, Disc 2, and Disc 3 respectively. We start the aggregation process based on the numerical method described in the previous section. Once the discs are clustered, they move similarly to a single disc but as a union. All the parameters used are the same as before along with the following initial disc velocities of $(\mathbf{1},\mathbf{2})$, $(-\mathbf{2},-\mathbf{2})$

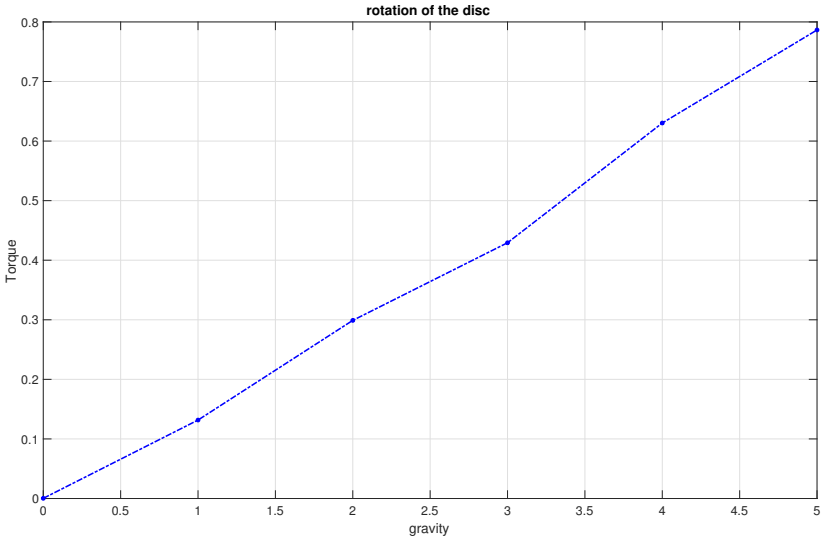

FIG. 53: Rotation of the disc under different gravity

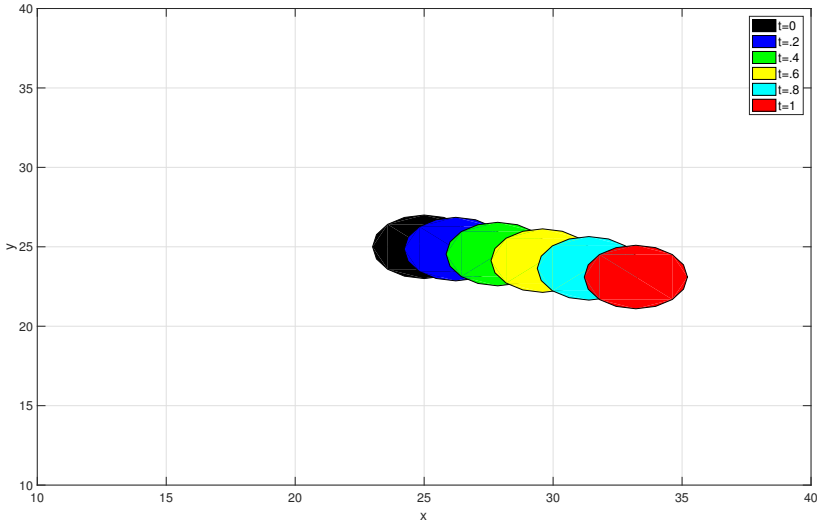

FIG. 54: Snapshot of the disc at various time steps

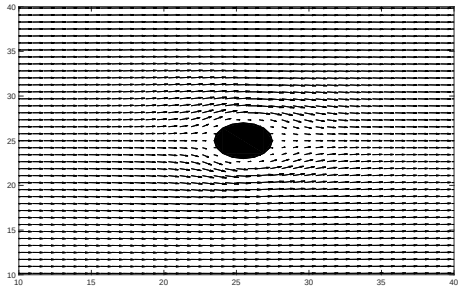

(a) $t = 2$

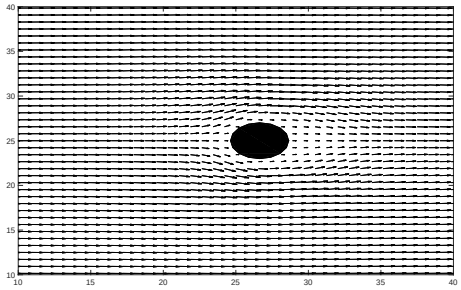

(b) $t = 6$

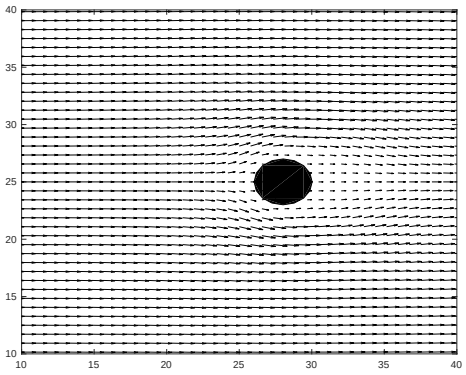

(c) $t = 10$

FIG. 55: Non-stationary disc along with the fluid flow at different time steps.

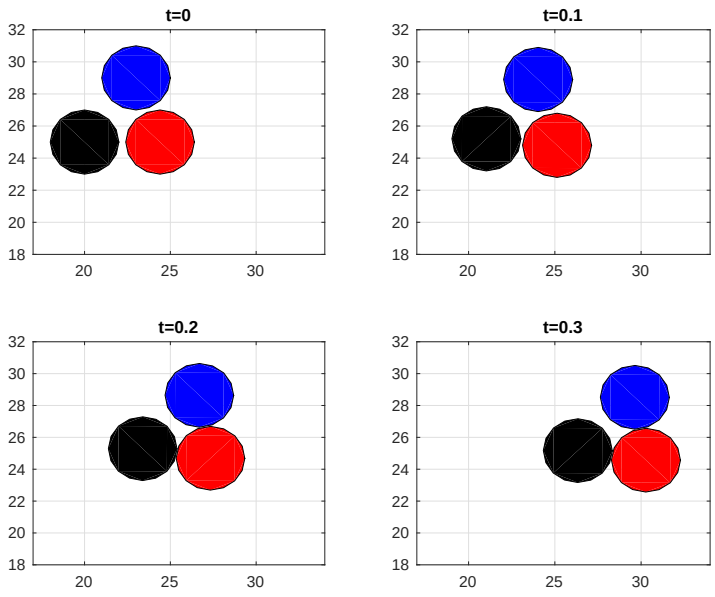

FIG. 56: Disc positions at various time steps

and (**1**,−**1**). Figure 56 shows the position of the disc at various time steps. Initially none of the discs are in contact with each other. A little before $t = 0.2$, disc 1 and disc 2 come in contact with one another. Very soon after that first contact, disc 2 and disc 3 also touch each other. Over the course of the simulation, the clustered unit of 3 discs continue to move along the flow as a single unit.

Figure 57 shows the horizontal and vertical velocities of all three discs from $t = 0$ to $t = 1$. This confirms our previous claim of how the aggregation takes place; i.e. disc 1 coming in contact with disc 2 and then their union clustering with disc 3 with point of contact at disc 2.

Finally, using the same rationale and methodology as 3 discs, we present two cases with 100 discs placed randomly in a domain of [0,800] x [0,800] and random initial velocities. The difference here is the possibility of the discs to form multiple clusters during the simulation process. Figures 58 and 59 display the aggregation and movement of such discs over time. As seen in the plots, the discs form several clusters which is dictated by the position and velocity of each discs. Each cluster so formed move as a single unit along the flow. They are free to attach to another group of discs and form a bigger cluster, but may never detach

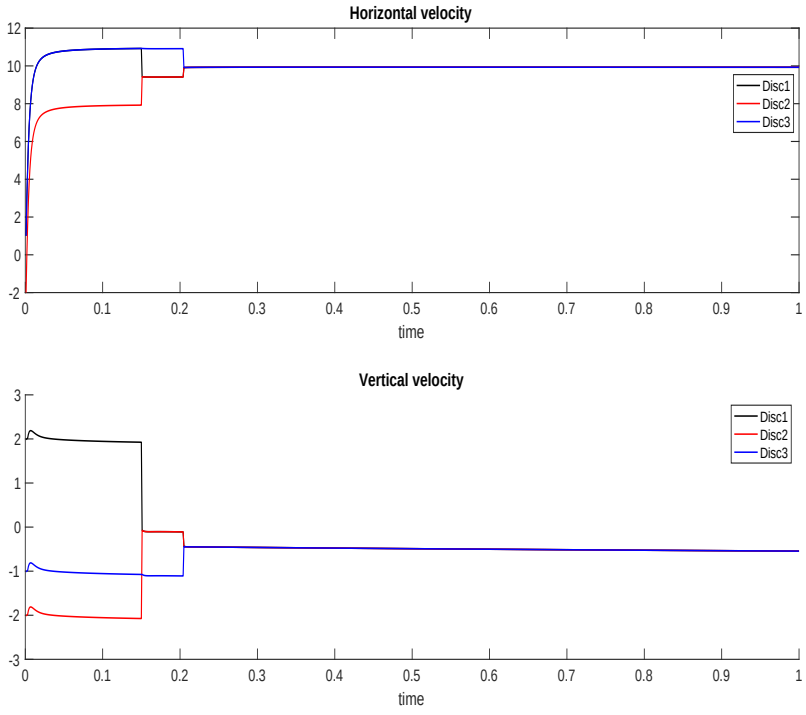

FIG. 57: Horizontal and Vertical velocity of the center of the three discs

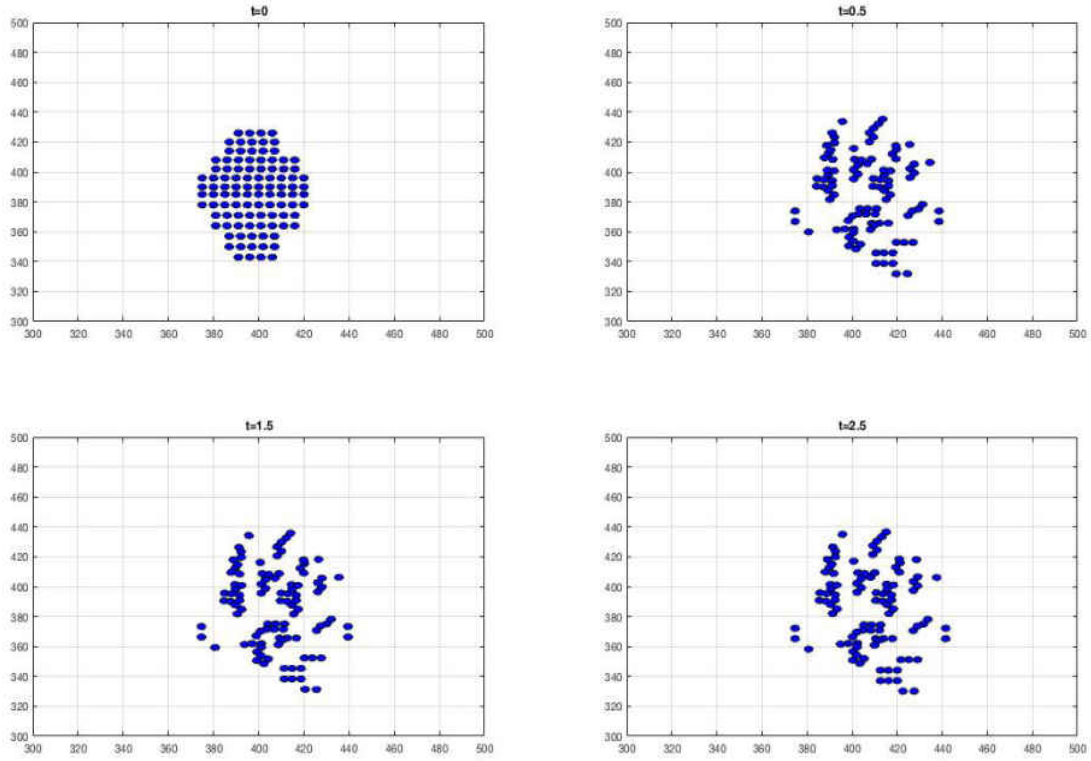

FIG. 58: Case1: Disc positions of 100 discs at different time steps

from their original cluster.

4.5 DISCUSSION

Clustering of cells and its movement as one unit are an important, yet relatively less studied, phases in cancer progression. Moreover, the cell-cell dynamics along with other extra cellular matrix is vital in understanding the growth of tumor and successfully treating it. In this chapter, we attempted to study the aggregation and movement of the cells using the modified Immersed Boundary and Direct Forcing approach. For simplicity, we modeled cells as freely moving rigid body discs and studied their fluid-structure interaction process, with as many as three discs. The fluid motion equations are similar to the ones described in Chapter 2, whereas the structure motion is now governed by the laws of rigid body motion.

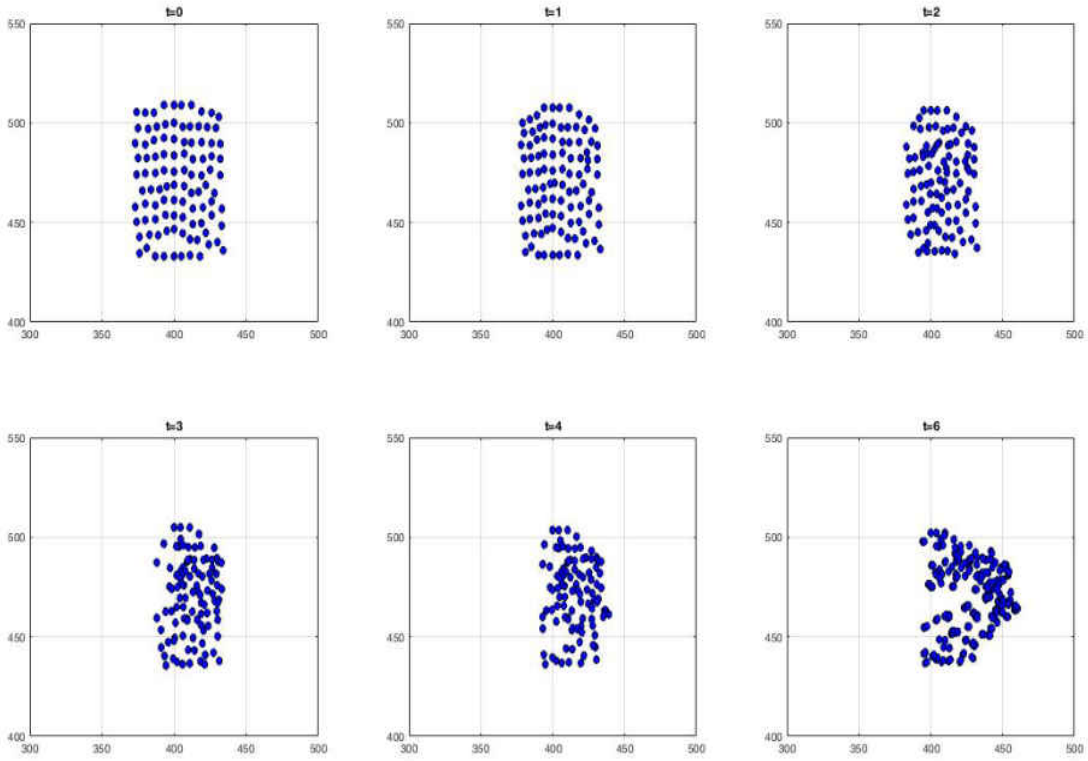

FIG. 59: Case2: Disc positions of 100 discs at different time steps

We have added an extra force in the Forcing term to account for adhesion of the discs when they come in contact with each other. This way we are able to keep all the discs within the prescribed distance of each other. The results are tested for two cases: a single disc and multi-disc flow. We perform careful numerical simulations with one, three and hundred discs to study disc movement as they attach to one another in the internal fluid flow. Both cases show promising results based on their movement, adhesion, torque, different gravity, etc. Although we have made major simplifications to the actual biomechanism of tumor FSI dynamics in this study, we have shown that the movement of the cells and clustering process of cancer cells can be effectively tracked and studied using our method.

This is only our preliminary work in our quest for achieving a better understanding of tumor FSI dynamics. We acknowledge that the current model for tumor FSI is far from realistic, and our goal is to continue improving the model. On that note, a few things that will be included in our future work are: represent cell as a non-linear elastic disc, adapt a better collision and adhesion strategy, optimize numerical methods so that it can handle thousands of cells, etc. Future models might also feature a 3D design of the cell, along with incorporation of other biochemical processes that will more accurately resemble the actual biological process involved in fluid structure interaction of tumor cells.

CHAPTER 5

CONCLUSIONS

In this dissertation, we performed mathematical modeling and numerical simulation of physical and biological processes: fluid structure interaction(FSI) and virotherapy of tumor. We provide detailed computational framework for these two applied cases with extensive simulation and favorable results. These are great advances in each of its respective domain and can be applied to solve sophisticated problems using the techniques described.

FSI is a multiphysics problem that involves two fields, usually the fluid and structure, interacting with each other. There are no analytical solution for most of these highly complex flows, so we sought a computational approach to accurately predict the motion of the flow and the structure. There are many engineering fields that have direct application of FSI problems involving rigid or elastic structures. Some of the examples include hydrodynamics, biomechanics, aeroelasticity, etc and the possibilities are endless. In chapter 2, we proposed a new computational framework for studying fluid-structure interaction problems. We present a partitioned approach that are able to handle various structural types and complex movement. Our method generalizes the original Immersed Boundary Method and Direct Forcing to accommodate structures that occupy finite volumes and are represented by realistic material constitutive laws. The method proposed is computationally inexpensive and relatively simple to implement with the ability of solving complex problems in the naturally occurring interdisciplinary FSI field. With advanced mathematical models, rigorous numerical simulations and visuals confirming the results, our methodology accommodates any fluid-structure interaction process; and is able to handle complex geometries without regeneration of meshes for moving structures, in addition to the extra benefit of flexibility and portability of the partitioned approach.

Cancer is characterized by uncontrollable growth of cells and is a cause of millions of deaths every year. Tumor may be benign or malignant(cancerous). Tumor treatment using oncolytic virotherapy has gained a lot of attention lately, and rightly so. It is important to accurately understand the tumor-virus-immune dynamics to come up with an effective treatment plan in tumor virotherapy. Several different types of mathematical models have

been presented in the past decade to model virotherapy on tumor growth. However, none of the prior models include both the innate and adaptive immune responses. In chapter 3, we presented and validated a tumor virotherapy model, that accurately depicts the effect of virus and immune cells on tumor growth, based on partial differential equations that includes both the innate and adaptive immune responses. This strongly non-linear PDE system is impossible to analyze analytically. So, we analyze the growth of the tumor using computational means by carefully designing an efficient and accurate method that achieves second order accuracy in both time and space. We have shown that the efficacy of tumor virotherapy can be improved by promoting anti-tumor adaptive immunity and viral replicability, along with administrating viral doses on a regular interval. Furthermore, we have performed substantial stability analysis on the reduced ODE model (that involves both immune cells) to identify possible solutions for controlling tumor. We have shown boundary and endemic equilibrium points that are either locally and globally stable and have great biological significance in controlling tumor. All results are validated either analytically or numerically and shown using stability plots. In Chapter 4, we have extended our computational framework proposed in Chapter 2, for the simulation of multiple discs to emulate the movement and aggregation of tumor cells during the cancer progression process. This is a step towards building more realistic models to accurately describe the tumor FSI dynamics.

There is no question that the results of these models and analysis have enhanced our general understanding of roles of fluid and structure in a viscous fluid flow, and immune system in tumor virotherapy. Although all possibilities of future work has been described in each chapter, we list some of them here for completeness. Our future goal for FSI is to create better models that are more accurate and efficient for handling complex structures. Moreover, extension of the 2-D model to 3-D, although computationally more expensive, can be explored to represent more realistic objects. For the tumor virotherapy model, we would like to fit and validate our model with clinical data and introduce heterogeneity among tumor cells. Our immediate goal for tumor FSI dynamics is to model the aggregation of multiple fully deformable cells in a tumor using the framework provided in Chapter 4 with necessary adjustments. Our long term vision for expansion of the current work can be explained in two folds: i) treating the current FSI study (with a focus on cell aggregation) as the initial phase of the tumor dynamics, where a number of tumor cells aggregate with each other and form the initial mass of the tumor ii) link this with a tumor model like that in the third chapter, as the second phase, to study the growth of cell numbers and the (macroscopic) tumor size.

REFERENCES

[1] K.J. Bathe. Finite Element Procedures. Prentice-Hall, Englewood CliVs, New Jersey, 1996, 780-782.

[2] D. Calhoun. A cartesian grid method for solving the two-dimensional streamfunction- vorticity equations in irregular regions. Journal of Computational Physics, 176(2): 231 – 275, 2002.

[3] S.C.R. Dennis and G.Z. Chang. Numerical solutions for steady flow past a circular cylinder at reynolds numbers up to 100. Journal of Fluid Mechanics, 42(03):471-489, 1970.

[4] E.H. Dowell and K.C. Hall. Modeling of fluid-structure interaction. Annual Review of Fluid Mechanics, 33:445-490, 2001.

[5] E.A. Fadlun, R. Verzicco, P. Orlandi, and J. Mohd-Yusof. Combined immersed-boundary finite-difference methods for three-dimensional complex flow simulations. Journal of Computational Physics, 161(1):35-60, 2000.

[6] C. Farhat, M. Lesoinne, and P. LeTallec. Load and motion transfer algorithms for fluid/structure interaction problems with non-matching discrete interfaces. Computer Methods in Applied Mechanics and Engineering, 157:95-114, 1998.

[7] B. Fornberg. A numerical study of steady viscous flow past a circular cylinder. Journal of Fluid Mechanics, 98(04):819-855, 1980.

[8] D. Goldstein, R. Handler, and L. Sirovich. Modeling a no-slip flow boundary with an external force field. Journal of Computational Physics, 105:354-366, 1993.

[9] R.D. Guy and D.A. Hartenstine. On the accuracy of direct forcing immersed boundary methods with projection methods. Journal of Computational Physics, 229:2479-2496, 2010.

[10] G. Hou, J. Wang, and A. Layton. Numerical methods for fluid-structure interaction - A review. Communication in Computational Physics, 12(2):337-377, 2012.

[11] W.X. Huang, S.J. Shin, and H.J. Sung. Simulation of flexible filaments in a uniform flow by the immersed boundary method. Journal of computational physics, 226(2):2206- 2228, 2007.

[12] W.X. Huang and H.J. Sung. An immersed boundary method for fluidflexible structure interaction. Computer methods in applied mechanics and engineering, 198(33):2650- 2661, 2009.

[13] B. Hubner, E. Walhorn, and D. Dinkler. A monolithic approach to fluid-structure interaction using space-time finite elements. Computer Methods in Applied Mechanics and Engineering, 193:2087-2104, 2004.

[14] M. Jira sek. Basic concepts and equations of solid mechanics. Revue europ eenne de g enie civil, 11(7-8):879-892, 2007.

[15] Z. Li. An overview of the immersed interface method and its applications. Taiwanese Journal of Mathematics, 7:1-49, 2003.

[16] H. Luo, H. Dai, P. Ferreira de Sousa, and B. Yin. On the numerical oscillation of the direct-forcing immersed-boundary method for moving boundaries. Computers and Fluids, 56:61-76, 2012.

[17] R. Mittal and G. Iaccarino. Immersed boundary methods. Annu. Rev. Fluid Mech., 37:239-261, 2005.

[18] J. Mohd-Yusof. Combined immersed-boundary/b-spline methods for simulations of flow in complex geometries. Annual Research Briefs. NASA Ames Research Center. Stanford University Center of Turbulence Research: Stanford, pages 317-327, 1997.

[19] D.Z. Noor, M.J. Chern, and T.L. Horng. An immersed boundary method to solve fluidsolid interaction problems. Computational Mechanics, 44(4):447-453, 2009.

[20] CS. Peskin. The immersed boundary method. Acta numerica, 11, 2002.

[21] CS. Peskin. The immersed boundary method in a simple special case, September 2007. Lecture notes. Retrieved on April,14,2013.

[22] R.H. Pletcher, J.C. Tannehill, and D.A. Anderson. Computational Fluid Mechanics and Heat Transfer, Third Edition. CRC Press, 2011.

[23] P.B. Ryzhakov, R. Rossi, S.R. Idelsohn, and E. Onate. A monolithic Lagrangian approach for fluid-structure interaction problems. Computational Mechanics, 46:883-899, 2010.

[24] F. Sotiropoulos and X. Yang. Immersed boundary methods for simulating fluid structure interaction. Progress in Aerospace Sciences, 2013.

[25] M. Souli and D.J. Benson (Ed.). Arbitrary Lagrangian Eulerian and Fluid-Structure Interaction: Numerical Simulation. Wiley-ISTE, 2010.

[26] J. Steindorf and H.G. Matthies. Numerical efficiency of different partitioned methods for fluid-structure interaction. ZAMM - Journal of Applied Mathematics and Mechanics, 80(S2):557-558, 2000.

[27] S.W. Su, M.C. Lai, and C.A. Lin. An immersed boundary technique for simulating complex flows with rigid boundary. Computers and fluids, 36(2):313-324, 2007.

[28] K. Taira and T. Colonius. The immersed boundary method: a projection approach. Journal of Computational Physics, 225(2):2118-2137, 2007.

[29] M. Uhlmann. An immersed boundary method with direct forcing for the simulation of particulate flows. Journal of Computational Physics, 209(2):448-476, 2005.

[30] J. Vierendeelsa, K. Dumontb, and P.R. Verdonckb. A partitioned strongly coupled fluid- structure interaction method to model heart valve dynamics. Journal of Computational and Applied Mathematics, 215:602-609, 2008.

[31] J. Wang and A. Layton. Numerical simulations of fiber sedimentation in Navier-Stokes flows. Communications in Computational Physics, 5(1):61-83, 2009.

[32] L.T. Zhang and M. Gay. Immersed finite element method for fluid-structure interactions. Journal of Fluids and Structures, 23:839-857, 2007.

[33] N. Zhang and Z.C. Zheng. An improved direct-forcing immersed-boundary method for finite difference applications. Journal of Computational Physics, 221(1):250-268, 2007.

[34] X. Zhang, X. Zhu, and G. He. An improved direct-forcing immersed boundary method for fluid-structure interaction simulations. In ASME 2013 Fluids Engineering Division Summer Meeting, pages V01AT08A005-V01AT08A005. American Society of Mechanical Engineers, 2013.

[35] Andtbacka, RH, Kaufman, HL, Collichio, F, et al. Talimogene laherparepvec improves durable response rate in patients with advanced melanoma. J. Clinical Oncology [epub ahead of print on May 26, 2015].

[36] Araujo, RP and McElwain, LS, A history of the study of solid tumor growth: The contribution of mathematical modeling. Bulletin of Mathematical Biology, 2004, 66: 1039–1091.

[37] Bandringa H. Immersed boundary methods. Masters thesis, University of Groningen. 2010 Aug;9700.

[38] Chiocca, EA and Rabkin, SD, Oncolytic viruses and their application to cancer immunotherapy. Cancer Immunology Research, 2014, 2: 295–300.

[39] Friedman, A, Mathematical analysis and challenges arising from models of tumor growth. Mathematical Models and Methods in Applied Sciences, 2007, 17: 1751–1772.

[40] Friedman, A and Kao, C-Y, Mathematical Modeling of Biological Processes. Springer, 2014.

[41] Friedman, A, Tian, JP, Fulci, G, Chiocca, EA, and Wang, J, Glioma virotherapy: Effects of innate immune suppression and increased viral replication capacity. Cancer research, 2005, 66: 2314–2319.

[42] Fulci, G, Breymann, L, Gianni, D, et al, Cyclophosphamide enhances glioma virotherapy by inhibiting innate immune responses. Proc. Natl. Acad. Sci. USA, 2006, 103: 12873–12878.

[43] Golub, GH and Van Loan, CF, Matrix Computations. Johns Hopkins University Press, 2012.

[44] Kambara, H, Okano, H, Chiocca, EA and Saeki, Y, An oncolytic HSV-1 mutant expressing ICP34.5 under control of a nestin promoter increases survival of animals even when symptomatic from a brain tumor. Cancer Res. 2005, 65: 2832–2839.

[45] Karev, GP, Novozhilov, AS and Koonin, EV, Mathematical modeling of tumor therapy with oncolytic viruses: Effects of parametric heterogeneity on cell dynamics. Biology Direct, 2006, 1–30.

[46] Kasuya, H, Takeda, S, Nomoto, S, and Nakao, A, The potential of oncolytic virus therapy for pancreatic cancer. Cancer Gene Ther. 2005, 12: 725–736.

[47] Kirn, DH, McCormick, F, Replicating viruses as selective cancer therapeutics. Mol Med Today. 1996, 2: 519–527.

[48] Kirn, D, Hermiston, T, and McCormick, F, ONYX-015: Clinical data are encouraging. Nat Med. 1998, 4: 1341–1342.

[49] Lawler, SE and Chiocca, EA, Oncolytic virus-mediated immunotherapy: A combinatorial approach for cancer treatment. Journal of Clinical Oncology, 2015, 33: 2812–2814.

[50] Lowengrub, JS, Frieboes, HB, Jin, F, Chuang, Y-L, Li, X, Macklin,P, Wise, SM, and Cristini, V, Nonlinear modeling of cancer: Bridging the gap bewteen cells and tumors. Nonlinearity, 2010, 23: R1–R91.

[51] Popkin, Gabriel. Quanta Magazine. Biophysics. Jammed Cells Expose the Physics of Cancer. August 16,2016.

[52] Marchini, A, Scott, EM, and Rommelaere, J, Overcoming barriers in oncolytic virotherapy with HDAC inhibitors and immune checkpoint blockade. Chiocca, EA and Lamfers, MLM, eds. Viruses, 2016, 8– 9.

[53] Melcher, A, Parato, K, Rooney, CM, and Bell, JC, Thunder and lightning: Immunotherapy and oncolytic viruses collide. Molecular Therapy, 2011, 19: 1008–1016.

[54] Novozhilov, AS, Berezovskaya, FS, Koonin, EV, and Karev, GP, Mathematical modeling of tumor therapy with oncolytic viruses: Regimes with complete tumor elimination within the framework of deterministic models. Biology Direct, 2006, 1– 6.

[55] Parato, KA, Senger, D, Forsyth, PA, and Bell, JC, Recent progress in the battle between oncolytic viruses and tumours. Nat Rev Cancer. 2005, 5: 965–976.

[56] Parish, CR and O'Neill, ER, Dependence of the adaptive immune response on innate immunity: Some questions answered but new paradoxes emerge, Immunology and Cell Biology, 1997, 75: 523-527.

[57] Press, WH, Flannery, BP, Teukolsky, SA, and Vetterling, WT, Numerical Recipes in Fortran 90. Cambridge University Press, 1996.

[58] Shah, AC, Benos, D, Gillespie, GY, and Markert, JM. Oncolytic viruses: Clinical applications as vectors for the treatment of malignant gliomas. J Neurooncol. 2003, 65: 203–226.

[59] Sadati M, Qazvini NT, Krishnan R, Park CY, Fredberg JJ. Collective migration and cell jamming. Differentiation. 2013 Oct 31;86(3):121-5.

[60] Tian, JP, The replicability of oncolytic virus: Defining conditions on tumor virotherapy. Mathematical Biosciences an Engineering, 2011, 8: 841–860.

[61] Wang, J and Tian, JP, Numerical study for a model of tumor virotherapy. Applied Mathematics and Computation, 2008, 196: 448–457.

[62] Wodarz, D, Viruses as antitumor weapons: defining conditions for tumor remission. Cancer Res. 2001, 61: 3501–3507.

[63] Wodarz, D and Komarova, N. Computational Biology of Cancer: Lecture Notes and Mathematical Modeling. World Scientific Publishing Company, Singapore, 2005.

[64] Woller, N, Gürlevik, E, Ureche, C-I, Schumacher, A, and Kühnel, F, Oncolytic viruses as anticancer vaccines. Frontiers in Oncology, 2014, 4: 188.

[65] Wu, JT, Byrne, HM, Kirn, DH, and Wein, LM. Modeling and analysis of a virus that replicates selectively in tumor cells. Bull Math Biol. 2001, 63: 731–768.

[66] World Cancer Report 2014, Chapter 1.1. World Health Organization, 2014.

[67] World Cancer Report 2014, Chapter 6.7. World Health Organization, 2014.

[68] Ugwa KA, Agwu IA, Agbanyim Akuagwu N. Mathematical Analysis Of The Endemic Equilibrium Of Thetransmission Dynamics Of Tuberculosis. International Journal of Technology Enhancements and Emerging Engineering Research. 2013 Dec 25;2(12):263-9.

[69] Crivelli JJ, Fldes J, Kim PS, Wares JR. A mathematical model for cell cycle-specific cancer virotherapy. Journal of biological dynamics. 2012 Jan 1;6(sup1):104–120.

[70] Araujo RP, McElwain DS. A history of the study of solid tumour growth: the contribution of mathematical modelling. Bulletin of mathematical biology. 2004 Sep 1;66(5):1039–1091.

[71] Ashyani A, Mohammadinejad H, RabieiMotlagh O.Stability Analysis of Mathematical Model of Virus Therapy for Cancer. Iranian Journal of Mathematical Sciences and Informatics. 2016 Feb 7; Vol. 11, No. 2 (2016), pp 97–110.

[72] Li D, Ma W, Guo S. Stability of a mathematical model of tumor-induced angiogenesis. Nonlinear analysis-modeling and control. 2016 Jan 1;21(3):325–344.

[73] Tutkun B, Edis FO. An implementation of the direct-forcing immersed boundary method using GPU power. Engineering Applications of Computational Fluid Mechanics. 2017 Jan 1;11(1):15-29.

[74] Rejniak KA, Dillon RH. A single cell-based model of the ductal tumour microarchitecture. Computational and Mathematical Methods in Medicine. 2007 Mar 1;8(1):51-69.

[75] Trepat X, Wasserman MR, Angelini TE, Millet E, Weitz DA, Butler JP, Fredberg JJ. Physical forces during collective cell migration. Nature physics. 2009 Jun 1;5(6):426-30.

VITA

Asim Timalsina
Department of Computational and Applied Mathematics
Old Dominion University
Norfolk, VA 23529

PREVIOUS DEGREES

B.S. Applied Mathematics, May 2011, George Mason University.
M.S. Computational and Applied Mathematics, August 2013, Old Dominion University.

PUBLICATIONS

Asim Timalsina, Gene Hou, and Jin Wang. "Computing Fluid-Structure Interaction by the Partitioned Approach with Direct Forcing." *Communications in Computational Physics.* 21.1 (2017): 182-210.

Asim Timalsina, Jianjun Paul Tian, and Jin Wang. "Mathematical and Computational Modeling for Tumor Virotherapy with Mediated Immunity." *Bulletin of Mathematical Biology.* Accepted May, 2017.

SCHOLARSHIP

Modeling and Simulation Scholarship -MSVE, Old Dominion University 2014-2016.
Philip Wolf Award, Mathematics and Statistics Department, Old Dominion University, 2014.

Typeset using LaTeX.